Local structure of network formers and network modifiers in silicate melts at high pressure and temperature conditions

---

Marija Krstulović

Kumulative Dissertation

zur Erlangung des akademischen Grades
"doctor rerum naturalium"
(Dr. rer. nat.)
in der Wissenschaftsdisziplin „Mineralogie“

eingereicht an der
Mathematisch-Naturwissenschaftlichen Fakultät
Institut für Geowissenschaften
der Universität Potsdam

Ort und Tag der Disputation: Potsdam, 20.08.2021

Betreuer:
Prof. Dr. Max Wilke, Universität Potsdam
Dr. Sakura Pascarelli, European XFEL

Gutachter:
Prof. Dr. Jörg Erzinger, Universität Potsdam
Dr. Sakura Pascarelli, European XFEL
Dr Guillaume Morard, Université Grenoble Alpes

Published online on the
Publication Server of the University of Potsdam:
https://doi.org/10.25932/publishup-51641
https://nbn-resolving.org/urn:nbn:de:kobv:517-opus4-516415

Zusammenfassung

Silikatische Schmelzen sind wichtiger Bestandteil des Erdinneren und als solche leisten sie in magmatischen Prozessen einen wesentlichen Beitrag in der Dynamik der festen Erde und der chemischen Entwicklung des gesamten Erdköpers. Makroskopische physikalische und chemische Eigenschaften wie Dichte, Kompressibilität, Viskosität, Polymerisationsgrad etc. sind durch die atomare Struktur der Schmelzen bestimmt. In Abhängigkeit vom Druck, aber auch von der Temperatur und der chemischen Zusammensetzung zeigen silikatische Schmelzen unterschiedliche strukturelle Eigenschaften. Diese Eigenschaften sind am besten durch die lokale Koordinationsumgebung, d.h. Symmetrie und Anzahl der Nachbarn (Koordinationszahl) eines Atoms, sowie dem Abstand zwischen Zentralatom und Nachbarn (atomarer Abstand) beschrieben. Mit steigendem Druck und Temperatur, das heißt mit der zunehmenden Tiefe in der Erde, nimmt die Dichte der Schmelzen zu, welches zur Veränderung von Koordinationszahl und Abständen führen kann. Bei gleichbleibender Koordinationszahl nimmt der Abstand in der Regel zu. Kommt es zu Erhöhung der Koordinationszahl kann der Abstand zunehmen. Diese allgemeinen Trends können allerdings stark variieren, welches insbesondere auf die chemische Zusammensetzung zurückzuführen ist.

Dadurch, dass natürliche Schmelzen der tiefen Erde für direkte Untersuchungen nicht zugänglich sind, um ihre Eigenschaften unter den relevanten Bedingungen zu verstehen, wurden umfangreiche experimentelle und theoretische Untersuchungen bisher durchgeführt. Dies wurde häufig am Beispiel von amorphen Proben der Endglieder SiO_2, und GeO_2 studiert, wobei letzteres als strukturelles und chemisches Analogmodell zu SiO_2 dient. Meistens wurden die Experimente bei hohem Druck und bei Raumtemperatur durchgeführt. Natürliche Schmelzen sind chemisch deutlich komplexer als die einfachen Endglieder SiO_2 und GeO_2, so dass die Beobachtungen an diesen möglicherweise zu falschen Verdichtungsmodellen führen können. Weiterhin können die Untersuchungen an Gläsern bei Raumtemperatur potentiell starke Abweichungen zu Eigenschaften von Schmelzen bei natürlichen thermodynamischen Bedingungen aufweisen.

Das Ziel dieser Dissertation war es zu erläutern, welchen Einfluss die Zusammensetzung und die Temperatur auf die strukturelle Eigenschaften der Schmelzen unter hohen Drücken haben. Um das zu verstehen, haben wir komplexe alumino-germanatische und alumino-silikatische Gläser studiert. Genauer gesagt, wir haben synthetische Gläser studiert, die eine Zusammensetzung wie das Mineral Albit und wie eine Mischung von Albit-Diopsid im eutektischen Punkt haben. Das Albitglas ähnelt strukturell einer vereinfachten granitischen Schmelze, während das Albit-Diopsid-Glas eine vereinfachte basaltische Schmelze simuliert. Um die lokale Koordinationsumgebung der Elemente zu studieren, haben wir die Röntgenabsorptionsspektroskopie in Kombination mit einer Diamantstempelzelle benutzt. Dadurch, dass die Diamanten eine hohe Absorption für Röntgenstrahlung mit Energien unterhalb von 10 keV aufweisen, ist die unmittelbare Untersuchung der geologisch sehr relevanten Elemente wie Si, Al, Ca, Mg etc. mit dieser Spektroskopie in Kombination mit einer Diamantstempelzelle nicht möglich. Deswegen wurden die Gläser mit Ge und Sr dotiert. Diese Elemente dienen teilweise oder vollständig als Ersatzelemente für wichtige Hauptelemente. In diesem Sinne, dient Ge als Ersatzelement fur Si und andere Netzwerkbildner, während Sr Netzwerkwandler wie Z.B. Ca, Na, Mg etc., sowie andere Kationen mit grossem Ionenradius ersetzt.

Im ersten Schritt haben wir die Ge K-Kante im Ge-Albit-Glass, $NaAlGe_3O_8$, bei Raumtemperatur bis 131 GPa untersucht. Dieses Glas hat eine höhere chemische Komplexität als SiO_2 und GeO_2, aber es ist immer noch vollständig polymerisiert. Die Unterschiede im Verdichtungsmechanismus zwischen diesem Glas und den einfachen Oxiden können so eindeutig auf höhere chemische Komplexität zurückgeführt werden. Die partiell mit Ge und Sr dotierten

Albit und Albit-Diopsid-Zusammensetzungen wurden bei Raumtemperatur für Ge bis 164 GPa und für Sr bis 42 GPa untersucht. Während das Albitglass wie $NaAlGe_3O_8$ nominelll vollständig polymerisiert ist, ist das Albit-Diopsid Glas teilweise depolymerisiert. Die Ergebnisse zeigen, dass in allen drei Gläsern strukturelle Aïderungen in den ersten 25 bis maximal 30 GPa stattfinden, wobei beide Ge und Sr die maximale Koordinationszahl 6 bzw. $\sim$9 erreichen. Bei höheren Drücken findet in den Gläsern nur eine isostrukturelle Schrumpfung der Koordinationspolyeder statt. Der wichtigste Befund der Hochdruckstudien an den alumino-silikatischen und alumino-germanatischen Gläsern ist, dass in diesen komplexen Gläsern die Polyeder eine viel höhere Kompressibilität aufweisen als bei den Endgliedern zu beobachten. Das zeigt sich insbesondere durch die starke Verkürzung der Ge-O Abstände in dem amorphen $NaAlGe_3O_8$ und Albit-Diopsid-Glas bei Drücken über 30 GPa.

Zusätzlich zu den Effekten der Zusammensetzung auf den Verdichtungsprozess, haben wir den Einfluss der Temperatur auf die strukturelle Änderungen untersucht. Dazu haben wir das Albit-Diopsid-Glas untersucht, da es den Schmelzen im unteren Mantel chemisch am ähnlichsten ist. Wir haben die Ge K-Kante der Probe mit einer resistiv-geheizten und einer Laser-geheizter Diamantstempelzelle untersucht, für einen Druckbereich bis zu 48 GPa, sowie einen Temperaturbereich bis 5000 K. Hohe Temperaturen, bei denen die Probe flüssig ist und die für den Erdmantel relevant sind, haben einen bedeutenden Einfluss auf die strukturelle Transformation. Diese wird um ca. 30% zu deutlich niedrigeren Drücken verschoben, im Vergleich zu den Gläsern bei Raumtemperatur und unterhalb von 1000 K.

Die Ergebnisse dieser Dissertation stellen einen wichtigen Beitrag fur das Verständnis der Eigenschaften von Schmelzen unter Bedingungen des unteren Mantels dar. Im Kontext der Diskussion über die Existenz und den Ursprung von silikatischen Schmelzen mit ultrahoher Dichte, welche an der Grenze zwischen Mantel und Erdkern aufgrund seismologischer Daten vermutet werden, zeigen diese Untersuchugen, dass die im Vergleich zur Umgebung höhere Dichte nicht durch strukturelle Besonderheiten, sondern durch eine besondere chemische Zusammensetzung erklärt werden müssen. Außerdem legen die Ergebnisse nahe, dass für Schmelzen im unteren Erdmantel nur sehr geringe Löslichkeiten von Edelgasen zu erwarten sind, so dass die strukturellen Eigenschaften deutlich den Gesamthaushalt und Transport der Edelgase im Erdmantel beeinflussen.

Abstract

Silicate melts are major components of the Earth's interior and as such they make an essential contribution in igneous processes, in the dynamics of the solid Earth and the chemical development of the entire Earth. Macroscopic physical and chemical properties such as density, compressibility, viscosity, degree of polymerization etc. are determined by the atomic structure of the melt. Depending on the pressure, but also on the temperature and the chemical composition, silicate melts show different structural properties. These properties are best described by the local coordination environment, i.e. symmetry and number of neighbors (coordination number) of an atom, as well as the distance between the central atom and its neighbors (interatomic distance). With increasing pressure and temperature, i.e. with increasing depth in the Earth, the density of the melt increases, which can lead to changes in coordination number and distances. If the coordination number remains the same, the distance usually decreases. If the coordination number increases, the distance can increase. These general trends can, however, vary greatly, which can be attributed in particular to the chemical composition.

Due to the fact that natural melts of the deep earth are not accessible to direct investigations, in order to understand their properties under the relevant conditions, extensive experimental and theoretical investigations have been carried out so far. This has often been studied using the example of amorphous samples of the end-members SiO_2 and GeO_2, with the latter serving as a structural and chemical analog model to SiO_2. Commonly, the experiments were carried out at high pressure and at room temperature. Natural melts are chemically much more complex than the simple end-member SiO_2 and GeO_2, so that observations made on them may lead to incorrect compression models. Furthermore, the investigations on glasses at room temperature can show potentially strong deviations from the properties of melts under natural thermodynamic conditions.

The aim of this thesis was to explain the influence of the composition and the temperature on the structural properties of the melts at high pressures. To understand this, we studied complex alumino-germanate and alumino-silicate glasses. More precisely, we studied synthetic glasses that have a composition like the mineral albite and like a mixture of albite-diopside at the eutectic point. The albite glass is structurally similar to a simplified granitic melt, while the albite-diopside glass simulates a simplified basaltic melt. To study the local coordination environment of the elements, we used X-ray absorption spectroscopy in combination with a diamond anvil cell. Because the diamonds have a high absorbance for X-rays with energies below 10 keV, the direct investigation of the geologically relevant elements such as Si, Al, Ca, Mg etc. with this spectroscopic probe technique in combination with a diamond anvil cell is not possible. Therefore the glasses were doped with Ge and Sr. These elements serve partially or fully as substitutes for important major elements. In this sense, Ge serves as an a substitute for Si and other network formers, while Sr replaces network modifiers such as Ca, Na, Mg etc., as well as other cations with a large ionic radius.

In the first step we studied the Ge K-edge in Ge-Albit-glass, $NaAlGe_3O_8$, at room temperature up to 131 GPa. This glass has a higher chemical complexity than SiO_2 and GeO_2, but it is still fully polymerized. The differences in the compression mechanism between this glass and the simple oxides can clearly be attributed to higher chemical complexity. The albite and albite-diopside compositions partially doped with Ge and Sr were probed at room temperature for Ge up to 164 GPa and for Sr up to 42 GPa. While the albite glass is nominally fully polymerized like $NaAlGe_3O_8$, the albite-diopside glass is partially depolymerized. The results show that structural changes take place in all three glasses in the first 25 to a maximum of 30 GPa, with both Ge and Sr reaching the maximum coordination number 6 and $\sim$9, respectively.

At higher pressures, only isostructural shrinkage of the coordination polyhedra takes place in the glasses. The most important finding of the high pressure studies on the alumino-silicate and alumino-germanate glasses is that in these complex glasses the polyhedra show a much higher compressibility than what can be observed in the end-members. This is shown in particular by the strong shortening of the Ge-O distances in the amorphous $NaAlGe_3O_8$ and albite-diopside glass at pressures above 30 GPa.

In addition to the effects of the composition on the compaction process, we investigated the influence of temperature on the structural changes. To do this, we probed the albite-diopside glass, as it is chemically most similar to the melts in the lower mantle. We studied the Ge K edge of the sample with a resistively heated and a laser-heated diamond anvil cell, for a pressure range of up to 48 GPa and a temperature range of up to 5000 K. High temperatures at which the sample is liquid and that are relevant for the Earth mantle, have a significant impact on the structural transformation, with a shift of approx. 30% to significantly lower pressures, compared to the glasses at room temperature and below 1000 K.

The results of this thesis represent an important contribution to the understanding of the properties of melts at conditions of the lower mantle. In the context of the discussion about the existence and origin of ultra-dense silicate melts at the core-mantle boundary, these investigations show that the higher density compared to the surrounding material cannot be explained by only structural features, but by a distinct chemical composition. The results also suggest that only very low solubilities of noble gases are to be expected for melts in the lower mantle, so that the structural properties clearly influence the overall budget and transport of noble gases in the Earth's mantle.

Acknowledgments

First of all I want to thank my PhD supervisors: Prof. Dr. Max Wilke and Dr. Sakura Pascarelly, as well as my PhD mentor Angelika D. Rosa. I would also like to acknowledge the ESRF for the funding of the part of the PhD program and for the possibility for the thesis students to work at the ESRF and to have a direct access to the beamlines. At the ESRF I particularly want to thank BM23 and ID24 team, and especially Sakura Pascarelli and Olivier Mathon for giving me the opportunity to perform experiments at BM23 and ID24. I also want to thank Angelika Rosa for the beamline alighniment and support during my experiments, as well as Sebastian Pasternak and Florian Perrin and Jeron Jacobs for their technical support. I want to thank Institute of Geosciences of the University of Potsdam, and in particular to Max Wilke, who provided the funding for the part of this Dissertation. I also want to thank Max Wilke from the University of Potsdam and Sakura Pascarelli from the ESRF for providing me possibility to participate in conferences. From the University of Potsdam, I also want to thank Dr. Barbara Schneider and Prof. Dr. Andreas Taubert for their support in the final stage of my PhD thesis. I would also like to thank the members of the jury for reading this manuscript.

I want to thank to all people who supported me during my experiments: Nicole Biedermann, Angelika Rosa, Margarita Merkulova, Lélia Libon, Christian Albers and Max Wilke. I also thank Dario Ferreira Sanchez and Daniel Grolimund from the MicroXAS station of the SLS for giving me the opportunity to perform experiment in their beamline and for the beamline alignment. I am grateful to Dr. Tetsuo Irifune from GRC in Japan for providing the nanopolycrystalline diamond anvils for my experiments. I want to thank Rico Fuchs who was ready to synthesize the glasses for me at the Institute of Geosciences in Potsdam during my stay in Grenoble.

My personal thanks to Mariia for the friendship, support and interesting conversations during my stay at the ESRF in Grenoble. I am very grateful to Richard and Ruxandra for their unforgettable support and help to solve the issues that I was facing at the beginning of my PhD. I also want to thank Bojan for his friendship and support in the past before my studies, which influenced my future path, I am very grateful for everything he did for me. I am thankful to Diana for her friendship and Parisa for being a good neighbor in Potsdam. I also want to thank Maia Kober for supportive advises. I also want to thank my fellow student Freddie, who's company was always full of fun. I want to thank Keith for his support, and tolerance, patience and for a deep friendship. I also want to thank all other friends from my childhood in Bosnia: Bojana, Bojan, Marinko, Jovana and many others, and during my life and studies in Belgrade: Milica, Andjelka, Suncica, Nevena and others, whom I may have not mentioned here.

I want to thank my parents for giving me freedom to chose my way of life and for respecting my decisions in life and for their trust. Here, especially I want to thank my mother for being always ready to talk to me if I need it and for being my best friend. I want to thank my brother and his wife and their healthy and happy son Boris and daughter Leona whom I hope I will see soon, all of them.

List of Abbreviations

Ab albite

AbDi albite-diopside

ASI alumina saturation index

BO bridging oxygen

CMB core-mantle-boundary

CN coordination number

DAC diamond anvil cell

EMPA electron microprobe analysis

EOS equation of state

ESRF European Synchrotron Radiation Facility

EXAFS Extended X-Ray Absorption Fine Structure Spectroscopy

FXPM first XANES peak maximum

IXS Inelastic X-Ray Scattering

KB Kirkpatrick-Baez

LH-DAC Laser-heated diamond anvil cell

LLSVPs large low-shear-velocity provinces

MD molecular dynamics

MEE multi-electronic excitation

MORB mid-ocean ridge basalt

MRO medium-range order

NBO non-bridging oxygen

NF network former

NM network modifier

ppm parts per million

PRIUS Premier Research Institute for Ultrahigh-pressure Sciences

RH-DAC Resistively-heated diamond anvil cell

SRO Short-range order

ULVZs ultra-low-velocity zones

VtC-XES Valence-to-Core X-Ray Emission Spectroscopy

XAFS X-Ray Absorption Fine Structure Spectroscopy

XANES X-Ray Absorption Near Edge Spectroscopy

XAS X-Ray Absorption Spectroscopy

XES X-Ray Emission Spectroscopy

XRD X-Ray Diffraction

XRS X-Ray Raman Scattering

Contents

List of figures

Tables

Chapter 1

Introduction

Throughout the Earth's history, silicate melts have been playing a crucial role in shaping the structure of the planet. They are key agents in the physico-chemical differentiation and the evolution of the planet starting from the global magma ocean in the early stages of the Earth's history up to the current layered picture of the planet. Global macroscopic processes, those visible on the Earth's surface such as volcanic eruptions, and those hidden deep in the interior (mantle plumes or ultra-low velocity zones, ULVZs) bare witness to the presence of the melts throughout the Earth's mantle.

In order to melt the solid silicate mantle, the system must experience a temperature increase, a pressure drop, or the introduction of volatile components (e.g. OH or CO_2) (Fiquet, 2018, references therein). It has also been reported that mixtures of different components melt at lower temperature compared to pure end member compounds (Fiquet, 2018). Prominent examples for the shallow Earth region are the melting of the subducted oceanic lithosphere due to the presence of volatiles, and the melting beneath the mid ocean ridge due to decompression of the upwelling mantle. In this pressure-temperature arrangement, mineralogical assemblages such as clynopyroxene, orthopyroxene and spinel undergo melting, whereas olivine crystallizes during the melting process (Niu, 1997) . Even at higher depths, in the areas of the transition zone from the upper to the lower mantle, the existence of partial melts has been predicted and related to dehydration melting (Fei, 2021; Fiquet, 2018; Panero et al., 2020; Schmandt et al., 2014). In particular, the possible generation of such a layer at 410 km has been related to the dehydration of either the subducted oceanic crust or of OH-bearing minerals (Revenaugh and Sipkin, 1994; Vinnik and Farra, 2007, see Fiquet, 2018), or to the weaker water storage capacity of upper mantle minerals (Bercovici and Karato, 2003, see Fiquet, 2018). Recent studies proposed the existence of partial melts also at 660 km. Their existence is related to the transition from ringwoodite to bridgmanite by the convective forces which entrain ringwoodite minerals down to the lower mantle, where higher pressure and temperature trigger the melting (Fiquet, 2018). Improvements in seismic resolution contributed to the potential detection of melts also at the deepest areas of the mantle, the core-mantle boundary (CMB). Heterogeneously distributed patches, extending vertically between 5 to 50 km above the CMB and up to 100 km across are characterized by excessively reduced compressional and shear wave velocities of up to 10 to 30 % (Garnero et al., 1993; Garnero and Helmberger, 1998; Fiquet, 2018; Wen and Helmberger, 1998) and by density excess of about 10 % relative to the surrounding mantle (Andrault et al., 2014). Due to seismic wave velocity reduction these patches are called ultra-low velocity zones (ULVZs) and are schematically shown as red patches in FIG. 1.1. Some seismological investigations evidence three times stronger decrease of the S wave velocity compared to P wave velocity (Lay et al., 1998, Ravenaugh and Meyer, 1997; Williams and Garnero, 1996).

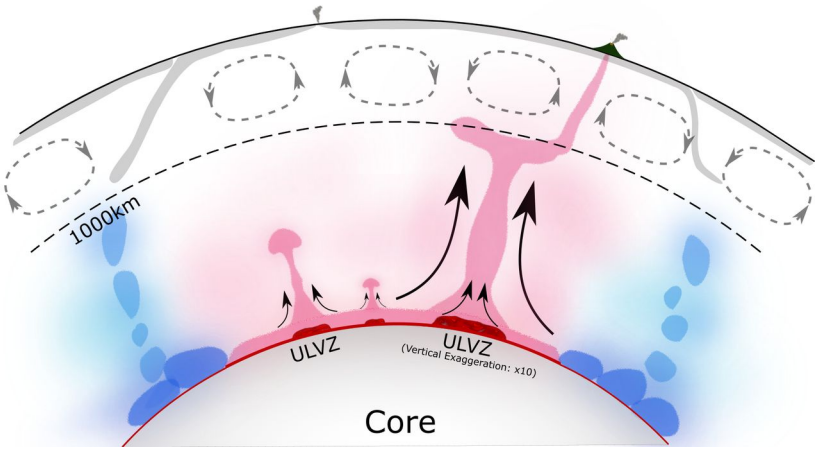

Figure 1.1: Conceptual sketch of the Earth's interior highlighting ultra-low velocity zones (ULVZs) as red patches at the root of the mantle plumes shown in pink (Yuan and Romanovicz, 2017). The ULVZs are vertically exaggerated by a factor of 10 relative to the thickness of the mantle and the height of the plumes. Subducted slabs above the 1000 km depth are shown in gray, whereas the slabs sinking down to the lower most mantle are shown in blue. Arrows indicate the flow direction (Yuan and Romanovicz, 2017).

Strong attenuation of the shear wave velocity coupled to a density increase provides a strong implication for the molten nature of these zones.

These partially molten zones located at the interface between two distinct media might play an important role for global processes. Their origin is however still a subject of discussion, but it is commonly related to thermal, compositional and/or phase heterogeneities (Garnero and McNamara, 2008). According to one hypothesis, the ULVZs are a result of the partial melt of the ambient lower mantle minerals that undergo further changes in the structure, which increases their density and makes them gravitationally stable at corresponding conditions. The weak side of this hypothesis is that the temperatures at the lower mantle conditions are not high enough to melt ambient mantle rock (Andrault et al., 2014). This deficit promotes the hypothesis proposing a compositionally distinct nature of these zones compared to the bulk mantle rock (Li et al., 2017). A prominent example of this conception is the melting of the subducted oceanic slab at the CMB (Andrault et al., 2014; Pradhan et al., 2015).

In order to answer questions about the nature and origin of the melts at deep Earth conditions, including those at the CMB, solid knowledge about the atomic-scale structural properties of melts are of fundamental importance. Structurally, silicate melts present disordered systems characterized only by a short- to medium-range order. Short-range order (SRO) describes the structural organization associated with the first coordination shell around a given central atom (Elliott, 2001). Quantities describing SRO are the average number of neighbors around the central atom or the coordination number, the average bond length between the central atom and the ligand, the nearest-neighbor bond-length distribution and the coordination-number distribution (Elliott, 2001). Medium-range order (MRO) is the next highest level of structural organization beyond SRO and is hence associated with the connectivity of adjacent SRO coordination polyhedra (Elliott, 2001). One important aspect of MRO is the type of linkage: face-, edge- or, most commonly, corner-sharing.

In a pure SiO_2 melt or glass, at ambient conditions, Si forms tetrahedral units with O atoms, where one Si is surrounded by four O atoms (SiO_4^{4-}) (Stebbins, 1995). In this arrangement O atoms are sitting at the edges of the tetrahedral units and each O atom is

being shared between two neighboring tetrahedra serving as a bridge between them. These O atoms are therefore called bridging oxygens (BOs), and their bridging role is facilitated by the connective nature of Si in the network. Si and other cations which facilitate the generation of BOs (e.g. Ge, Al) are commonly called network forming cations. The whole system of connected tetrahedral units builds an undistorted polymeric network. Si-O bonds in such tetrahedra are among the strongest in silicate materials (Stebbins, 2016).

Natural silicate melts are highly complex multi-component systems. After O, Si is the most abundant element in the Earth's crust and mantle. It has a very strong connection to O and is thus unlikely found in metallic form, but always either as a pure oxide (SiO_2) or as an integral component of the Earth's largest group of minerals – silicates. This strong connection of Si to O, which is much stronger than between other elements and O (Putnis, 1992) explains, why both crust and mantle are composed mostly of silicates. O and Si are followed by Al and by alkali and alkaline earth cations (e.g. Na, K, Ca, Mg), as well as by numerous trace elements, also in association with O. This chemical heterogeneity makes natural silicate melts structurally highly complex. While for example Al, similar to Si, preferentially creates polymeric chains, and thus acts as a network former (Trail et al., 2017), lower charged large cations, notably alkali (Na^+, K^+), and alkaline earth metals (Ca^{2+}, Mg^{2+}), but also other large cations (Y^{3+}, La^{3+}) are usually incorporated at interstitial positions of the random network breaking the polymeric chain. This generates oxygen atoms bonded to only one tetrahedron, so called non-bridging oxygens (NBOs) (Wolf and McMillan, 1995). These weakly bonded cations that are "decoupled" from the network and rapidly move about in the melt, are usually referred to as network modifying cations (Stebbins, 2016). In FIG. 1.2 a schematic image of the structure of silicate melts/glasses with network formers (NF), network modifiers (NM), BOs and NBOs is presented.

Depending on the ratio of BOs to NBOs or, depending on the number of NBOs per tetrahedron in the melt (NBO/T), which is also related to the amount and type of a specific cation, the melt will have different degree of polymerization. Degree of polymerization is one of the most important properties of the polymeric melts as it is directly related to its overall physical properties. Classically, using the NBO/T ratio, the degree of polymerization can be calculated from the chemical composition of the melt (Mysen et a., 1985). The weak side of this approach is the dual role of particular cations in the melt structure, such as Al^{3+} which may act not only as network former, but also as network modifier (Henderson, 2005), depending on the melt composition. Its network forming role is usually facilitated in association with low-field strength cations such as K^+ or Na^+ to satisfy charge balance with Al^{3+}, which allows for generation of tetrahedral units (Mysen and Richet, 2005; Mysen and Toplis, 2007; Trail et al., 2017). Alternatively, the network forming role is reached in association with alkaline earths, whereby for charge compensation two AlO_4 tetrahedra are required (Mysen et al., 1981; Trail et al., 2017). In its network forming role, together with charge compensating cations, Al facilitates the increase of the degree of polymerization. On the other side, if there are no low field strength cations to compensate the charge balance, the amount of Al in five- or even sixfold coordination increases (Mysen and Toplis, 2007; Trail et al., 2017), which contributes to the depolymerization of the melt.

A good estimate for the degree of polymerization in aluminosilicate melts can be determined from the alumina saturation index (ASI), which describes the saturation of Al in the melt from the molar ratio $Al_2O_3/(Na_2O+K_2O+CaO)$ (Zen, 1986, Zen, 1988). Depending on the ratio, three types of melt composition can be distinguished: peralkaline (ASI < 1), metaluminous (ASI $= 1$) and peraluminous (ASI > 1). While metaluminous melts are fully polymerized, highly peralkaline melts are strongly depolymerized, as, due to missing Al in the system, alkali and alkaline earth cations act as pure network modifiers. In peralkaline melts

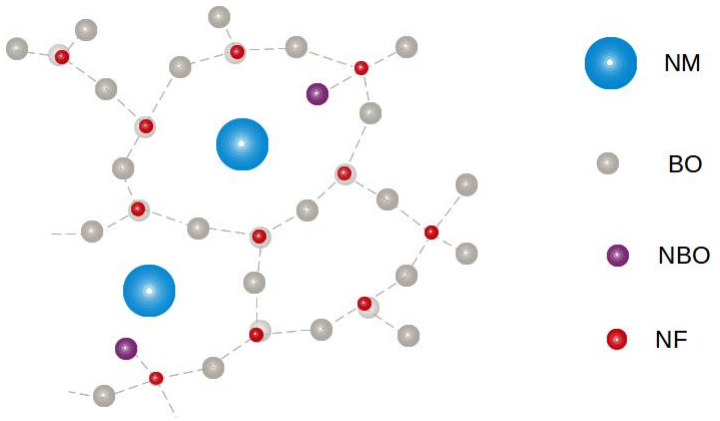

Figure 1.2: Schematic sketch (modified after Pohlenz et al., 2018) showing the structure of the silicate glass or melt network consisting of tetrahedrally coordinated network forming (NF) cations (e.g. Si, red) surrounded either by four bridging oxygen atoms (BO, gray), or by three BO and one non-bridging oxygen (NBO, violet) due to the presence of network modifying cation, NM (e.g. Ca, Mg, Na, K, blue).

with constant Si/Al ratio the degree of polymerization increases with increasing ASI towards 1 (Zen, 1988). Alkali-rich silicate melts have been found to have modified random networks (Greaves, 1985; Henderson, 1995; Huang and Cormack, 1990; Smith et al., 1995; Vessal et al., 1992; see also Pohlenz et al., 2018). In peraluminous melts when Al is not associated to the charge compensating cations, the excess Al enters (Al,Si)-triclusters in fourfold coordination with different Al/Si ratios depending on composition (Mysen and Toplis, 2007; Trail et al., 2017). In strongly peraluminous melt compositions, the Al fraction in five- or even sixfold coordination increases (Neuville et al., 2004; Trail et al., 2017).

Depending on its composition and thus on the degree of polymerization, at specific pressure and temperature conditions the melt will exhibit different structural properties with effects on its thermodynamic properties such as viscosity, diffusivity, growth of minerals, trace element partitioning, density or compressibility (Henderson et al., 1985; Kirkpatrick, 1975, Kirkpatrick, 1983; Prowatke and Klemme 2005; Scarfe et al., 1987). Starting from tetrahedrally coordinated Si (or also Al or Ge) at ambient pressure, under compression the number of neighboring O atoms continuously increases from 4 to 6, which results in a density increase of the melt. Thus the polyhedral geometries are continuously rearranging from tetrahedral to octahedral. The mechanism of the increase of the coordination number is accompanied by rotation of the polyhedra. These two coupled mechanisms result in the increase of the number of shared O atoms from one to two per two neighboring polyhedra. The polyhedra are not any more linked via corners, but via edges. Further, and in contrast to silicate melts at low pressure, the oxygen atoms show a closely packed arrangement.

If the system is not fully polymerized, only NBOs contribute to the coordination number increase at lower pressure. Only at high pressures, once all NBOs are consumed, BOs also become involved in the formation of high-coordinated species, which is described as energetically more costly (Wolf and McMillan, 1995) and involves also the formation of oxygen atoms bonded to three Si atoms (threefold coordinated O atoms).

At the conditions of the Earth's mantle silicate melts exhibit high compressibilities due to large variety of structural compression mechanisms that characterize these molten systems, in contrast to their crystalline counterparts (Wolf and McMillan, 1995). Compression induced structural changes in silicate melts at conditions of the deep Earth mantle have been studied experimentally mostly on simple end-member glasses like SiO_2 (e.g. Benmore et al.,

2010; Meade et al., 1992; Prescher et al., 2017; Sato and Funamori, 2010) or GeO_2 (Baldini et al., 2010; Hong et al., 2014; Itié et al., 1989; Kono et al., 2016; Vaccari et al., 2009), which is commonly used as a structural and chemical analogue for SiO_2 (Itié et al., 1989; Wolf and McMillan, 1996). By using simple oxide glasses, two strong approximations are involved in the derivation of the structural properties of melts: glasses as analogues for melts, and simple oxides as analogues for compositionally complex systems. In various experimental works, usually synchrotron based techniques were used, most commonly X-Ray Diffraction (XRD), X-Ray Absorption Spectroscopy (XAS), Inelastic X-Ray Scattering (IXS) (Baldini et al., 2010; Benmore et al., 2010; Hong et al., 2014; Itié et al., 1989; Kono et al., 2016; Lelong et al., 2012; Petitgirard et al., 2017; Prescher et al., 2017; Sato and Funamori, 2010; Vaccari et al., 2009), but also X-Ray Emission Spectroscopy, XES (Spiekermann et al., 2019) and Brillouin Scattering (Murakami and Bass, 2010). While there is no full consistency in the pressure range of the onset of the structural changes, and in the pressure of the completion of the octahedral coordination of Si or Ge, most studies on amorphous GeO_2 and SiO_2 agree about the smooth and gradual transformations from 4- to 6-fold coordination. Only a few experimental works reported also about the existence of the 5-fold coordination state (Guthrie et al., 2004; Lelong et al., 2012), supported by several molecular dynamics (MD) studies (Marrocchelli et al., 2010; Micoulaut, 2004). The inconsistencies in the pressure range of the onset of the changes and in the completion of the octahedral coordination might be related to the variety of applied techniques, differences in the experimental setups, as well as in the differences in the data quality. In GeO_2, the onset of the transformation is usually reported in the pressure range between $\sim$6 and 13 GPa (Baldini et al., 2010; Hong et al., 2014; Vaccari et al., 2009). The completion of the octaheral coordination of Ge has been usually set somewhere between 20 and 30 GPa (Baldini et al., 2010; Hong et al., 2014; Kono et al., 2016; Spiekermann et al., 2019). In SiO_2 glass, due to smaller cation to anion ratio, both the onset of the structural transformations and the completion of the octahedral coordination have usually been observed at comparably higher pressure. The onset of the structural changes has been reported at various pressures between $\sim$8 and $\sim$30 GPa (Benmore et al., 2010; Murakami and Bass, 2010; Petitgirard et al., 2017; Prescher et al., 2017), whereas the completion of the sixfold coordination was observed at pressures between 30 and 60 GPa (Benmore et al., 2010; Murakami and Bass, 2010; Petitgirard et al., 2017, 2019; Prescher et al., 2017; Sato and Funamori, 2010). Even though there is a large inconsistency in the pressure range for the onset of the structural changes, as well as in the completion of the octahedral coordination of Si, more recent studies provide more reliable and robust results (Petitgirard et al., 2017, 2019; Prescher et al., 2017). According to these works the onset of the transformations is located between 15 and 25 GPa, and the completion of the sixfold coordination at about 60 GPa.

To reach conditions more authentic for the deep mantle, a few authors performed studies on more complex compounds probed at high pressure and temperature conditions (Pohlenz et al., 2018; Sanloup et al., 2013). For tracking of the structural evolution and the densification mechanism at the conditions of the deep mantle, particularly important is the work by Sanloup et al. (2013) on molten basalt up to 60 GPa and in the temperature range between 2200 and 3200 K using XRD. The structural changes around Si were set in the pressure range between 10 and 35 GPa. Some complementary molecular dynamics simulation (MD) studies on complex basalt and anorthite glasses up to megabar pressures and at temperatures of up to 6000 K (Bajgain et al., 2015; Ghosh and Karki, 2018) support experimentally reported findings by Sanloup et al. (2013). The MD studies tracked not only the behavior of network forming components (Si and Al) in basaltic or anorthitic compositions, but also of Ca, showing that the strongest changes around all probed atoms occur within the first 20 to 30 GPa. These studies provide important insight into the structural behavior of complex silicate melts at the conditions of the Earth's interior, but further investigations are needed, especially given the

pressure range covered by Sanloup et al. (2013) that gives no insight about the state of the melt at the lowermost mantle conditions. Moreover, knowledge about the structural behavior of the basaltic composition under compression at room temperature is so far missing, which is why reported structural behavior cannot be explicitly attributed to compositional or thermal effects. Apart from this, a more sensitive local structural probe such as XAS could provide more reliable information, rather than XRD, which can track only average global structural properties. MD studies are a highly valuable complementary approach to elucidate structural information, where temperatures of 6000 K also reduce the reliability of the results. The mentioned MD studies provide so far the only insights into the structural evolution of network forming cations in silicate melts at conditions exceeding the shallow upper mantle (Pohlenz et al., 2018). Therefore, further investigations on not only network forming, but also on network modifying elements are needed at the conditions relevant for the deep Earth's interior.

The goal of this work was to track structural properties around network forming and network modifying cations in complex alumino-silicate and alumino-germanate glasses and melts at the conditions corresponding to the entire mantle. We performed detailed and multiple investigations of the local coordination environment in complex aluminosilicate and aluminogermanate glasses and melts as a function of pressure at room, and at high temperature. For this we conducted *in-situ* experimental XAS studies coupled to high-pressure (and high temperature) instrumentation. To generate high pressure conditions of up to megabar pressures in the studied samples, we used diamond anvil cells (DAC), whereas high temperatures were reached using resistive heating (RH) for moderate temperatures (up to $\sim$ 900 K) and laser heating system (LH) for ultra-high temperatures of up to 5000 K. XAS is a leading element specific tool for probing local atomic environment. However, in combination with high-pressure instrumentation such as DAC it cannot be used to directly probe most of the geologically relevant elements such as Si, Ca, Al, Na and others due to the low absorption edge energies of these elements. To probe the K edge of Si, X-ray photons of 1.8 keV must be used. If a Si bearing sample is enclosed in the DAC apparatus, the entire incident photon intensity would be absorbed by the diamonds, which prevents direct probe of Si and other light elements using *in-situ* high-pressure XAS. To circumvent these experimental barriers, usually synthetic samples are used, where elements of interest are fully or partially substituted by some other elements that have been proofed to be suitable chemical and structural analogues, but that have high enough absorption edge energies in order to be directly probed within *in-situ* XAS experiments coupled to the DAC.

In this thesis the concept of element substitution was followed. Therefore, synthetic glasses were used where network-forming Si was partially or fully substituted by its structural and chemical analogue Ge, and network modifying cations (Ca, Mg) were partially substituted by Sr. In particular, we probed Ge-albite glass composition $NaAlGe_3O_8$, where Ge fully substitutes Si, as well as albite glass ($Na_{0.5}Sr_{0.5}Al_{1.5}Si_2Ge_{0.5}O_8$) where Ge and Sr are doped in minor concentrations to partially substitute network forming (Si) and network modifying metals (Ca, Mg), as well as trace elements. These two nominally fully polymerized glass compositions, representing simplified granitic melt compositions, were probed at room temperature up to 131 and 40 GPa, respectively. Even though the albite composition is not compatible with deep mantle melts, it is a first step away from commonly studied simple oxides SiO_2 and GeO_2 and allows tracking the compositional effects on the compression mechanism in fully polymerized systems. The third and central glass composition studied here is the albite-diopside glass ($Na_{0.45}Ca_{0.1}Mg_{0.05}Sr_{0.5}Al_{1.35}Si_{1.95}Ge_{0.5}O_{7.8}$) that was partially doped with minor concentrations of Ge and Sr. It was probed at room temperature up to 164 GPa, as well as at different high-pressure and high-temperature settings up to a maximum 48 GPa, and up to about 5000 K. This partially depolymerized peralkaline glass serves as a rough approximation for basaltic melt

compositions, that can be formed at various depths of the Earth's mantle and that were among others proposed as a potential candidate to explain the origin of the ULVZs at the CMB (Andrault et al., 2014; Pradhan et al., 2015). With this collection, this thesis provides systematic insights into the structural evolution of both, network forming and network modifying components in the melts at the conditions relevant for the deep planetary interior.In the following paragraph a brief overview of the manuscripts presented in the next chapters is provided.

In Chapter 2, the role of the chemical composition on the compressibility of silicate/germanate glasses was studied using XAFS. In particular, we performed a detailed and profound EXAFS study on the spectra collected at the Ge *K* edge of $NaAlGe_3O_8$ at room temperature and up to 131 GPa. The details about the experimental approach, experimental setup and the data analysis are described in Chapter 2. The main objective was to track the effect of increased chemical complexity on a fully polymerized system. The data presented and discussed in Chapter 2 show that increased chemical complexity, in particular Na and Al, considerably influence the densification mechanism of the fully polymerized systems, and that compared to pure SiO_2 and GeO_2 glasses, the studied complex glass exhibits much higher compressibility, especially at the pressures above the completion of the octahedral coordination. In Chapter 3 an extensive EXAFS study on Ge and Sr *K* edges in Ge and Sr doped complex aluminosilicate glasses under compression was studied. Thus, here not only the influence of the network modifying cations on the densification process of Ge was investigated, but also structural transformations around network modifying metals under compression. Because monitoring elements Ge and Sr were only minor elements partially substituting major network forming and network modifying cations Si, Ca, Na and Mg, an additional goal of this work was to identify potential roles of the presence of Si on the structural transformation of Ge. Two glass compositions were studied: Ge and Sr doped modified albite compositions, and Ge and Sr doped albite-diopside glass composition. Here albite-diopside as a simplified basaltic melt composition provided important geological implications for the melt properties in the lower mantle conditions, which is discussed in Chapter 3. In Chapter 4 the role of the temperature in the structural transformation of complex aluminosilicate glasses and melts was studied. For this, Ge *K* edge of albite-diopside glass was probed performing *in-situ* high-pressure and high-temperature XAS experiments with a primary focus on the XANES region due to strong attenuation of the EXAFS signal at high temperatures. That study provided important implications about the influence of the temperature on the structural transformations at the conditions of the upper lower mantle with maximum pressure of 48 GPa and with temperatures extending up to 5000 K. Apart from the implications for the melt properties at the lower and lower most mantle conditions, potential implications for the solubilities of noble gases in the melts could be derived based on the knowledge from the data presented in Chapter 4 and supported by the data provided in Chapter 2 and 3.

Chapter 2

Ge coordination in $NaAlGe_3O_8$ glass upon compression to 131 GPa

Pubplished in:
Physical Reveiw B, 101, 214103 (2020)

Ge coordination in $NaAlGe_3O_8$ glass upon compression to 131 GPa

Marija Krstulović[1,2], Angelika D. Rosa[1], Nicole Biederemann[2,3], Georg Spiekermann[2], Tetsuo Irifune[4], Manuel Muñoz[5] and Max Wilke[2]

[1]*European Synchrotron Radiation Facility, ESRF, 71 Avenue des Martyrs, 38000 Grenoble, France*

[2]*Institute of Geosciences, University of Potsdam, Karl-Liebknecht-Strasse 24–25, 14476 Potsdam-Golm, Germany*

[3]*European XFEL, Holzkoppel 4, 22869 Schenefeld, Germany*

[4]*Geodynamics Research Center, Ehime University Johoku Campus, 2–5 Bunky-ocho, Matsuyama, Ehime 790–0826, Japan*

[5]*Géosciences Montpellier, Université de Montpellier, CNRS, Montpellier, France*

(Received 20 December 2019; revised manuscript received 12 May 2020; accepted 13 May 2020; published 4 June 2020)

Structural transformations at high pressure in $NaAlGe_3O_8$ glass were investigated by means of x-ray absorption spectroscopy at the Ge K edge in combination with a diamond anvil cell. The obtained results provide a detailed picture of the local structural behavior of Ge in a chemically complex glass under compression. First and second shell bond distances ($R_{\text{Ge-O}}$ and $R_{\text{Ge...Ge}}$) were extracted assuming contributions of two scattering paths (Ge-O and Ge ...Ge). We observed a significant extension of the Ge-O distance from 1.73 to 1.82 Å between 3 and ∼26 GPa, accompanied by an increase of the fitted number of nearest neighbors from ∼4 to ∼6. These observations can be attributed to the change from tetrahedral to octahedral Ge coordination. Second shell bond distances Ge...Ge are also consistent with this structural transformation. Between 34 and 131 GPa, the evolution of the fitted Ge-O distance implies a gradual volume reduction of the Ge octahedra. At the highest probed pressure of 131 GPa a Ge-O distance of 1.73 Å was found, which is similar to the one obtained at ambient conditions for Ge in fourfold coordination. The compressibility of the Ge-O octahedron in $NaAlGe_3O_8$ beyond 34 GPa is considerably higher than the one reported for amorphous GeO_2 from x-ray diffraction analysis but it is similar to the one reported for the Ge octahedron in crystalline rutile-type GeO_2 . We attribute the high compressibility of the Ge-O bond in $NaAlGe_3O_8$ glass to the presence of Al and Na that increase the system's complexity and therefore its degrees of freedom. Beyond 110 GPa the data on $NaAlGe_3O_8$ glass indicate the onset of polyhedral distortion. The performed study provides insights into the structural changes of complex and polymerized germanate glasses or melts at extreme pressure conditions.

DOI: 10.1103/PhysRevB.101.214103

*Corresponding author: krstulov@uni-potsdam.de

2.1 Introduction

Structural properties of germanate glasses under compression have fundamental relevance for our understanding of the compaction mechanism in the polymerized amorphous systems. The questions about the nature of the amorphous-amorphous transitions in germanates is of significant importance in the glass theory, condensed matter physics and chemistry. Germanates are of particular interest in Earth sciences as germanates are considered to be chemical and structural analog materials for silicates, the most abundant mineral group of the Earth's mantle and crust. Their structural proximity to silicate melts makes them suitable analogs for the study of natural melts, including studies at extreme pressure conditions.

Multicomponent silicate melts, and in analogy also germanate melts, are challenging to understand due to complex reciprocal influences of their constituents on the overall physical and chemical melt properties. An important descriptor of this family of melts, that links the structural to the physical properties, is the degree of polymerization of Si$-O_4$, Al$-O_4$ and Ge$-O_4$ tetrahedra, the main structural units. The degree of polymerization is related to the ratio between oxygen atoms that are bonded to at least two Si/Ge/Al atoms (bridging oxygens, BOs) and those that are bonded to only one Si/Ge/Al atom (nonbridging oxygen atoms, NBOs). From the perspective of the Si/Ge/Al-polyhedron the degree of polymerization is linked to the number of NBOs that these units contain [1]. At low and moderate pressures, the degree of polymerization of tetrahedral units is commonly described as Q^n species, where n corresponds to the number of BOs with n consequently varying between 0 and 4 [1,2]. In pure SiO_2 glass/melt all oxygen atoms are BOs, thus all Si tetrahedra are Q^4 species. In more complex silicate or aluminosilicate glasses that contain also alkali or alkaline earth cations, the dominant Q^n species depends on the abundance of the specific alkali or alkaline earth component and usually a variety of Q^n species is present. While each alkali or alkaline earth component will influence the physical properties of the system in a different way, generally the higher their content, the larger the abundance of smaller n values [1]. As these cations break connections between Si/Ge/Al-tetrahedra, they may have significant influence on the compressional behavior of multicomponent melts and glasses and thus on their physical and chemical properties at high pressure. The influence of depolymerizing components on the compaction mechanism of polymerized and partially depolymerized silicate glasses and melts particularly for pressures up to 5 GPa has been summarized and elucidated in detail in the work by Wolf and McMillan [1]. Many of these studies were performed on melts quenched from high pressure and temperature with subsequent measurements on the glass by various techniques. Important insights were derived from vibrational spectroscopy and magic-angle spinning nuclear magnetic resonance (see Wolf and McMillan [1] and Stebbins [2]). *In-situ* investigations at higher pressures were still relatively scarce at that time because of the experimental difficulties, but insights especially by vibrational spectroscopy, were already reported. The study by Williams and Jeanloz [3] reports on structural changes in amorphous SiO_2 , $CaMgSi_2O_6$, and $CaAl_2Si_2O_8$ up to 31 GPa. It has been shown that structural changes in $CaAl_2Si_2O_8$ begin at lower pressure compared to SiO_2 and $CaMgSi_2O_6$, which was related to the presence of Al in $CaAl_2Si_2O_8$. One year later in a pioneering work, Itié et al. [4] studied the coordination change of Ge in GeO_2 up to 20 GPa using x-ray absorption fine-structure (XAFS) technique. Following this study most of previous experimental studies performed at pressures above 7 GPa have been focused on pure oxide compositions GeO_2 [5–7] and SiO_2 [8,9]. These studies provided precise information on the compression behavior of (Ge/Si)O_4 tetrahedra that build the polymeric network at ambient conditions by corner-sharing. Under compression the coordination of Si and Ge changes from tetrahedral to octahedral, and the linkage of these polyhedra changes from corner- to edge-sharing. This transformation is accompanied by the change of oxygen from two- to threefold

while still keeping the ideal ratio between the Ge nonbonded radius to the Si/Ge-O bond length [10]. In the picture of the theory of O'Keeffe and Hyde on nonbonded forces in crystalline and noncrystalline matter, this is the main driving force for the change in local structure and not the closer packing of oxygens. The repulsive Ge...Ge or Si...Si interactions are also responsible for relatively loosely packed structures of silicates and germanates at ambient conditions.

Despite the fact that amorphous GeO_2 and SiO_2 have been the most studied systems, uncertainties persist on the character of the transition from four- to sixfold (smooth or abrupt) [11,12], the possible existence of a fivefold intermediate coordination state [1,6,11,13,14] and the completion pressure of the four- to sixfold transition [7,15–17]. In some recent studies on GeO_2 and SiO_2 glasses, covering pressures beyond 90 GPa, the appearance of a coordination number higher than six was discussed [9,15,18,19]. The discrepancies between previous studies can be attributed principally to different experimental probe techniques, including x-ray absorption spectroscopy (XAS) and x-ray diffraction (XRD), Brillouin scattering spectroscopy and near-edge spectroscopy by x-ray Raman scattering (XRS). These techniques exhibit a different sensitivity ranging from local changes (XAS, XRS) to bulk observations (XRD, Brillouin). Other sources that could lead to the present disagreements might be the apparent differences in the experimental setups (beamline properties, sample environment) as well as sample synthesis methods.

Only few studies investigated the structural changes in chemically more complex glasses and melts to higher pressures. Among them, Sanloup et al. [20] reported on the Si coordination change in molten basalt up to 60 GPa and ∼3200 K. This work revealed that the coordination change in basalt is shifted to lower pressures at high temperature compared to glassy SiO_2 which might be explained by the higher chemical complexity and/or temperature [8,21].

In this work, we investigated in detail the structural response of $NaAlGe_3O_8$ glass up to 131 GPa at room temperature. This glass represents a nominally fully polymerized structure (as GeO_2) due to the coupled substitution of Na and Al for one Ge per formula unit. The coupled substitution of Ge by Na and Al is a first step to increase the complexity of the system while still preserving the polymerization of the tetrahedral network. Notably, the coupled substitution leads to a higher variation of the oxygen-cation bond length and cation-oxygen-cation angles compared to the pure oxides [1]. In our view, this is an ideal way to improve our understanding of compositional effects on the compressional behavior of glasses up to extreme pressures in a systematic way. We performed XAS measurements in this material to determine the atomic environment of Ge, i.e., coordination number and interatomic distances. The composition is in analogy to the naturally occurring tectosilicate mineral albite, $NaAlSi_3O_8$. Replacing Si by Ge allows for probing the local structure by XAS using a diamond anvil cell (DAC). Low x-ray energies that need to be applied to study light elements like, e.g., Si, Al, Na, Mg, or K are not compatible with high pressure cells. Another advantage of germanate glasses is the fact that structural transitions are shifted to lower pressures compared to silicates [1,4], making the high-pressure phases/state more easily accessible. Even though not all observations on germanates can be completely transferred to silicates [1], this study provides valuable insight to this class of compounds at extreme pressures, in general. Using XAS and a DAC equipped with nanopolycrystalline diamonds [22,23] allowed acquiring high-quality extended x-ray absorption fine structure (EXAFS) spectra up to a k-range of 13 $Å^{-1}$. Particularly, changes in the first and second coordination shell, i.e. bond distances ($R_{\text{Ge-O}}$ and $R_{\text{Ge...Ge}}$) could be followed. Our results suggest, that the onset of the four- to sixfold coordination is slightly shifted to lower pressures and the transformation pressure interval is enlarged compared to observations in pure GeO_2 glass. By using the concept of polyhedral bulk modulus by Hazen and Finger [24,25], we show that the octahedrally coordinated Ge in

amorphous $NaAlSi_3O_8$ preferably undergoes compression up to 110 GPa without polyhedral distortion in contrast to amorphous GeO_2 .

2.2 Methods

2.2.1 Sample synthesis

The $NaAlSi_3O_8$ glass was synthesized at high temperature using as a starting material a mixture of oxide and carbonate powders in appropriate proportions. Powders were first mechanically homogenized by manual mixing and grinding in an agate mortar for about 5–10 min. The mixture was then placed in a Pt crucible with a Pt lid to prevent devolatilization of alkalis and germanium at high temperatures. The mixture was first annealed at 1050 °C for decarbonization and then heated up to 1600 °C for 15 h to ensure homogenization of the melt. The Pt crucible was then removed from the furnace and it was immediately immersed in water at ambient temperature in order to quench the melt and to avoid crystallization. This procedure leads to high quenching rates of 400 °C/s favoring a homogeneous glass formation [26]. Raman spectra confirmed the glassy nature of the material.

2.2.2 High-pressure XAS experiments

XAS measurements were performed at the micro-XAS station of the beamline BM23 at the European Synchrotron Radiation Facility (ESRF, France) [27]. Two experimental runs on two individual sample loadings were performed, one up to 46 GPa (run 1) and one extending over the pressure range from 14 to 131 GPa (run 2). A double crystal monochromator equipped with two Si(111) crystals in fixed exit geometry was employed for monochromatizing the incoming beam. The x-ray beam was focused down to 5×5 µm^2 using two Pt coated mirrors inclined to 4 mrad in Kirkpatrick-Baez (KB) geometry that served also as harmonic rejection mirrors. Only for the first run, two Rh coated mirrors in fixed exit and total reflection geometry inclined to 3 mrad, were included in the optical path of the x-rays between the monochromator and the KB-system for additional rejection of higher harmonics. The EXAFS spectra were acquired in transmission mode by scanning the incoming energy across the Ge K edge. X-ray beam intensity variations before and after the sample were determined by using ionization chambers filled with appropriate gas mixtures. The energy to monochromator angle was calibrated before and during the experiment using a reference Pt foil placed between the second and third ion chamber. For high-pressure generation, membrane driven Le Toullec-type [28] DACs equipped with nanopolycrystalline diamond anvils were employed [22,23], provided by PRIUS, Geodynamics Research Center, Ehime University, Japan.

2.2.3 EXAFS analysis

EXAFS spectra were collected up to 16 Å^{-1} with a dwell time of 2 and 3 s for run 1 and 2, respectively. The collected EXAFS data were analyzed by the software package XAFS [35]. The background below the Ge K edge was subtracted from the spectra by fitting a polynomial function to the pre- edge region (from 11 049 to 11 080 eV). The edge position (E_0) was fitted by a combination of an error function and a Gaussian function. The error function was used to determine the edge position and the edge jump for normalization. The normalized spectra

were converted from energy into the k space $\chi(k)$. The EXAFS signal (post-edge region) was obtained as $\chi(k) = (\mu - \mu_0)/\mu_0$, with μ as the absorption coefficient and μ_0 was fitted using a smoothing spline function with typically eight knots that were found in order to best minimize low frequencies after background subtraction. EXAFS spectra were k^3 weighted for analysis. The final k range used for later analysis extended up to 13 Å^{-1}. The Fourier transform of the EXAFS function k^3 $\chi(k)$ was performed applying a Kaiser-Bessel window and without phase-shift correction. EXAFS data modeling was performed on unfiltered data. For this analysis, backscattering amplitude and phase shift, as well as photoelectron mean free path, were calculated using the FEFF9 code [36]. The analysis was performed using two coordination shells. In the simplest approach, Ge-O (first) and Ge...Ge (second) coordination shells were used. Two other approaches were tested modifying the contributions to the second shell. This was done by introducing additional scattering paths to the second shell by replacing one Ge by either Al or Na, respectively. The pressure-induced evolution obtained from the latter two approaches did not considerably differ from those of the simple fit model considering Ge-O and Ge...Ge and provided no significant results for Na and Al. In the 6 – 25 GPa pressure range, structural disorder in the second coordination shell was too high to attain significant results and fitting of the second shell was therefore omitted. An undistorted tetrahedral configuration for the first coordination shell calculated using FEFF9 served as input structural model in the fits for the entire pressure range. In the pressure range beyond 40 GPa an octahedral configuration was tested but did not provide any significant difference for the fitted parameters, indicating that fit results are independent from the input structural model. The contribution of the second coordination shell was fitted using tetrahedral configuration for pressures up to 3 GPa. Above 25 GPa an octahedral configuration provided better fit results. The fit interval in k space was 3 - 13 Å^{-1}. An asymmetric distribution for the Ge-O and Ge...Ge pair correlation were determined in the fits using an approach implemented in the XAFS software package by Winterer (1997) [35] see Pohlenz et al. [37] for details. We found that the inclusion of the asymmetry parameter considerably improves the fits in the pressure range between ∼8 and ∼90 GPa, while below 8 and beyond 90 GPa it has a negligible influence on the fit quality. Free fit parameters were the mean bond distances $R_{\text{Ge-O}}$ and $R_{\text{Ge...Ge}}$, Debye-Waller factor $\sigma^2_{\text{Ge-O}}$, and the coordination number for Ge in the first shell ($N_{\text{Ge-O}}$). $N_{\text{Ge...Ge}}$ was constrained to be equal to $N_{\text{Ge-O}}$ in order to reduce the number of fitted parameters. After a first fit with a very small asymmetry parameter (i.e., symmetric distribution), this parameter was iteratively increased until the best fit for each spectrum was obtained. The fit quality was estimated from the χ^2 statistics. The nonstructural parameter ΔE_0, the energy mismatch between theoretical and experimental scales, was treated as a free fit parameter for the Ge-O scattering path. For Ge ...Ge it was constrained to be equal to ΔE_0 obtained for Ge-O value. The amplitude reduction factor S_0^2 was initially constrained to one for all fits by fitting the data set at ambient pressure as well as spectra of crystalline GeO_2 in quartz and rutile structure. The EXAFS signals of the second experimental run showed systematically reduced amplitudes compared to those of the first run spectra. This mismatch might be related to a slightly higher contribution of higher harmonics due to the absence of the Rh-coated mirrors in this run. We, therefore, used an amplitude reduction factor of 0.92 to fit the second dataset in order to account for the presence of a higher fraction of higher harmonics. This procedure led to similar N values extracted from fits of both runs.

2.3 Results

The normalized absorption spectra in the near-edge region (XANES) are plotted in Fig. 2.1(a) as a function of increasing pressure up to 121 GPa highlighting the shift of the

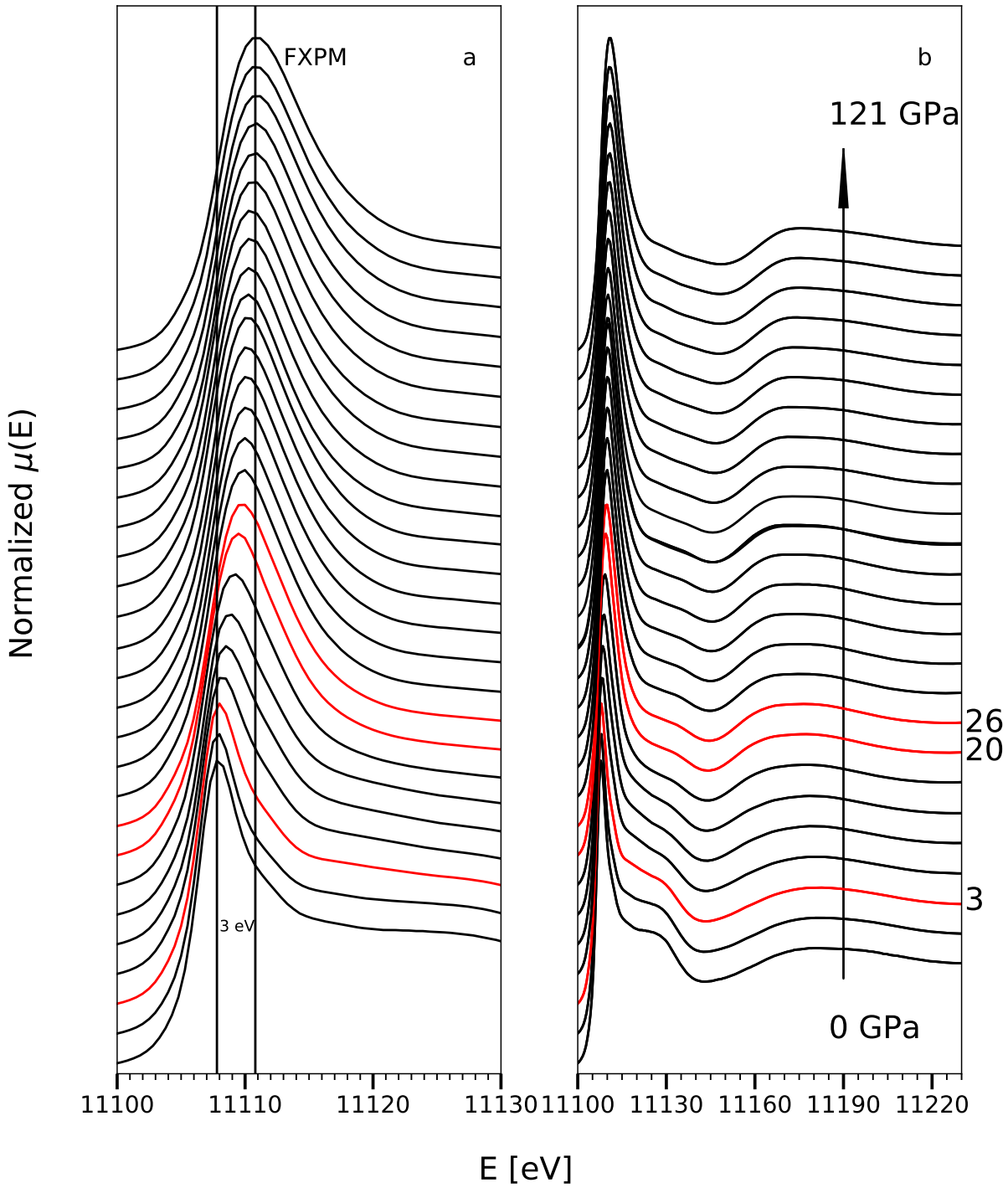

Figure 2.1: Normalized Ge K edge XANES spectra as a function of pressure (1 – 121 GPa). Left side (a) covers the energy range around the first XANES peak maximum (FXPM). The two vertical lines indicate the position of the maximum of the first XANES peak at 0 and 121 GPa, respectively, which exhibits an energy shift of ∼3 eV over this pressure range. Right side (b) covers the extended energy range between first XANES peak maximum up to 11 240 eV, in which changes in the beginning of the EXAFS region are apparent upon compression. All spectra are shifted along the y axis for clarity. Spectra in red color indicate pressure range with the strongest energy shift (see also Fig. 2.2).

first XANES peak maximum (FXPM) between 11 110 and 11 130 eV [Fig. 2.1(a)] and the first EXAFS oscillation [Fig. 2.1(b)] around 11 180 – 11 190 eV. The FXPM energy position was determined by fitting a Gaussian curve to the energy region around the maximum (4, + 1.4 eV). As the pressure increases, the full width half maximum of the first XANES peak increases and its maximum shifts to higher energies. The strongest changes are observed between 3 and ∼26 GPa (highlighted by red spectra). In Fig. 2.1(b) two coupled features can be distinguished in the spectra. While the XANES shoulder around 11 127 eV is very prominent below 3 GPa, it flattens as the pressure increases. As the shoulder flattens the first EXAFS oscillation shifts towards lower energies and its intensity increases. This feature becomes more prominent beyond 26 GPa.

Figure 2.2 reports the energy of the maximum of the first XANES peak (denoted as FXPM in [Fig. 2.1(a)]) as a function of pressure. The total energy shift along the measured pressure range is ∼3 eV. The evolution of FXPM can be divided in four different regions: At low pressures up to 26 GPa the energy position of FXPM increases steeply with pressure. At 26 GPa the slope of the trend flattens considerably until between 60 and 90 GPa it remains almost constant. Above ∼90 GPa the FXPM increases again with pressure while a significant scatter of the data points is apparent.

The k^3 -weighted EXAFS function $k^3\ \chi(k)$ and the corresponding Fourier transform is shown in Figs. 2.3(a) and 2.3(b). Up to ∼20 GPa, the maxima of $\chi(k)$ tend to shift to lower k values. This is pronounced at ∼7 Å^{-1} , and around 9 Å^{-1}. Upon further compression and beyond 80 GPa, in particular the EXAFS oscillations at ∼5 Å^{-1} has a significant broadening. Maxima and minima of oscillations at ∼7 and 9 Å^{-1} shift towards higher k values beyond 20 GPa. This shift is evident between ∼40 and ∼90 GPa and at 9 Å^{-1} as well as at ∼11 Å^{-1} [Fig. 2.3(a)]. In the magnitude of the Fourier transform (R space) of the EXAFS spectra [Fig. 2.3(b)] the main peak at ∼1.3 Å corresponds to the signal coming from the first coordination shell, with O atoms as nearest neighbors. Upon compression, this peak shifts to higher R values (interatomic distances uncorrected for phase shift) and becomes broader. The signal beyond the first coordination shell is rather weak, but increases in intensity with pressure due to progressively enhanced contributions from the second coordination shell. In Fig. 2.4 selected spectra with their corresponding fits are shown covering the fitted k range.

For the interpretation of the data we will show and discuss results of the evolution of the mean bond distances $R_{\text{Ge-O}}$, $R_{\text{Ge...Ge}}$, as well as first shell coordination number $N_{\text{Ge-O}}$. The most reliable parameter for the interpretation of the EXAFS data is the Ge-O distance with an overall uncertainty of ±0.005 Å. N is directly correlated to the amplitude reduction factor S_0^2 which is not precisely known. Furthermore, the bond distance variance σ^2 (values shown in Table 2.1) is also strongly correlated with N. Thus, the overall uncertainty for the N parameter is about ±0.5.

The evolution of the first coordination shell bond distance ($R_{\text{Ge-O}}$) with pressure (Fig. 2.5) shows a very strong increase up to ∼26 GPa (ΔR ∼0.09 Å), whereas between 26 and 34 GPa it is virtually constant (ΔR ∼0.005 Å) given the uncertainties. Beyond 34 GPa the $R_{\text{Ge-O}}$ decreases constantly up 131 GPa (ΔR ∼0.09 Å), whereby its pressure dependence reduces beyond 110 GPa. The coordination number $N_{\text{Ge-O}}$ upon compression is shown in Fig. 2.6. $N_{\text{Ge-O}}$ exhibits first a strong increase from 4.6 to 6.6, from 1 GPa to 26 GPa, respectively. At higher pressures no further significant change is observed, particularly given the uncertainty for this parameter. Fitted values typically vary between 6.0 and 6.5 in that pressure range.

The pressure evolution of the second coordination shell bond distance $R_{\text{Ge...Ge}}$ is shown in Fig. 2.7. Up to 3 GPa, tetrahedral coordination dominates, and the obtained mean bond distance is 3.2 Å, which is in agreement with the reported Ge...Ge bond distance of 3.16

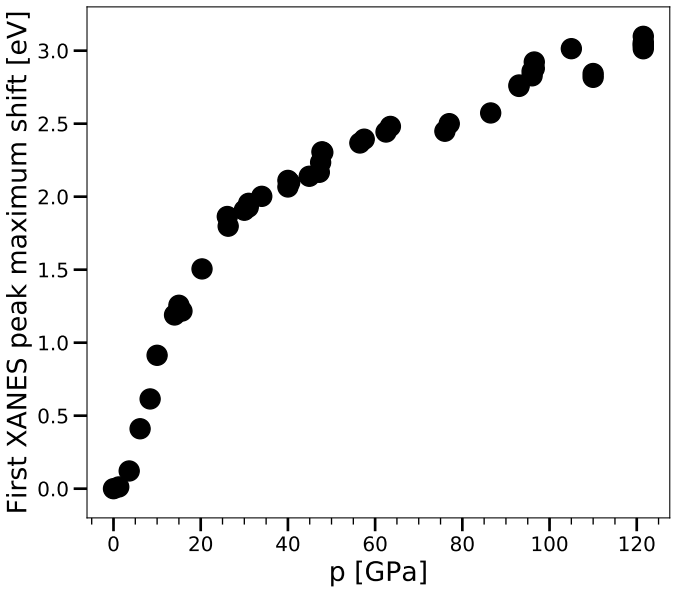

Figure 2.2: Energy shift of the fitted first XANES peak maximum (FXPM in Fig. 2.1) as a function of pressure from 0 to 121 GPa. The point at 131 GPa was not included in this plot due to uncertainties in the energy calibration of the monochromator.

(1) Å in crystalline quartz-type GeO_2 [38]. For the pressure range between 3 and 26 GPa the contribution of the second shell could not be extracted due to the high configurational disorder in the system, this pressure interval is indicated by a grey-shadowed area in Fig. 2.7. Beyond 26 GPa, distances consistent with edge-sharing Ge octahedra could be fitted for the second shell. The Ge-O pair distribution in our fits can be described as symmetric with low degree of anharmonicity at low pressure (< 8 GPa) with the h parameter 0.01 - 0.015 as well as at highest pressures ($> \sim$90 GPa) with an h parameter of 0.02. In the pressure interval between 8 and $\sim$90 GPa the pair distribution is asymmetric (for details see Table 2.1).

2.4 Discussion

Upon compression, the first neighbor mean Ge-O distance of $NaAlGe_3O_8$ glass shows a distinctive increase starting at $\sim$3 GPa (Fig. 2.5), which might be due to the onset of the Ge coordination change from tetrahedral to octahedral. The further progressive and significant expansion of the Ge-O distance up to 26 GPa and the increase in the disorder parameter σ^2 (Table 2.1) of the first shell confirm this interpretation and support the assumption of a continuous increase of the Ge coordination number. Fitted results of the second shell mean Ge...Ge distances are in agreement with tetrahedral coordination and polymerization of tetrahedra via corners up to 3 GPa (Fig. 2.7). Between 3 and 26 GPa no significant contribution of the second shell can be determined, which may be explained by the high static disorder in the material due to possible coexistence of four-, five-, and sixfold-coordinated Ge in this pressure interval. At higher pressures, the fitted Ge...Ge distances are considerably shorter than below 3 GPa. This is consistent with an arrangement of edge-sharing octahedra like in crystalline rutile [39]. Between 26 and 34 GPa, the mean Ge-O distance exhibits almost no change with pressure. This may indicate that the complete conversion to octahedral coordination of Ge and the structural rearrangement from corner- to edge-sharing polyhedra is reached at 34 GPa.

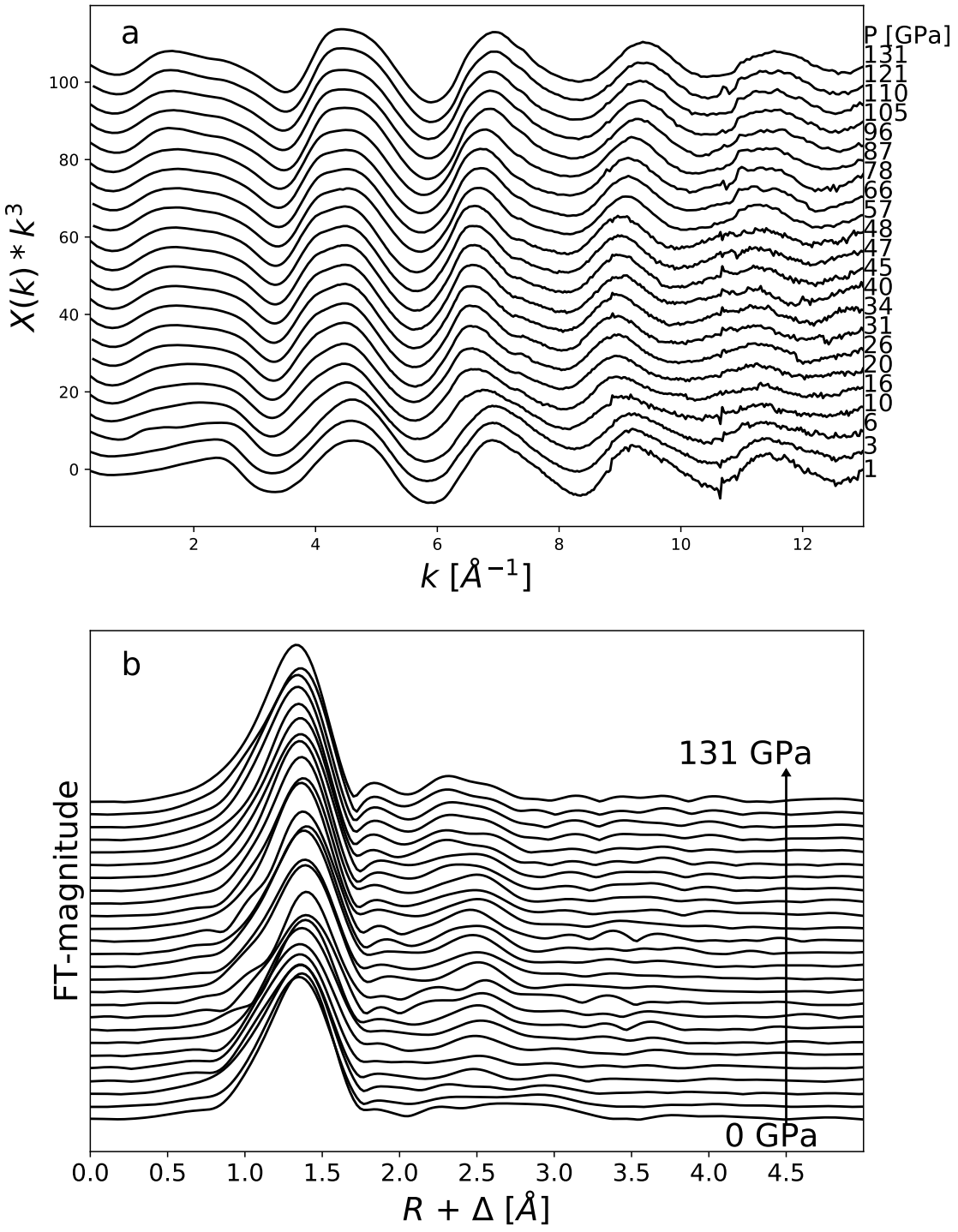

Figure 2.3: (a) Evolution of k^3 weighted EXAFS spectra at the Ge K edge of amorphous $NaAlGe_3O_8$ upon compression to 131 GPa. (b) Magnitude of the Fourier transform (R) of the EXAFS function shown in (a) of amorphous $NaAlGe_3O_8$ to 131 GPa. Plotted data are not corrected for the phase-shift.

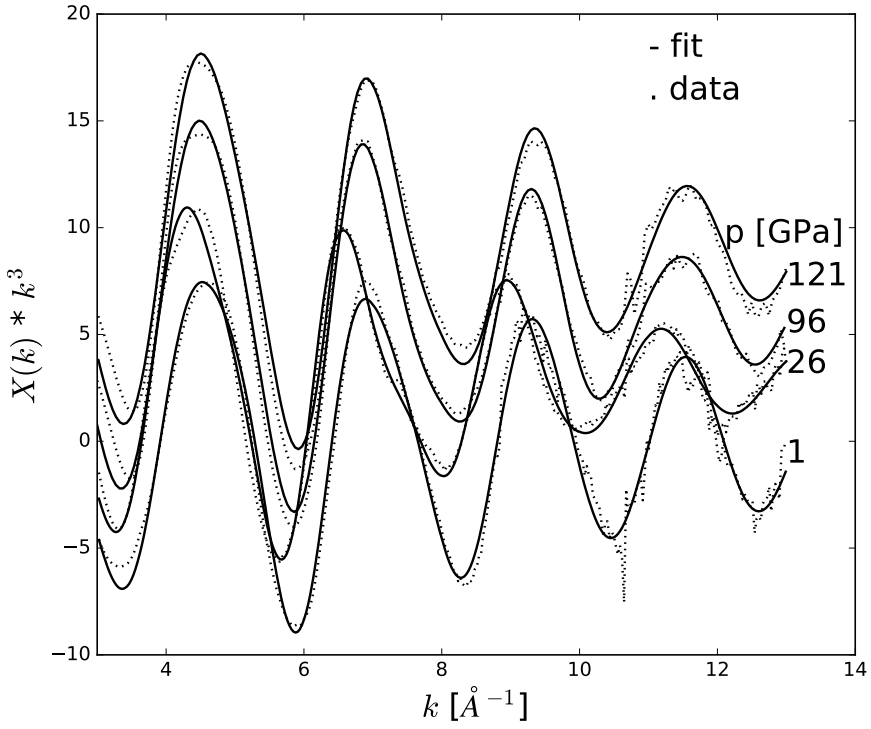

Figure 2.4: Selected k^3 weighted EXAFS spectra of amorphous $NaAlGe_3O_8$ at different pressures and corresponding fits.

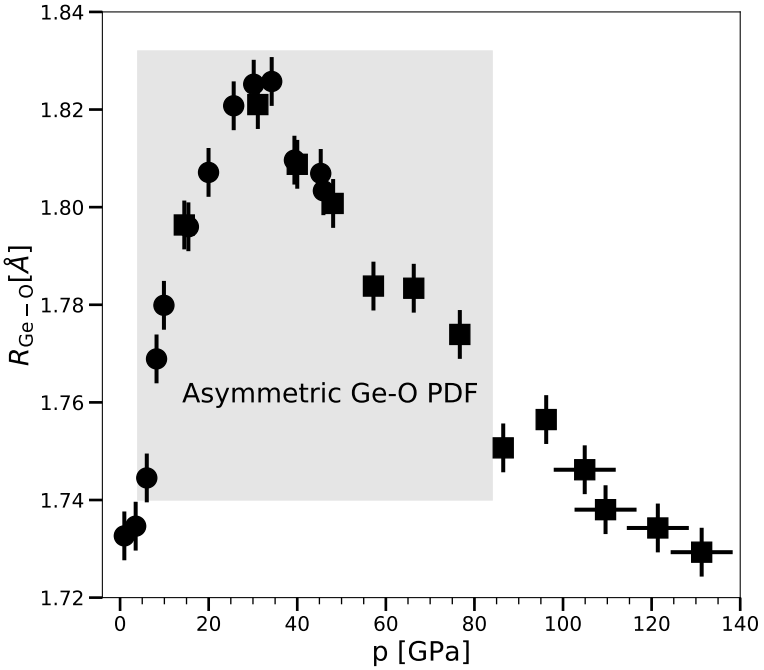

Figure 2.5: Evolution of the average Ge-O distance of the first coordination shell ($R_{\text{Ge-O}}$) of amorphous $NaAlGe_3O_8$ with pressure, obtained from fitting the experimental spectra acquired in run 1 (circles) and run 2 (squares). The grey shaded area presents the pressure interval in which an asymmetric pair distribution function (PDF) was included in the EXAFS analysis.

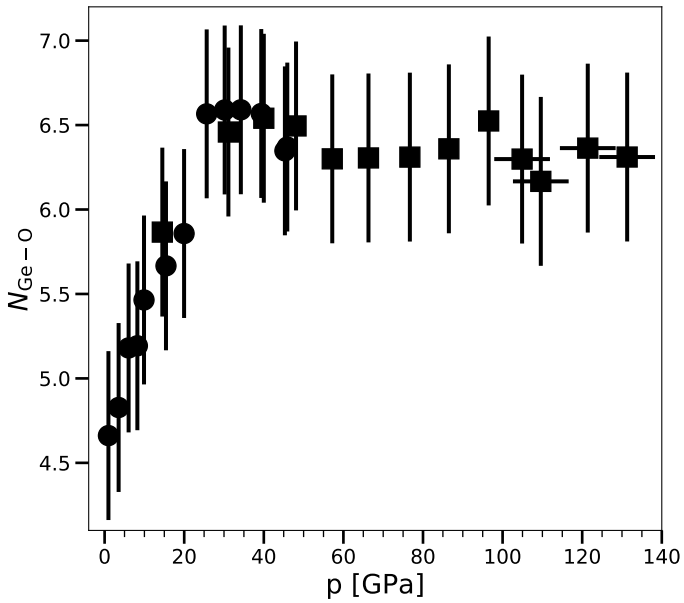

Figure 2.6: Evolution of the fitted number of neighbors of the first coordination shell ($N_{\text{Ge-O}}$) of amorphous $NaAlGe_3O_8$ with pressure. Symbols as in Fig. 2.5.

However, the shift of the FXPM with pressure (Fig. 2.2) indicates a significant change in slope already at 26 GPa and may be taken as evidence that the conversion to octahedral symmetry is already completed around 26 GPa because the XANES region is particularly sensitive to site symmetry. This ambiguity in the data may indicate that the presence of the softer Na-O and Al-O bonds prevents the Ge-O bond length to show a clear turning point in the pressure trend. At pressures beyond 34 GPa, continuous shortening of Ge-O bonds is observed up to 131 GPa with a slight change of the slope beyond 110 GPa.

The mean bond distance presents the most reliable structural parameter extracted from EXAFS. The uncertainty of the fitted N parameter that should describe the number of neighbors has to be considered rather high due to the uncertainty on the nonstructural parameter S_0^2 that also influences the EXAFS amplitude and the correlation of N with the fitted Debye-Waller factor σ^2. Previous studies showed that the bond length can be used as a sensitive probe for the coordination number as they are correlated via the bond-valence theory [37,40–42]. In this theory, the bond valence (s) is directly related to the difference between measured (R) and an empirically determined ideal metal-oxygen bond length (R_0) for a given material according to s = R_0 - $R/e^{0.37}$ [41]. In this sense, the increase of the Ge-O distance during conversion to octahedral coordination is dictated by local charge requirements, because compression of the tetrahedral Ge-O units is not possible, as the bond-valence sum around the oxygen atoms would exceed the ideal value of two [10]. Densification at low pressures in these tectosilicate-like structures is accommodated by rearrangement of the polymerized units and rotation of tetrahedra (e.g., Wolf and McMillan, 1995) [1]. Therefore, further compaction is accommodated by rearrangement from loosely packed oxygen atoms in the tectosilicate structure, to a closest packing of oxygen atoms in a rutile-like structure with an edge-sharing configuration of Ge octahedra. During this conversion, the Ge-O expansion is accommodated by the contraction of the nonbonded or next-nearest-neighbor Ge...Ge distance. The strong repulsion of the Ge...Ge interaction is overcome by high pressure and is compensated by the increase of the oxygen coordination number from 2 to 3, preserving the ideal value for the oxygen bond valence sum. The structural response of these compounds to pressure can be understood through the

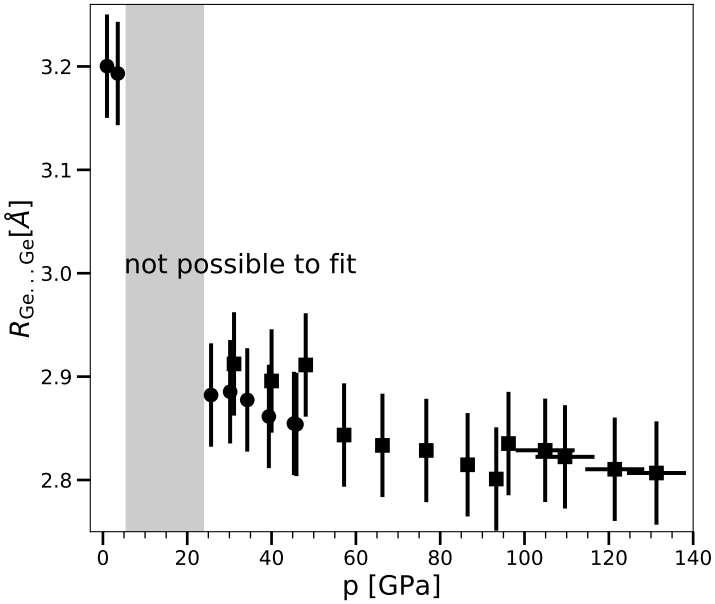

Figure 2.7: Evolution of the second coordination shell distance ($R_{\mathrm{Ge...Ge}}$) of amorphous $NaAlGe_3O_8$ with pressure. Symbols as in Fig. 2.5. The grey shaded area (between 5.3 and 24 GPa) corresponds to the pressure range in which very high structural disorder in the second coordination shell inhibited the EXAFS analysis.

relation between the oxygen coordination number and the ratio of the nonbonded Ge radius R_{GeGe} (1.58 Å) [10] and the bonded Ge-O distance l ($R_{\mathrm{GeGe}}/\mathrm{l}_{\mathrm{Ge\text{-}O}}$), which is developed and described by O'Keeffe and Hyde [10]. At room pressure this ratio is ∼0.91 which meets the requirements for twofold-coordinated oxygen atoms, whereas at 26 GPa and above this ratio is ≤ 0.867, which satisfies the bond-valence requirements of threefold-coordinated oxygen.

In Fig. 2.8 we compare the pressure evolution of the average Ge-O distance for amorphous $NaAlGe_3O_8$ and GeO_2 with the one extracted for rutile-type crystalline GeO_2 . Data for GeO_2 glass were determined by Kono et al. by XRD [15] and by Hong et al. [7] and Baldini et al. [16] by EXAFS. Measured data for crystalline GeO_2 in rutile structure up to 25 GPa were taken from Haines et al. [39]. We used the concept of polyhedral bulk modulus introduced by Hazen and Finger [24,25] to extrapolate the Ge-O distance of octahedrally coordinated Ge in crystalline rutile-type GeO_2 up to a pressure of 130 GPa. For this calculation, we used a third-order Birch-Murnaghan equation with the parameters $K_{T0} = 270$ GPa and $K_0^{'} = 7$ [25]. At ambient conditions, $NaAlGe_3O_8$ and GeO_2 glasses have a similar structure with fully polymerized tetrahedral units connected via corners. Due to its higher chemical complexity, the $NaAlGe_3O_8$ glass has likely a higher structural flexibility than GeO_2 at the same degree of polymerization as only Q^4 species are present in both glasses [1,2]. The data of both glasses, GeO_2 and $NaAlGe_3O_8$, follow roughly similar trends within the first 40 GPa, showing first a significant expansion, followed by a broad maximum and subsequent decrease of the Ge-O distance. The data coverage from EXAFS does not allow an equivalent evaluation of the influence of Al and Na on the onset of tetrahedral-to-octahedral conversion as reported by Williams and Jeanloz [3] for SiO_2 compared to $CaMgSi_2O_6$ and $CaAl_2Si_2O_8$. Assuming that observations made by Williams and Jeanloz [3] can be transferred to germanates, we suggest that the presence of Al in the structure might favor the shift from four- to sixfold coordination at lower pressure. Further, the high compressibility of the large Na cations could allow for taking up large parts of the structural densification. As a result, the Ge-O (and Al-O) bonds

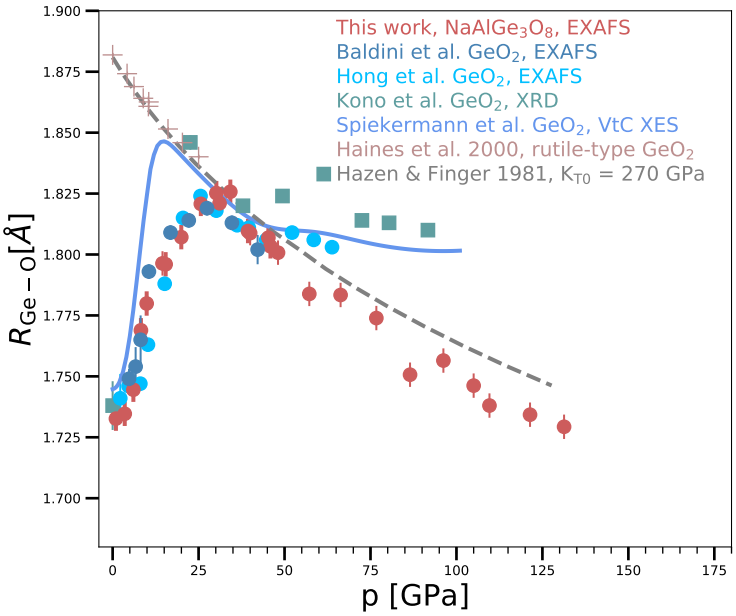

Figure 2.8: Evolution of mean Ge-O distances as a function of pressure for amorphous $NaAlGe_3O_8$ (red symbols) compared to those reported in literature on amorphous GeO_2 (blue symbols) using different probe techniques as indicated (squares for XRD, circles for EXAFS, full line for VtC XES). Data of the mean Ge-O bond length in rutile-type crystalline GeO_2 (sixfold coordinated Ge) are plotted for comparison, including those reported by Haines et al. [39] (brown crosses) and those obtained from extrapolation of the compression data reported in Hazen and Finger [25] using a third order Birch-Murnaghan equation of state with K_{T0} = 270 GPa and $K_0^{'}$ = 7 [24,25] (grey dashed line).

extend, but tetrahedral configuration is preserved. This trend must terminate once the ratio of R_{GeGe}/l reaches the critical threshold and conversion to octahedral coordination starts. These hypotheses could be validated by measurements of the O K edge with x-ray Raman scattering that probes the local structure of oxygen (e.g., Lelong et al. [6], Petitgirard et al. [21]).

Above 40 GPa, the trend of the Ge-O distance in GeO_2 glass levels off, whereas in $NaAlGe_3O_8$ it continuously decreases up to the highest pressure with slight change in the slope above 110 GPa. The pressure evolution of the calculated Ge-O distances using the polyhedral bulk modulus can be considered as the one expected for a homogenously compressed octahedron without any polyhedral distortion. The similarity to the pressure evolution of $NaAlGe_3O_8$ glass implies that an increase of the Ge coordination number beyond 6 in $NaAlGe_3O_8$ glass is unlikely as well as distortion of the Ge coordination polyhedron, at least up to ∼110 GPa. This conclusion is based on the general observation, that an increase of the coordination number should be associated with an increase of the bond length similar to the one observed between 0 and 26 GPa in this study, while polyhedral distortions should result in weaker bond-length reductions with pressure (reduced bond length sensibility with pressure) as illustrated by Spiekermann et al. [19] for GeO_2 glass. This simple comparison of the pressure dependence of the Ge-O distance evidences that there is a strong difference in the compressional behavior of the Ge coordination polyhedron between $NaAlGe_3O_8$ and GeO_2 glass. The weaker shortening of the Ge-O bond distance beyond 110 GPa in $NaAlGe_3O_8$ might indicate the onset of polyhedral distortions similar to those observed for GeO_2 in the α-PbO_2 structure [43].

In the following, we compare the evolution of the relative bond length with pressure

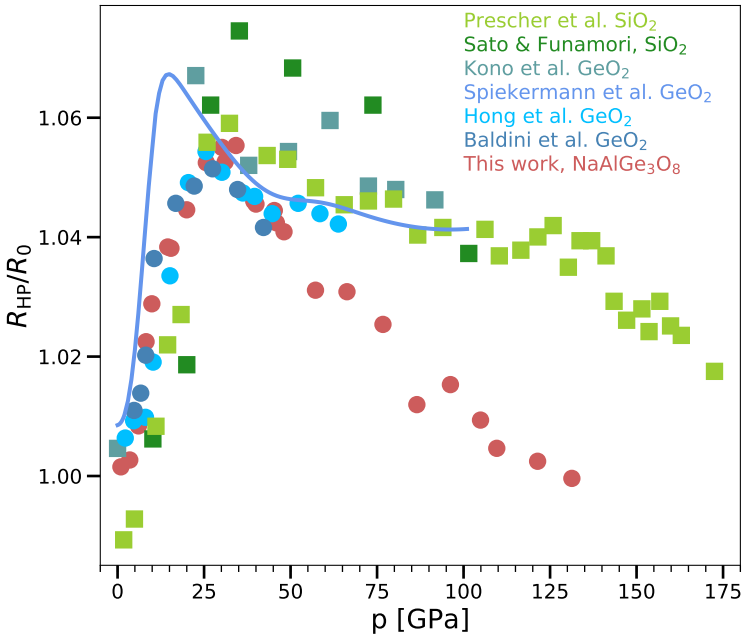

Figure 2.9: Evolution of the normalized Ge-O distance expressed by the ratio R_{HP}/R_{P0} of amorphous $NaAlGe_3O_8$ with pressure from this study (symbols as in Fig. 2.8) compared to literature data on the relative changes of the Si-O distance (green symbols) and Ge-O (blue symbols) distances obtained from XRD (squares), EXAFS (circles), and VtC-XES (full line).

(R_{HP}/R_0) in GeO_2 , SiO_2 and $NaAlGe_3O_8$, which presents the bond length obtained at high pressure normalized to the one at ambient conditions (Fig. 2.9). This approach reduces systematic errors introduced by using different probe techniques and allows a direct comparison of data on Ge and Si. In $NaAlGe_3O_8$ glass, this ratio increases during the coordination change to a maximum value of 1.053 where conversion to octahedral coordination is reached. This value is similar to those reported from XAS studies on GeO_2 glass of 1.054 [7] and 1.051 [16]. In the XRD study by Kono et al. [15] on GeO_2 glass a larger relative expansion of 1.067 was found. In summary, in the first 26 GPa all compared Ge compounds exhibit a consistent evolution with pressure with the exception of the results obtained by XRD. The origin of these discrepancies may reside in the different sensitivities of the probe techniques. For SiO_2 glass, the relative bond expansion during the four- to sixfold conversion covers a slightly larger pressure interval than in GeO_2 and $NaAlGe_3O_8$ glass. A considerably higher bond expansion with a factor of 1.08 is obtained by Sato and Funamori [17], whereas the factor of 1.059 obtained from the data by Prescher et al. [9] is closer to that on GeO_2 glass. The course of the bond distance increase during conversion form four- to sixfold coordination in all compared glass compositions does not necessarily imply the existence of the pure fivefold state. We, however, cannot exclude its presence as a fraction in the mixed-state pressure domain that contains polyhedra with coordination numbers ranging from 4 to 6. The existence of the pure fivefold structure as an intermediate state between four- and sixfold coordination is considered to have significant influence on the rheology of a given melt [1]. In previous studies, pure fivefold coordination was reported as an intermediate phase in SiO_2, but not in GeO_2 glass (see chapter by Wolf and McMillan [1]). In some later studies on GeO_2 glasses the presence of fivefold coordination was reported either as a fraction [6], or as a pure intermediate state [11,13]. The present data do not allow deriving a final conclusion on this topic and it is very likely that evidence to constrain the role of fivefold coordination can only be provided by numerical simulations.

Table 2.1: Values of $R_{\text{Ge-O}}$, $N_{\text{Ge-O}}$, $\sigma^2_{\text{Ge-O}}$, h_{GeO}, $R_{\text{Ge...Ge}}$, $N_{\text{Ge...Ge}}$, $\sigma^2_{\text{Ge...Ge}}$, $h_{\text{Ge...Ge}}$ and χ^2 for first and second experimental run at each pressure step. The given pressure up to 100 GPa presents the average of the pressure measured before and after XAS acquisition on the ruby and the uncertainty was calculated from the standard deviation using the nonhydrostatic EOS [32]. For data points above 100 GPa pressure was determined from XRD on the Re gasket before and after XAS acquisitions using the protocol and EOS of Re from Anzellini et al., 2014 [33]. In addition to the standard deviation we assumed a pressure uncertainty of 7 % for these points, which is related to the absence of a pressure medium in the present experiments.

Run1

P [GPa]	$R_{\text{Ge-O}}$ $R_{\text{Ge-Ge}}$	$N_{\text{Ge-O}}$ $N_{\text{Ge-Ge}}$	$\sigma^2_{\text{Ge-O}}$ $\sigma^2_{\text{Ge-Ge}}$	$h_{\text{Ge-O}}$ $h_{\text{Ge-Ge}}$	χ^2
1 (0.4)	1.733 (3) 3.2 (4)	4.6 (2)	0.0035 (3) 0.021(0)	0.01 0.01	0.886
3.5 (0.2)	1.735 (2) 3.2 (4)	4.8 (1)	0.0047 (3) 0.029 (0)	0.01 0.01	0.659
6 (0.1)	1.745 (2)	5.2 (1)	0.0058 (3)	0.015	0.602
8.2 (0.2)	1.769 (3)	5.2 (2)	0.0050 (3)	0.035	0.622
10 (0.3)	1.780 (3)	5.5 (2)	0.0052 (4)	0.04	0.601
15.4 (0.3)	1.796 (3)	5.7 (2)	0.0055 (4)	0.04	0.639
20 (0.5)	1.807 (3) 2.9 (3)	5.9 (2)	0.0054 (4) 0.021 (0)	0.04 0.04	0.537
25.6 (0.3)	1.821 (3) 2.9 (3)	6.3 (2)	0.0038 (3) 0.020 (0)	0.05 0.04	0.629
30.2 (0.3)	1.823 (3) 2.9 (4)	6.5 (2)	0.0045 (4) 0.02 (0)	0.05 0.04	0.705
34.2 (1.0)	1.825 (3) 2.9 (3)	6.6 (2)	0.0042 (4) 0.02 (0)	0.05 0.04	0.668
39.4 (0.7)	1.810 (4) 2.9 (5)	6.6 (3)	0.0053 (5) 0.02 (0)	0.04 0.04	0.932
45.3 (0.2)	1.807 (3) 2.9 (3)	6.4 (2)	0.0046 (3) 0.019 (0)	0.04 0.04	0.680
45.9 (0.7)	1.803 (3) 2.9 (3)	6.4 (2)	0.0047 (3) 0.02 (0)	0.04 0.04	0.712

Run3

P [GPa]	$R_{\text{Ge-O}}$ $R_{\text{Ge-Ge}}$	$N_{\text{Ge-O}}$ $N_{\text{Ge-Ge}}$	$\sigma^2_{\text{Ge-O}}$ $\sigma^2_{\text{Ge-Ge}}$	$h_{\text{Ge-O}}$ $h_{\text{Ge-Ge}}$	χ^2
14.5 (0.9)	1.796 (3) 2.90 (0.4)	5.9 (2)	0.0044 (4) 0.0217 (0)	0.045 0.045	0.544
31.1 (0.4)	1.821 (3) 2.91 (0.4)	6.5 (2)	0.0030 (4) 0.0157 (0)	0.052 0.06	0.585
40 (0.2)	1.809 (3) 2.89 (0.4)	6.5 (2)	0.0038 (4) 0.0151 (0)	0.045 0.06	0.604
48 (0.7)	1.801 (3) 2.91 (0.4)	6.5 (2)	0.0037 (4) 0.0122 (0)	0.042 0.08	0.624
57.3 (0.2)	1.784 (3) 2.83 (0.4)	6.3 (2)	0.0033 (3) 0.0182 (0)	0.040 0.04	0.620
66.3 (0.3)	1.783 (3) 2.82 (0.4)	6.3 (2)	0.0032 (3)) 0.0185 (0)	0.04 (3) 0.04	0.653
76.7 (0.7)	1.774 (3) 2.81 (0.4)	6.3 (3)	0.0033 (4) 0.0180 (0)	0.040 0.05	0.707
86.5 (0.6)	1.751 (3) 2.80 (0.4)	6.4 (2)	0.0031 (3) 0.0180 (0)	0.020 0.05	0.638
96.2 (0.8)	1.756 (3) 2.84 (0.4)	6.5 (2)	0.0029 (3) 0.0088 (0)	0.04 0.08	0.698
104.9 (2.7)	1.746 (3) 2.83 (0.4)	6.3 (2)	0.0040 (3) 0.0149 (0)	0.03 0.08	0.670
109.6 (4.4)	1.738 (3) 2.82 (0.4)	6.2 (2)	0.0047 (4) 0.0147 (0)	0.02 0.08	0.700
121.4 (5.9)	1.734 (3) 2.81 (0.5)	6.4 (3)	0.0047 (4) 0.0147 (0)	0.02 0.08	0.835
131 (0.5)	1.729 (3) 2.81 (0.5)	6.3 (2)	0.0047 (3) 0.0149 (0)	0.02 0.08	0.730

Beyond 26 GPa, larger discrepancies are apparent in the Ge/Si-O bond compression evolution: The data of Kono et al. [15] as well as those by Spiekermann et al. [19] on GeO_2 glass report a smaller bond length reduction with pressure than the one of $NaAlGe_3O_8$ glass. Data from Hong et al. [7] and Baldini et al. [16] on GeO_2 glass are similar to the one observed for $NaAlGe_3O_8$ up to ∼40 GPa. Between 40 and 65 GPa the trend for GeO_2 glass levels off. Interestingly, the two data sets on SiO_2 differ in their values at pressures above 26 GPa. The study of Prescher et al. [9] exhibits similar pressure evolution as GeO_2 glass [15] along the whole common pressure range, whereas Sato and Funamori [17] reported longer relative bond lengths at given pressures. Compared to $NaAlGe_3O_8$ glass, the two pure oxide glasses exhibit a lower Ge-O bond-length reduction beyond 40 GPa. As already outlined above, we interpret the trend observed for GeO_2 glass to be due to the fact that compression induces considerable octahedral distortion. Due to the similarity, we may speculate that the Si polyhedron in SiO_2 glass undergoes a similar distortion at extreme pressures as reported for amorphous GeO_2. The very low compressibility in glassy GeO_2 and SiO_2 may be attributed to the presence of only highly charged Ge or Si, which may facilitate octahedral distortion due to stronger intercation repulsion [44]. In contrast to pure oxides, the data on $NaAlGe_3O_8$ glass show a trend that may be easily interpreted by mere compression of largely undistorted Ge octahedra. This simpler compressional behavior might be related to the presence of Na and Al. The charge difference between Al and Ge leads to a longer mean bond length for Al-O due to its lower bond strength according to the bond strength theory [41]. Similarly, a significantly larger mean bond length for Na compared to Ge-O can be considered due to its higher coordination number [45]. In contrast to Ge-O, the nonbonded Ge...Ge distance shows only little shortening at pressures beyond the completion of the octahedral coordination (Fig. 2.7). We do admit that describing the second shell in our EXAFS fits with Ge...Ge only represents a simplification. Still, considering the concepts of O'Keeffe and Hyde [10,44,46] we may speculate that after conversion to sixfold coordination at ∼26 GPa, the critical threshold distance between nonbonded Ge...Ge is reached, between two edge-sharing octahedra. Thus, closer packing and overall volume reduction is now achieved by the reduction of the Ge-O, Ge...Al and Ge...Na bond lengths. As an example, one could consider an oxygen atom that links three octahedra, two edge-sharing octahedra, one Ge and one Al, and an adjacent Ge octahedron. Volume reduction, and therefore average Ge-O bond-length reduction, can be achieved via bond angle adjustments, i.e., increase of Al-O-Ge angle and Al-O distance. This would lead to a decrease of the two Ge-O bond distances accommodating the oxygen bond valence, and to reduction of the nonbonded Al...Ge distance that was not yet at its critical threshold value, in contrast to Ge...Ge.

Earlier studies have already shown that aluminosilicate glasses exhibit a distinct structure evolution to the pure silica system [3], e.g., shifting conversion from tetrahedral to octahedral coordination to lower pressure. Addition of Al and Na to GeO_2 leads to an overall decrease of the average bond valence sum of the oxygen atoms in the structure and thus, to a higher structural flexibility that can explain the observed increased compressibility compared to GeO_2. The question at which pressure $NaAlGe_3O_8$ glass will also show polyhedral distortion for Ge cannot be conclusively answered from our data, but the apparent flattening of the bond distance evolution beyond 110 GPa might indicate the onset of octahedral distortion.

The results on the complex fully polymerized $NaAlGe_3O_8$ glass reported here indicate that chemically complex germanate (and in analogy also silicate), glasses will exhibit a structural behavior upon compression that is considerably different from that observed for the pure oxide compositions GeO_2 and SiO_2. The local structure evolution with pressure found in the simple compound studied here provides insight into the compaction mechanism of fully polymerized alkali aluminogermanate glasses. This includes insight into the four- to sixfold amorphous-amorphous phase transition as well as the densification mechanism that acts far

beyond the transition to octahedral coordination. Our observations suggest that glasses or melts with even higher chemical complexity than $NaAlGe_3O_8$ may follow similar trends and are very distinct to the pure GeO_2 system.

Acknowledgments

We thank the anonymous reviewers for their very constructive comments and the editor for fast handling of the manuscript. We are particularly grateful for pointing us to the unique concept of nonbonded forces that seem to have been forgotten in textbooks on crystal chemistry. We thank the entire staff of the beamline BM23 of the European Synchrotron Radiation Facility (ESRF), in particular S. Pascarelli and O. Mathon, for providing us two experimental sessions to perform the experiment. We strongly recognize the technical support provided by F. Perrin and S. Pasternak. We also thank M. Mezouar and G. Garbarino for their help with XRD measurements at ID27. We warmly thank also J. Jacobs from the high-pressure sample environment for his assistance with high-pressure instrumentation, and R. Torchio for providing the measurements on reference samples. M.W. would like to acknowledge funding by DFG through Project Wi 2000/13-1.

[1] G. H. Wolf and P. F. McMillan, Pressure effects on silicate melt structure and properties, in Structure, Dynamics and Properties of Silicate Melts, edited by J. F. Stebbins, P. F. McMillan, and D. B. Dingwell (Mineralogical Society of America, Washington, DC, 1995), Chap. 11, Vol. 32, p. 505.

[2] J. F. Stebbins, Dynamics and structure of silicate and oxide melts: Nuclear magnetic resonance studies, in Structure, Dynamics and Properties of Silicate Melts, edited by J. F. Stebbins, P. F. McMillan, and D. B. Dingwell (Mineralogical Society of America, Washington, D.C., 1995), Chap. 7, Vol. 32, p. 191.

[3] Q. Williams and R. Jeanloz, Spectroscopic evidence for pressure-induced coordination changes in silicate glasses and melts, Science 239, 902 (1988).

[4] J. P. Itié, A. Polian, G. Calas, J. Petiau, A. Fontaine, and H. Tolentino, Pressure-Induced Coordination Changes in Crystalline and Vitreous GeO_2 , Phys. Rev. Lett. 63, 398 (1989).

[5] F. Vannereau, J. P. Itié, A. Polian, G. Calas, J. Petiau, A. Fontaine, and H. Tolentino, Pressure-Induced coordination changes of germanium in crystalline and vitreous germanates, High Press. Res. 7, 372 (1991).

[6] G. Lelong, L. Cormier, G. Ferlat, V. Giordano, G. S. Henderson, A. Shukla, and G. Calas, Evidence of fivefold-coordinated Ge atoms in amorphous GeO_2 under pressure using inelastic x-ray scattering, Phys. Rev. B 85, 134202 (2012).

[7] X. Hong, M. Newville, T. S. Duffy, S. R. Sutton, and M. L. Rivers, X-ray absorp-

tion spectroscopy of GeO_2 glass to 64 GPa, J. Phys. Condens. Matter 26, 035104 (2014).

[8] H. Fukui, M. Kanzaki, N. Hiraoka, and Y. Q. Cai, Coordination environment of silicon in silica glass up to 74 GPa: An x-ray Raman scattering study at the silicon L edge, Phys. Rev. B 78, 012203 (2008).

[9] C. Prescher, V. B. Prakapenka, J. Stefanski, S. Jahn, L. B. Skinner, and Y. Wang, Beyond sixfold coordinated Si in SiO_2 glass at ultrahigh pressures, Proc. Natl. Acad. Sci. 114, 10041 (2017).

[10] M. O'Keeffe and B. G. Hyde, The role of nonbonded forces in crystals, in Structure and Bonding in Crystals, edited by M. O'Keeffe and A. Navrotsky (Academic Press Inc., New York, 1981), Chap. 10, Vol. 1, p. 227.

[11] D. Marrocchelli, M. Salanne, and P. A. Madden, High-pressure behavior of GeO_2 : A simulation study, J. Phys. Condens. Matter 22, 152102 (2010).

[12] M. Vaccari, G. Aquilanti, S. Pascarelli, and O. Mathon, A new EXAFS investigation of local structural changes in amorphous and crystalline GeO_2 at high pressure, J. Phys.: Condens. Matter 21, 145403 (2009).

[13] M. Guthrie, C. A. Tulk, C. J. Benmore, J. Xu, J. L. Yarger, D. D. Klug, J. S. Tse, H-k. Mao, and R. J. Hemley, Formation and Structure of a Dense Octahedral Glass, Phys. Rev. Lett. 93, 115502 (2004).

[14] T. Sato, N. Funamori, D. Wakabayashi, K. Nishida, and T. Kikegawa, Coexistence of two states in optically homogeneous silica glass during the transformation in short-range order, Phys. Rev. B 98, 144111 (2018).

[15] Y. Kono, C. Kenney-Benson, D. Ikuta, Y. Shibazaki, Y. Wang, and G. Shen, Ultrahigh-pressure polyamorphism in GeO_2 glass with coordination number > 6, Proc. Natl. Acad. Sci. USA 113, 3436 (2016).

[16] M. Baldini, G. Aquilanti, H. K. Mao, W. Yang, G. Shen, S. Pascarelli, and W. L. Mao, High-pressure EXAFS study of vitreous GeO_2 up to 44 GPa, Phys. Rev. B 81, 024201 (2010).

[17] T. Sato and N. Funamori, High-pressure structural transformation of SiO_2 glass up to 100 GPa, Phys. Rev. B 82, 184102 (2010).

[18] M. Murakami and J. D. Bass, Spectroscopic Evidence for Ultrahigh-Pressure Polymorphism in SiO_2 Glass, Phys. Rev. Lett. 104, 025504 (2010).

[19] G. Spiekermann, M. Harder, K. Gilmore, P. Zalden, C. J. Sahle, S. Petitgirard,

M. Wilke, N. Biedermann, C. Weis, W.Morgenroth, J. S. Tse, E. Kulik, N. Nishiyama, H. Yavas, and C. Sternemann, Persistent Octahedral Coordination in Amorphous GeO_2 up to 100 GPa by K β" X-ray Emission Spectroscopy, Phys. Rev. X 9, 011025 (2019).

[20] C. Sanloup, J. W. E. Drewitt, Z. Konôpková, P. Dalladay-Simpson, D. M. Morton, N. Rai, W. van Westrenen, and W. Morgenroth, Structural change in molten basalt at deep mantle conditions, Nature (London) 503, 104 (2013).

[21] S. Petitgirard, C. J. Sahle, C. Weis, K. Gilmore, G. Spiekermann, J. S. Tse, M. Wilke, C. Cavallari, V. Cerantolla, and C. Sternemann, Magma properties at deep Earth's conditions from electronic structure of silica, Geochem. Persp. Lett. 9, 32 (2019).

[22] T. Irifune, A. Kurio, S. Sakamoto, T. Inoue, and H. Sumiya, Materials: Ultrahard polycrystalline diamond from graphite, Nature 421, 599 (2003).

[23] N. Ishimatsu, K. Matsumoto, H. Maruyama, N. Kawamura, M. Mizumaki, H. Sumiya, and T. Irifune, Glitch-free X-ray absorption spectrum under high pressure obtained using nanopolycrystalline diamond anvils, J. Synchrotron Radiat. 19, 768 (2012).

[24] R. M. Hazen and L. W. Finger, Bulk Modulus-Volume Relationship for Cation-Anion Polyhedra, J. Geophys. Res. 84, 6723 (1979).

[25] R. M. Hazen and L. W. Finger, Bulk moduli and high-pressure crystal structures of rutile-type compounds, J. Phys. Chem. Solids 42, 143 (1981).

[26] D. P. Birnie III and M. D. Dyar, Cooling rate calculations for silicate glasses, J. Geophys. Res., California 91, D509 (1986).

[27] O. Mathon, A. Beteva, J. Borrel, D. Bugnazet, S. Gatla, R. Hino, I. Kantor, T. Mairs, M. Munoz, S. Pasternak, F. Perrin, and S. Pascarelli, Radiation Facility: the general-purpose EXAFS bending-magnet beamline BM23, J. Synchrotron Radiat. 22, 1548 (2015).

[28] R. Letoullec, J. P. Pinceaux, and P. Loubeyre, The membrane diamond anvil cell: A new device for generating continuous pressure and temperature variations, High Press. Res. 1, 77 (1988).

[29] A. D. Rosa, O. Mathon, R. Torchio, J. Jacobs, S. Pasternak, T. Irifune, and S. Pascarelli, Nano-polycrystalline diamond anvils: Key devices for XAS at extreme conditions: their use, scientific impact, present status and future needs, High Press. Res. 40, 65 (2019).

[30] R. Boehler and K. De Hantsetters, New anvil designs in diamond-cells, High Press. Res. 24, 391 (2004).

[31] G. Shen, Q. Mei, V. B. Prakapenka, P. Lazor, S. Sinogeikin, Y. Meng, and C.

Park, Effect of helium on structure and compression behavior of SiO_2 glass, Proc. Natl. Acad. Sci. 108, 6004 (2011).

[32] H. K. Mao, P. M. Bell, J. W. Shaner, and D. J. Steinberg, Specific volume measurements of Cu, Mo, Pd, and Ag and calibration of the ruby R1 fluorescence pressure gauge from 0.06 to 1 Mbar, J. Appl. Phys. 49, 3276 (1978).

[33] S. Anzellini, A. Dewaele, F. Occelli, P. Loubeyre, and M. Mezouar, Equation of state of rhenium and application for ultrahigh pressure calibration, J. Appl. Phys. 115, 043511 (2014).

[34] J. Gonzalez-Platas, M. Alvaro, F. Nestola, and R. Angel, EosFit7-GUI: a new graphical user interface for equation of state calculations, analyses and teaching, J. Appl. Crystallography 49, 1377 (2016).

[35] M. Winterer, XAFS - a data analysis program for materials science in proceedings of the 9th international conference on x-ray absorption fine structure, J. Phys. IV France 7, C2-243 (1997).

[36] J. J. Rehr, J. J. Kas, F. D. Vila, M. P. Prange, and K. Jorissen, Parameter-free calculations of x-ray spectra with FEFF9, Phys. Chem. Chem. Phys. 12, 5503 (2010).

[37] J. Pohlenz, A. D. Rosa, O. Mathon, S. Pascarelli, S. Belin, G. Landrot, V. Murzin, A. Veligzhanin, A. Shiryaev, T. Irifune, and M. Wilke, Structural controls of CO_2 on Y, La and Sr incorporation in sodium-rich silicate - carbonate melts by *in-situ* high P-T EXAFS, Chem. Geology 486, 1 (2018).

[38] M. Micoulaut, L. Cormier, and G. S. Henderson, The structure of amorphous, crystalline and liquid GeO_2 , J. Phys.: Condens. Matter 18, R753 (2006).

[39] J. Haines, J. M. Leger, C. Chateau, and A. S. Pereira, Structural evolution of rutile-type and $CaCl_2$ -type germanium dioxide at high pressure, Phys. Chem. Miner. 27, 575 (2000).

[40] L. Pauling, The principles determining the structure of complex ionic crystals, J. Am. Chem. Soc. 51, 1010 (1929).

[41] I. D. Brown, Recent developments in the methods and applications of the bond valence model, Chem. Rev. 109, 6858'(2009).

[42] S. Simon, M. Wilke, R. Chernikov, S. Klemme, and L. Hennet, The influence of composition on the local structure around yttrium in quenched silicate melts - Insights from

EXAFS, Chem. Geology 346, 3 (2013).

[43] R. Dutta, C. E. White, E. Greenberg, V. B. Prakapenka, and T. S. Duffy, Equation of state of the αPbO_2 and Pa3-type phases of GeO_2 to 120 GPa, Phys. Rev. B 98, 144106 (2018).

[44] M. O'Keeffe and B. G. Hyde, On Si-O-Si configurations in silicates, Acta Crystallogr. B34, 27 (1978).

[45] F. Farges, S. de Wispelaere, S. Rossano, M. Muñoz, M. Wilke, A. M. Flank, and P. Lagarde, Local structures around Si, Al and Na in hydrated silicate glasses, in X-RAY ABSORPTION FINE STRUCTURE - XAFS13: 13th International Conference, edited by B. Hedman and P. Pianetta, AIP Conf. Proc. No. 882 (American Institute of Physics, New York, 2007), p. 214.

[46] B. G. Hyde, Inorganic and mineral structures reconsidered, J. Proc. Roy. Soc. New South Wales 119, 153 (1986).

Chapter 3

Structural changes in aluminosilicate glasses up to 164 GPa and the role of alkali, alkaline earth cations and alumina in the densification mechanism

Pubplished in:
Chemical Geology, 560, 119980 (2021)

Structural changes in aluminosilicate glasses up to 164 GPa and the role of alkali, alkaline earth cations and alumina in the densification mechanism

Marija Krstulović[1,2], Angelika D. Rosa[1], Nicole Biederemann[2,3], Tetsuo Irifune[4], and Max Wilke[2]

[1]*European Synchrotron Radiation Facility, ESRF, 71 Avenue des Martyrs, 38000 Grenoble, France*

[2]*Institute of Geosciences, University of Potsdam, Karl-Liebknecht-Strasse 24–25, 14476 Potsdam-Golm, Germany*

[3]*European XFEL, Holzkoppel 4, 22869 Schenefeld, Germany*

[4]*Geodynamics Research Center, Ehime University Johoku Campus, 2–5 Bunky-ocho, Matsuyama, Ehime 790–0826, Japan*

(Received 29 July 2020; Received in revised form 28 October 2020; Accepted 5 November 2020 Available online 8 November 2020)

Pressure induced structural changes in silicate melts have a great impact on their physico-chemical properties and hence on their behaviour in the deep Earth's interior. In order to gain a deeper understanding we have studied the densification mechanism in multicomponent aluminosilicate glasses (albitic and albit-diopside composition) by means of extended X-ray absorption fine structure spectroscopy coupled to a diamond anvil cell up to 164 GPa. We have monitored the structural modifications from the network-former Ge as well as the network-modifier Sr. Notably, we tracked the evolution of Ge-O and Sr-O bond lengths ($R_{\text{Ge-O}}$, $R_{\text{Sr-O}}$) and their coordination number with pressure. We show that $R_{\text{Ge-O}}$ increases strongly up to about 32 GPa, whereas $R_{\text{Sr-O}}$ increases only slightly up to ∼26 GPa. We assign these extensions to the increase of the coordination number from 4 to 6 (Ge) and from ∼6 to at least 9 (Sr). Upon further compression $R_{\text{Ge-O}}$ and $R_{\text{Sr-O}}$ exhibit a continuous decrease to the highest probed pressure. These bond contractions, notably of $R_{\text{Ge-O}}$, that are continuous and exceed the one observed in pure SiO_2 and GeO_2, reflect a higher structural flexibility of multi-component glasses compared to those simple systems. Particularly, the high fraction of non-bridging oxygen atoms due to the presence of Na, Sr, Ca, Mg in the studied glasses, favours the simple compression of the highly-coordinated polyhedra of Si and Ge at pressure greater than 30 GPa. This is in strong contrast to pure oxides where cation polyhedral distortions govern the densification mechanism of the glass. The results of this study demonstrate that low field-strength alkali and alkaline earth cations, ubiquitous in deep Earth's melts, have a profound influence on the densification mechanism of glasses. Our results provide important constrains for interpreting the observed low velocity anomalies at the Earth's core-mantle boundary that have been, beyond others, referred to the presence of high-density melts. The hypothesis that non-buoyant melts at the Earth's core-mantle boundary can be formed by peculiar structural transformations in melts leading to higher coordination numbers compared to their crystalline equivalents is not supported from the present observations. The present results rather suggest that if velocity anomalies are to be explained by melts, these likely have considerable differences in chemical

composition to the surrounding crystalline phase assemblage.

DOI: 10.1016/j.chemgeo.2020.119980

*Corresponding author: krstulov@uni-potsdam.de

3.1 Introduction

Silicate melts are key agents of planets that govern the global exchange of heat and matter over geological times. They are of prime importance to understand and model the chemical differentiation and cooling history of planets. In the Earth's interior the presence of silicate melts has been deduced mainly from seismic low shear wave velocity and attenuation anomalies that appear across the Earth's mantle and include signals from shallow magma chambers of volcanoes, as well as those related to upwelling plumes and prominent anomalies at the core mantle boundary (Adenis et al., 2017; Andrault et al., 2012; Buffett et al., 2000; Ohtani and Maeda, 2001). The physico-chemical properties of melts at the core-mantle boundary region are of particular interest for mantle and core dynamics as these melts may form at the interface between two radically distinct reservoirs in terms of temperature ($\sim\Delta$T of 1000 – 1500 K) and composition (silicate mantle versus metallic iron core). However, especially at these conditions structural and physical properties of silicate melts remain enigmatic but are fundamental for modelling the chemical and physical behaviour of melts in deep planetary interiors. The silicate melt structure at ambient conditions can be described as an interconnected network of SiO_4 tetrahedra constituting the main structural component. In the pure Si-O system the tetrahedra are fully interconnected (polymerized) by bridging oxygen atoms (BOs). In natural and chemically more complex systems the presence of alkali and alkaline earth elements (e.g. K^+, Na^+, Sr^{2+}, Ca^{2+}, Mg^{2+}), as well as other large cations such as Y^{3+} and La^{3+}, depolymerizes the SiO_4 network (Mysen et al., 1985; Pohlenz et al., 2018; Simon et al., 2013). This induces the formation of non-bridging oxygen atoms (NBOs), increases the Si-O bond length distribution and consequently the structural disorder. Elements with a smaller charge than Si may also have a network-forming role, like Al^{3+} or Fe^{3+} in tetrahedral coordination (Ha and Garofalini, 2017; Weigel et al., 2008). The formation of NBOs depends on whether the exchange of network-formers or network-modifiers is charge balanced, so that the network polymerization may persist. It has been shown in previous studies that the physical properties of melts including the degree of structural flexibility and ion-exchange capability can be directly related to the polymerization and thus to the number of NBOs (e.g. Stebbins, 1995). Therefore, the ratio of NBOs relative to BOs can be taken as a prime indicator for the melt structure controlling its physico-chemical properties (Mysen et al., 1985; Wolf and McMillan, 1995). The NBO/BO ratio may also play an important role for the densification of silicate melts with pressure.

At low pressures, particularly highly polymerized glasses/melts show very distinct behaviour with relatively high compressibility due to the structural flexibility of the polymerized network. Further, structural rearrangements in these melts lead to an anomalous decrease in viscosity with increasing pressure (e.g. Wolf and McMillan, 1995). At higher pressures, the SiO_4 tetrahedra become unstable and conversion to octahedral coordination takes place. The coordination change involves a concomitant change of the polyhedral linkage of Si from corner to edge-sharing and an increase of the oxygen coordination number from 2 to 3 (O'Keeffe and Hyde, 1981). The change in coordination allows for a closer packing of atoms while keeping the ideal ratio between the Si non bonded radius to the Si-O bond length (O'Keeffe and Hyde, 1981). For the simplest fully polymerized system, SiO_2, this structural conversion has been reported to take place at different pressure intervals with the lowest pressure of $\sim$8 GPa for the onset of the transformations and the highest pressure of $\sim$60 GPa for the completion of the 6-fold coordination number (Benmore et al., 2010; Meade et al., 1992; Murakami and Bass, 2010; Petitgirard et al., 2017; Petitgirard et al., 2019; Prescher et al., 2017; Sato and Funamori, 2010; Tse et al., 1992).

It has been previously shown that the onset and evolution of this structural conversion depends highly on the composition (Wolf and McMillan, 1995). For instance, the presence of

NBOs (thus network modifying cations) may promote an earlier coordination increase of SiO_4 polyhedra. This is because the consumption of NBOs to increase the oxygen coordination of Si is energetically more favourable than the consumption of BOs (Wolf and McMillan, 1995). A comparative investigation on the structural changes in SiO_2, $CaMgSi_2O_6$ and $CaAlSi_2O_8$ up to 40 GPa provided valuable information on the effect of multiple coexisting cations on the densification mechanism of amorphous silicates (Williams and Jeanloz, 1988). Notably, this study demonstrated that the presence of Ca, Mg and particularly of Al favors shifting of the onset of the structural changes to lower pressures. In line with these observations, studies on $MgSiO_3$ glass that directly probed the atomic environment around the oxygen atoms place the 4- to 6-fold transition between 20 and 50 GPa (Kim et al., 2019; Lee et al., 2008).

So far, only a few studies have investigated also the effect of temperature on this transition. A high pressure and temperature XRD study on basaltic melts up to 60 GPa and 3200 K (Sanloup et al., 2013) revealed that Si in this complex partially depolymerized melt reaches octahedral coordination at ca. 35 GPa. This observation is in agreement with recent results from molecular dynamics (MD) simulations on anorthite $CaAl_2Si_2O_8$ and basaltic liquids that reported strong structural changes around all cations in the pressure up to 20 i.e. 30 GPa and at temperatures of ∼6000 K (Bajgain et al., 2015; Ghosh and Karki, 2018; Spera et al., 2009).

Germanates have been used as analogue materials to silicates for decades due to their related properties, the shift of phase transitions to lower pressures and the possibility for applying further analytical techniques (e.g. X-ray absorption spectroscopy). These studies have complemented insights on silicate glasses and provided valuable additional evidence on the structural properties of amorphous matter at extreme pressure (e.g., Baldini et al., 2010; Hong et al., 2014; Itié et al., 1989; Kono et al., 2016; Spiekermann et al., 2019; Vaccari et al., 2009). A recent study on the structural densification mechanism of a nominally fully polymerized complex glass, $NaAlGe_3O_8$ up to 131 GPa, demonstrated that the presence of Na and Al changes fundamentally the densification mechanism compared to the pure oxide, particularly at pressures beyond the transition to octahedral Ge coordination ($>$ 40 GPa) (Krstulović et al., 2020).

In this work, we aim at extending the knowledge on the properties of silicate melts/ glasses at conditions of the deep Earth, particularly addressing compositions that are chemically more complex and closer to those ubiquitous in the Earth's interior. We report on pressure induced local structural changes of two glass compositions up to maximum 164 GPa that exhibit different degrees of melt polymerization: a modified albite glass ($Na_{0.5}Sr_{0.5}Al_{1.5}Si_2Ge_{0.5}O_8$) and a modified albite-diopside glass ($Na_{0.45}Ca_{0.1}Mg_{0.05}Sr_{0.5}Al_{1.35}Si_{1.95}Ge_{0.5}O_{7.8}$). The albite glass composition is a stuffed tectosilicate-like structure, nominally NBO-free and represents a first step away from pure silica. This composition allows for discriminating differences in the structural densification mechanism between pure silica/germania and more complex polymerized melts. In nature, the formation of albitic melts is however restricted to shallow crustal conditions. In spite of high Na and low Ca content, the albite-diopside glass can be considered representative of a simplified basaltic composition that is partially depolymerized, with a higher content of NBOs. Basaltic melts may be formed at various depths of Earth's mantle and have been previously proposed as potential candidates to explain observed seismic anomalies at the core-mantle boundary (Andrault et al., 2014; Fiquet, 2018; Hirose et al., 1999; Jones et al., 2020; Niu and O'Hara, 2004; Pradhan et al., 2015).

We focused on monitoring the structural changes seen from two elements doped in the glasses, Ge and Sr that are analogues for structural melt components such as network formers and modifiers and that are suitable for *in-situ* high pressure X-ray absorption spectroscopic

studies combined with hard X-rays in high pressure devices (Krstulović et al., 2020; Pohlenz et al., 2018). X-ray absorption spectroscopy, and in particular the extended fine structure X-ray absorption spectroscopy (EXAFS), provides detailed element-specific information of the local and mesoscopic atomic arrangements at extreme pressures. Ge embedded as a monitoring element in an aluminous silicate glass may allow extracting information on the behaviour of major network-forming elements (Si, Al). The behaviour of Sr, in turn can be taken as representative for the network-modifying cations (Ca, Mg) and the family of divalent lithophile trace elements that provide important constraints for petrogenetic processes in magmatic geochemistry.

An important finding of this work is the significant influence of alkali and alkaline earth metals on the structural densification mechanism especially beyond the 4- to 6-fold coordination change of Si. This finding implies that at equivalent pressure chemically complex melts exhibit higher compressibility compared to GeO_2 or SiO_2 due to increased network flexibility coming from alkali and alkaline earth cations. In contrast to previous findings, our results imply that cations in amorphous materials follow similar structural changes as they do in their crystalline analogues. We also find that these structural changes occur at similar pressures in both amorphous and crystalline compounds. This may indicate that the densification process in amorphous materials is not characterized by specific structural mechanisms that could produce ultra-high density.

3.2 Methods

3.2.1 Glass compositions and sample synthesis

Three glasses were synthesized for the experiments, one with modified albite ($Na_{0.5}Sr_{0.5}Al_{1.5}Si_2Ge_{0.5}O_8$), and two with modified albite-diopside nominal composition ($Na_{0.45}Ca_{0.1}Mg_{0.05}Sr_{0.5}Al_{1.35}Si_{1.95}Ge_{0.5}O_{7.8}$). The details on elemental concentrations (in wt%) of the albite-glass (Ab-glass, run 1) and albite-diopside glasses (AbDi-glass run 2, 3) obtained from electron microprobe measurements are listed in Table 3.1. In Table 3.2, chemical formulas of the nominal glass compositions and of the synthesized glasses can be found. The amorphous nature of the produced glasses was checked and confirmed by XRD patterns.

Table 3.1: Chemical composition of the synthesized glasses (Ab-glass, run 1, AbDi-glass (1), run 2, and AbDi-glass (2), run 3) compared to the nominal composition both in wt%. The concentrations were determined by electron microprobe analysis (EMPA).

Measured concentrations in the glasses in wt%								
Sample	Na_2O	GeO_2	SrO	SiO_2	CaO	MgO	Al_2O_3	Sum
Ab-Glass	5.702 (1)	5.163 (5)	18.159 (5)	42.755 (3)	0.023 (1)	0.000	28.388 (2)	100.190 (5)
AbDi-glass(1)	5.183 (1)	8.188 (6)	17.627 (5)	40.909 (3)	2.216 (1)	0.443 (1)	24.812 (2)	99.380 (6)
AbDi-glass(2)	4.420	14.750	16.160	39.320	1.770	1.320	22.290	100.030
Ab nominal	4.90	16.58	16.38	37.98	0.00	0.00	24.17	100
AbDi nominal	4.47	16.82	16.62	37.57	1.80	0.65	22.07	100

Each glass was additionally doped with ca. 5000 ppm Y, which, however, is not considered here. The glasses were synthesized from oxide and carbonate powders of SiO_2, Al_2O_3, MgO, Na_2CO_3, $CaCO_3$, $SrCO_3$, GeO_2 and Y_2O_3. The nominal concentrations of Ge and

Table 3.2: Chemical formula of the starting mixture and of the synthesized glasses for Ab-glass, run 1 and for AbDi-glass (1,2), run 2 and run 3, respectively. Results of the chemical formula for the synthesized glasses are calculated from the mean value of the wt% results that were determined by electron microprobe analysis (EMPA).

Composition	Chemical formula of the start mixture	Chemical formula of the glass
Ab	$Na_{0.5}$ $Sr_{0.5}Al_{1.5}Si_2Ge_{0.5}O_8$	$Na_{0.35}Sr_{0.56}Al_{1.78}Si_{2.28}Ge_{0.16}O_8$
AbDi-glass(1)	$Na_{0.45}Ca_{0.1}Mg_{0.05}Sr_{0.5}Al_{1.35}Si_{1.95}Ge_{0.5}O_{7.8}$	$Na_{0.64}Ca_{0.13}Mg_{0.04}Sr_{0.7}Al_{1.68}Si_{2.35}Ge_{0.27}O_{7.8}$
AbDi-glass(2)	$Na_{0.45}Ca_{0.1}Mg_{0.05}Sr_{0.5}Al_{1.35}Si_{1.95}Ge_{0.5}O_{7.8}$	$Na_{0.39}Ca_{0.07}Mg_{0.09}Sr_{0.44}Al_{1.21}Si_{1.81}Ge_{0.39}O_{7.8}$

Sr were chosen to reach an absorption jump at the K edge of ca. 0.2. Powders were first ground in an agate mortar for about 30 min for homogenization of the mixture. To avoid material loss during grinding, acetone was added to the mixture.

The Ab-glass and the AbDi-glass for the first X-ray absorption experiment (run 1 and 2) were synthesized from the homogenized substances that were first annealed in a Pt crucible for about an hour at 1050 °C to achieve decarbonization followed by a temperature increase to 1600 °C to achieve melting. At 1600 °C the mixture was kept in the furnace for about 2 - 2.5 h and subsequently quenched by placing the Pt crucible into water at room temperature. The produced glass exhibits a considerable Ge loss due to evaporation (see Table 3.1), but the remaining concentration was sufficient to perform the first X-ray absorption experiment in spite of small absorption jump at K edge of ca. 0.1 (run 1). Optical inspection provided by electron microprobe analysis (EMPA) of the run-products revealed a homogeneous and bubble free glass.

For the second X-ray absorption experiment (run 3) a new glass was synthesized using an improved protocol to limit loss of Ge due to evaporation during high temperature homogenization. The oxide and carbonate mixture was first ground, annealed and molten without the GeO_2 fraction. After 1 h of decarbonisation at 1050 °C the mixture was subsequently molten at 1600 °C for 24 h, quenched, ground and molten again at the same temperature for three days and subsequently quenched and ground again. The GeO_2 portion was then added to the mixture, which was then ground again and molten at 1200 °C for 24 h and subsequently at 1600 °C for 20 min. This procedure allowed for synthesis of the homogeneous bubble and crystal free glass exhibiting a limited loss of Ge (Table 3.1).

In terms of the alumina saturation index ASI, which is defined as the molar ratio between Al_2O_3 and $CaO + Na_2O + K_2O$ (Zen, 1986; Zen, 1988), and distinguishes peraluminous ASI > 1, peralkaline ASI < 1, and metaluminous compositions, ASI $= 1$, the synthesized Ab-glass is peraluminous (ASI = 1.2), whereas AbDi-glass is moderately peralkaline (ASI = 0.7).

3.2.2 High pressure XAS experiments

Three EXAFS experiments in transmission mode were carried out on Ge and Sr K edges in the bending magnet beamline BM23 of the European Synchrotron Radiation Facility, ESRF (Mathon et al., 2015). The first experiment (run 1 and 2) aimed to examine in detail the differences in densification mechanism between polymerized and partially depolymerized glasses during the 4- to 6-fold conversion of Si and Ge. In these experiments also the coordination number change of Sr from 6-fold to higher coordinated species upon compression was determined. Therefore, Sr and Ge K edges of the Ab-glass (run 1) and AbDi-glass (run 2) were

probed in fine pressure steps of ∼3 - 5 GPa up to 41 GPa. The second experiment (run 3) aimed to investigate the densification mechanism of the partially depolymerized glass beyond the 6-fold state of Ge (and Si) up to 164 GPa. Such high pressure experiments restrict the sample thickness to few microns and therefore the AbDi-glass with higher Ge content (AbDi-glass (run 3)) was used.

A double crystal fixed-exit monochromator with two Si(111) crystals was employed to monochromatize the X-rays. The beam was focussed to 5×5 µm^2 by two Pt-coated Kirkpatrick-Baez mirrors (KB-mirrors) inclined to 4 mrad. These mirrors served additionally for the rejection of higher order harmonics. During the first experiment (run 1, 2) two Rh-coated mirrors were additionally employed in front of the KB-mirrors to achieve a higher rejection of harmonics, which however resulted in reduced photon fluxes on the sample. Three ionization chambers allowed simultaneous transmission measurement of the sample and the reference material. As a reference of the energy to monochromator angle a Pt-foil was placed between second and third ion chamber. XAFS spectra were collected in the energy range from 11,044 to 11,964 eV (Ge) and from 16,008 to 16,966 eV (Sr) in run 1 and 2 and from 10,974 to 12,079 eV (Ge) in run 3. In terms of k-space the data collected on Ge K edge extend up to 16 Å^{-1}, and on Sr K edge up to 15 Å^{-1}, though shorter range is considered for the EXAFS analysis (see EXAFS analysis section).

For high pressure experiments, membrane driven diamond anvil cells of Le Toullec type (Letoullec et al., 1988) were used. The cells were equipped with nano-polycrystalline diamond anvils (Irifune et al., 2003) that provide glitch free EXAFS spectra (Rosa et al., 2019). The diamond anvils were of Boehler-Almax design (Boehler and De Hantsetters, 2004) with culet diameters of 300 µm for run 1 and 2, and 200 µm for the third run. Rhenium gaskets were employed in all experiments. The initial gasket thickness of 200 µm was pre-indented to a thickness of 65 µm for the runs 1 and 2 and to 30 µm for run 3, respectively. A circular hole was drilled by a laser in the centre of the indentation with the size of 150 µm (run 1 and 2) and 100 µm (run 3), that served as the sample chamber. The chamber was filled entirely with the synthetic glass without pressure transmitting medium. A gaseous pressure medium might infiltrate the cavities of the silicate network structure of the glass and thus likely modify the structural response of the glass to the compression (Shen et al., 2011).

In all experiments a small ruby sphere was placed at the rim of the gasket hole, serving as pressure standard using the ruby-fluorescence method (Mao et al., 1978). The non-hydrostatic ruby pressure scale (Mao et al., 1978) was used to calculate the pressure from the line shift. In run 3 the sample pressures beyond 85 GPa were determined from the lattice volume of the Re-gasket using diffraction measurements conducted at BM23. For these measurements the beam was tuned to an energy of 18 keV corresponding to a wavelength of 0.6888 Å and a MarCCD 165 detector was employed, placed 191.37 mm from the sample. Detector to sample distance, detector tilt and rotation parameters were obtained from a standard measurement of a CeO_2 powder. Diffraction data were acquired without sample oscillation and with an exposure time of two minutes. Diffraction data were taken before and after the acquisition of the EXAFS data and each time at two opposed positions in the Re gasket in order to obtain an estimate of the pressure gradient across the sample. The pressures from the lattice volume of the Re gasket were obtained using the Vinet equation of state (V-EOS) reported by Anzellini et al. (2014). This pressure determination method provides usually about 1.2 % lower pressures than those in the centre of the cell. The pressure variation before and after an EXAFS acquisition did not exceed 2 GPa, while the gradient across the sample at certain pressure points reached up to 4 GPa, which we relate to the presence of non-hydrostatic stresses. Based on these observations we considered a larger pressure uncertainty of up to 7 % for pressure points beyond 85 GPa.

3.2.3 EXAFS analysis

The XAFS spectra were analysed by the software package XAFS (Winterer, 1997). For the background subtraction in the pre-edge region a polynomial function to the signal below the edge was fitted (for Ge K edge from 11,049 to 11,080 eV and for Sr K edge from 15,901 to 16,050 eV). The normalization of the spectra was performed by fitting a Gaussian function and an error function to the edge position (E_0). The normalized spectra were converted from energy into the k-space $\chi(k)$. The background subtraction of the extended absorption signal or post-edge region (EXAFS) was obtained using a smoothing spline function with 8 knots covering the region from 0 to 11 Å^{-1} for both Ge and Sr K edges.

The EXAFS spectra were fitted in k-space using unfiltered data. For analysis Ge spectra were k^3 and Sr spectra were k^2 weighted and Fourier transformed without phase-shift correction using a Kaiser-Bessel envelope. Due to the noise in the spectra at higher k, the signal used for analysis was restricted to k-ranges of 3 to 10 Å^{-1} for Ge and from 3 to 9 Å^{-1} for Sr. The backscattering amplitude and phase shift, as well as photoelectron mean free path were calculated by FEFF9 code (Rehr et al., 2010). The data on Ge K edge in AbDi-glass were fitted using Ge-O model in tetrahedral coordination (quartz structure) up to 25 GPa. Above this pressure, models for the first (Ge-O) and second (Ge-Si) coordination shell in octahedral coordination were used. Due to the low amplitude of the signal of the second shell (due to disorder) and the low amount of Ge in the glass, the contribution by Ge was not sufficient, and Ge could not be reliably fitted.

The Ge K edge data of the Ab-glass were fitted using only a model in tetrahedral coordination for the first Ge-O coordination shell, because the introduction of additional scattering path did not contribute to any changes of the fitted parameters. Sr K edge data were fitted using contributions of the first Sr-O and second Sr-Si coordination shells. For the fit an input structural model based on octahedral Sr coordination was used along the entire pressure range of 41 GPa. For all Ge and Sr fits an asymmetric pair distribution function had to be used to compensate for anharmonic effects as implemented in the XAFS-program (Pohlenz et al., 2018; Winterer, 1997) for the Ge-O and Sr-O, and Ge-Si and Sr-Si pair distributions.

Free fit parameters for Ge K edge were the mean bond distance $R_{\text{Ge-O}}$, the variance in the ligand distances (EXAFS Debye-Waller factor) $\sigma^2_{\text{Ge-O}}$, the coordination number $N_{\text{Ge-O}}$ and the non-structural parameter ΔE_0, the energy mismatch between theoretical and experimental energy scales. In order to reduce the number of fitting parameters, the peak asymmetry h was treated as fixed parameter that was changed manually and incrementally. The first fits were performed using a quasi-Gaussian peak shape approximation followed by fits with increasing asymmetry contributions until the best fit for each spectrum was obtained that was deduced from the χ^2-value. For second shell fits, the bond distance $R_{\text{Ge-Si}}$ and its variance $\sigma^2_{\text{Ge-Si}}$ were set as free parameters, while the coordination number parameter $N_{\text{Ge-Si}}$ and the energy mismatch ΔE_0 were constrained to be equal to the values of the corresponding parameters of the first coordination shell ($N_{\text{Ge-O}}$ and ΔE_0). The non-structural parameter amplitude reduction factor S_0^2 was constrained to 1 for the data collected within the run 1 and 2, which corresponds to the value obtained by fitting the data set at 0 GPa as well as spectra of crystalline GeO_2 in quartz and rutile structure. For EXAFS data acquired in run 3, S_0^2 was set to a value of 0.91, to compensate for the slightly reduced harmonic rejection related to absence of the second pair of Rh-mirrors in this run, following previous systematics (Krstulović et al., 2020).

Free fit parameters for Sr K edge were first and second shell interatomic distance $R_{\text{Sr-O}}$ and $R_{\text{Sr-Si}}$, first and second shell ligand distance variance $\sigma^2_{\text{Sr-O}}$ and $\sigma^2_{\text{Sr-Si}}$, first shell ΔE_0 and second shell asymmetry parameter $h_{\text{Sr-Si}}$. Coordination number fit parameter for both

coordination shells, $N_{\text{Sr-O}}$ and $N_{\text{Sr-Si}}$, was treated as fixed with equal values in the second and first coordination shell. First shell asymmetry parameter $h_{\text{Sr-O}}$ and second shell energy mismatch ΔE_0 were also treated as fixed parameters, whereby energy mismatch was constrained to be equal to the first shell ΔE_0. S_0^2 was constrained to 1.

3.3 Results

3.3.1 Ge coordination and bond distances in Ab- and AbDi-glass

The k^3 weighted EXAFS signal and corresponding Fourier Transform (FT-magnitude) of Ge-O in Ab-glass (run 1) are presented in Fig. 3.1a and b. In the first pressurizing steps to 8 GPa, the EXAFS oscillations sharpen (Fig. 3.1a.). Beyond 8 GPa and until 22 GPa the oscillations broaden and shift to slightly lower k-value. Beyond 22 GPa a clear opposite shift to higher k-values is observed. The main peak of the FT-magnitude of the EXAFS spectra at ∼1.3 Å shows very sharp intensity increase between ∼12 and ∼16 GPa (Fig. 3.1b), while it exhibits more or less constant intensity value at other pressures. A second isolated sharp peak can be identified at ∼2.5 Å and at low pressures of 2 GPa. This peak corresponds to the signal of the second coordination shell. At pressures beyond 2 GPa, a third peak emerges at around 2 Å that increases in its intensity and width up to 41 GPa. All peaks exhibit a slight shift to the higher R-value with increasing pressure.

In Fig. 3.2 the k^3 weighted EXAFS spectra (Fig. 3.2a) with its FT-magnitude (Fig. 3.2b) of Ge-O in AbDi-glass from run 2 and 3 are presented. Similar to Ab-glass, the sharpening and the shift of the EXAFS oscillations to lower k-values, characteristic for low pressure up to 20 GPa (first 3 spectra), is replaced by the broadening of the oscillations and their shifts to higher k-values with increasing pressure beyond 26 GPa.

In the moduli of the Fourier transform of the EXAFS spectra (Fig. 3.2b), the first peak shifts slightly to the larger R-value within first 26 GPa (first five spectra from the bottom). Its position remains rather constant with increasing pressure up to 113 GPa (7th spectrum from the top), where it slightly shifts to the larger R-value and then remains constant along the whole remaining measured pressure range. The amplitude of the main peak at ∼1.3 Å does not change much within the first 32 GPa. At 37 and at 70 GPa the amplitude increases considerably (7th and 10th spectrum from the bottom), at ∼90 GPa, as well as at ∼135 GPa (9th and 4th spectrum from the top) the amplitude increases again. The signal beyond the first coordination shell is rather weak, but increases with pressure, especially above 25 GPa.

In Fig. 3.3 the extended k^3 weighted spectra of the Ge K edge EXAFS data of Ab- (Fig. 3.3a) and AbDi-glass (Fig. 3.3b) are shown together with their corresponding fits as a function of increasing pressure. Overall, the data on AbDi-glass exhibit higher quality and fit better to the model compared to the Ab-glass. The high noise of the Ab-glass Ge K edge EXAFS data hindered the inclusion of the second shell into the fit and a discrimination between fit qualities using either a tetrahedral or octahedral structural input model.

The first coordination shell bond distance ($R_{\text{Ge-O}}$) of Ab- and AbDi-glass extracted from the EXAFS fits is shown in Fig. 3.4. It increases steeply in both glasses within the first ∼32 GPa ($\Delta R \sim 0.1$ Å). Beyond this pressure it exhibits a continuous decrease up to the highest probed pressure of 164 GPa. Interestingly, $R_{\text{Ge-O}}$ obtained at the highest probed pressure of 164 GPa corresponds closely to the values extracted at the lowest probed pressure of ∼5 GPa for the AbDi-glass.

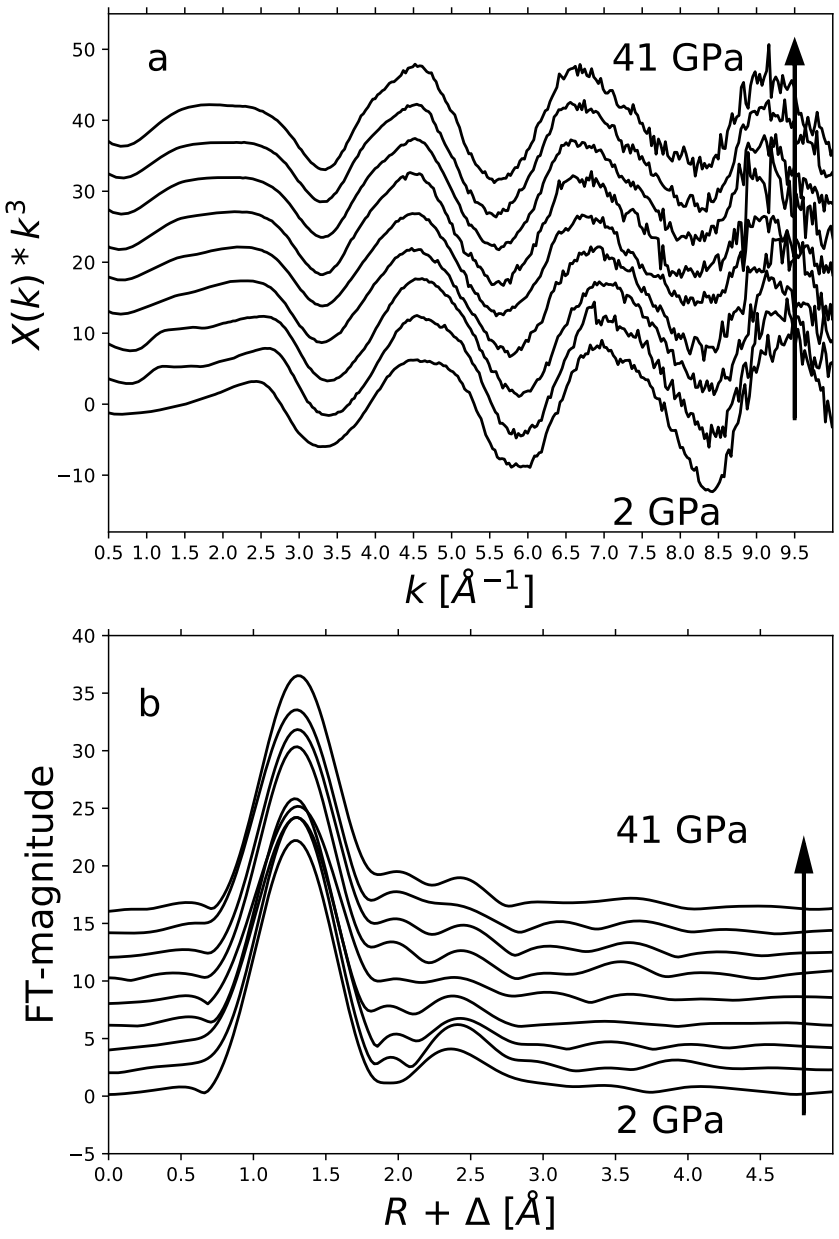

Figure 3.1: a Evolution of k^3 weighted EXAFS function ($k^3\,\chi(k)$) at the Ge K edge of Ab-glass (run 1) upon compression to 41 GPa. b Magnitude of the Fourier transforms (R) of the EXAFS functions ($k^3\,\chi\,(k)$) of Ab-glass (run 1) (shown in Fig. 3.1a) to 41 GPa. In contrast to fitted $R_{\text{Ge-O}}$ values (Table 3.3), magnitudes of the Fourier Transforms plotted here are not corrected for the phase-shift.

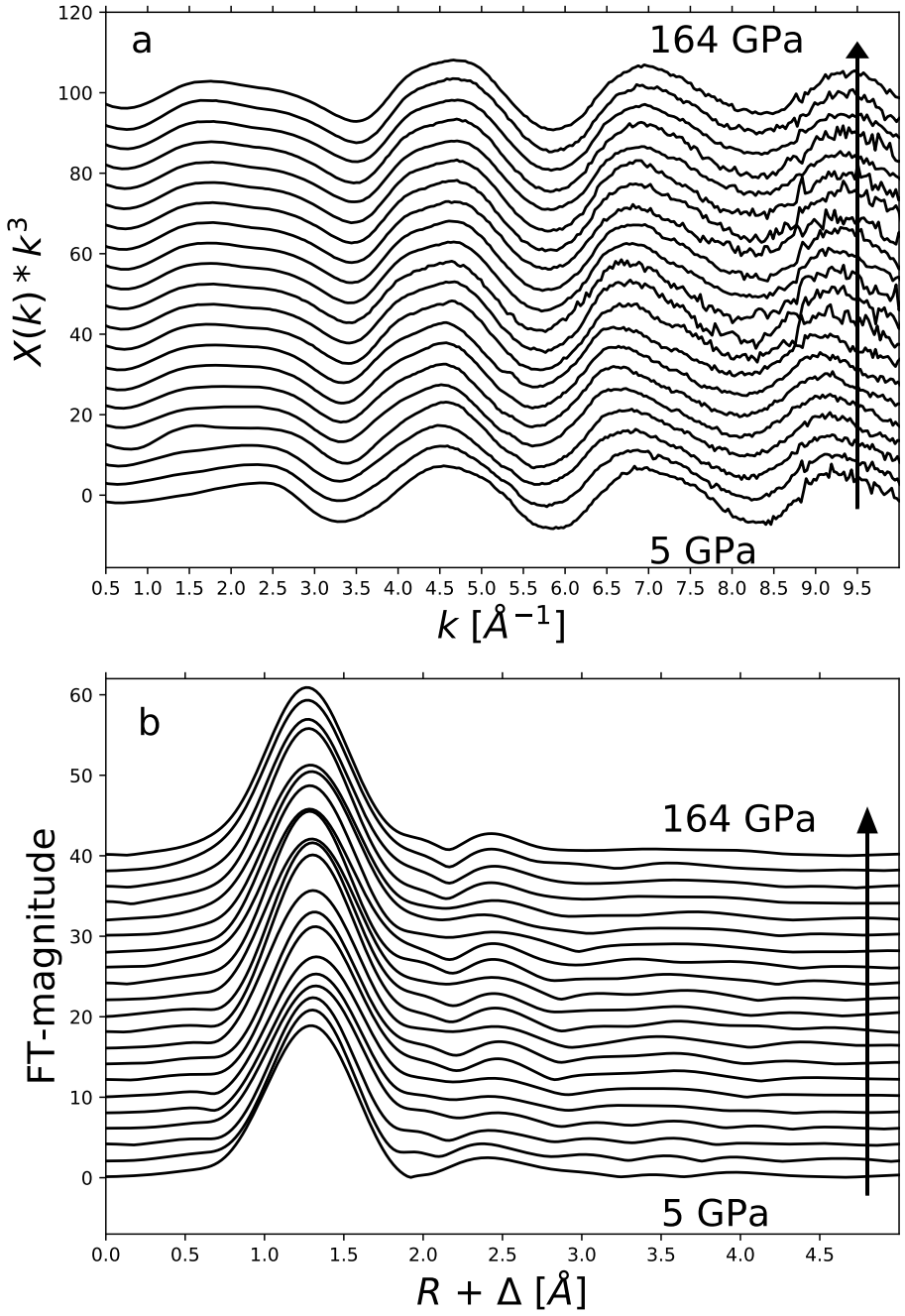

Figure 3.2: a Evolution of k^3 weighted EXAFS function (k^3 χ (k)) at the Ge K edge of AbDi-glass (run 2 and 3) upon compression to 164 GPa. b Magnitude of the Fourier transforms (R) of the EXAFS functions (k^3 χ (k)) of AbDi-glass (run 2 and 3) (shown in Fig. 3.2a) to 164 GPa. In contrast to fitted $R_{\text{Ge-O}}$ values (Table 3.4), magnitudes of the Fourier Transforms plotted here are not corrected for the phase-shift.

Table 3.3: Fit results on Ge K edge in Ab-glass upon compression to 41 GPa. Free parameters are $R_{\text{Ge-O}}$, $N_{\text{Ge-O}}$, (up to 8 GPa and for the highest pressure point), $\sigma^2_{\text{Ge-O}}$ and ΔE_0. Asymmetry parameter $h_{\text{Ge-O}}$ is usually set to a fixed value. χ^2 indicates the fit quality. The standard deviation for free fit parameters is given in parentheses and refers to the last printed digit.

Run1						
P [GPa]	$R_{\text{Ge-O}}$	$N_{\text{Ge-O}}$	$\sigma^2_{\text{Ge-O}}$	$h_{\text{Ge-O}}$	ΔE_0	χ^2
2 (1)	1.730 (5)	4.2 (5)	0.0008 (5)	0.001 (2)	7.3	1.49
5.1 (1)	1.730 (5)	4.2 (5)	0.0005 (5)	0.02	6.5 (4)	1.49
8.3 (1)	1.735 (5)	4.4 (5)	0.0019 (5)	0.02	6.8 (4)	1.28
11.8 (1)	1.765 (5)	5	0.0002 (5)	0.05	5.6 (4)	1.36
16.4 (1)	1.790 (5)	4.8	0.0005	0.05 (2)	6.4 (4)	1.26
22.5 (2)	1.801 (5)	6	0.00008 (5)	0.062	5.9 (4)	1.92
27.8 (2)	1.815 (5)	6	0.00002 (5)	0.065	6.6 (4)	1.55
40.7 (3)	1.81 (5)	5.6 (5)	0.0007 (5)	0.06 (2)	6.8 (4)	1.88

The fitted first shell coordination number parameter $N_{\text{Ge-O}}$ in Ab- and AbDi-glass is presented in Fig. 3.5. A continuous increase from $N_{\text{Ge-O}}$ from 4 to 6 up to ∼20 - 35 GPa is followed by a stagnation of this value at around ∼6 up to 164 GPa. The fitted values of $N_{\text{Ge-O}}$ have high uncertainties (± 0.5) which are intrinsically related to EXAFS analysis with multiple fit parameters. Therefore, we consider that slight changes in the pressure trend have to be taken with caution and should not be explicitly considered as indicator for changes in the structure.

The values of the extracted best fit asymmetry parameter h for the Ge-O bond are listed in Table 3.3 for Ab-glass (run 1) and in Table 3.4 for AbDi-glass (run 2, run 3). In Ab-glass the Ge-O bond distance shows an asymmetric contribution above 8 GPa with slightly increasing values to 41 GPa ($h_{\text{Ge-O}}$ values between 0.05 and 0.06). In AbDi-glass (run 2) we observed a similar contribution with corresponding values in this pressure domain. Interestingly, values obtained for AbDi-glass (run 3) above ∼61 GPa show a decreasing bond asymmetry reaching the value of 0.005 at the highest probed pressure of 164 GPa.

3.3.2 Sr coordination and bond distances in Ab- and AbDi-glass

The Sr K edge EXAFS spectra of Ab-glass do not considerably change as the pressure increases (Fig. 3.6a). At higher k-range (above 7.5 Å^{-1}) the amplitude is strongly attenuated. Between 7 and 7.5 Å^{-1}, enhancement of amplitude with increasing pressure is observed. The steep increase at 6.5 Å^{-1} develops into an edge-like feature at pressures above 8 GPa. This feature is likely related to a multi-electronic excitation as reported by D'Angelo et al. (1996).

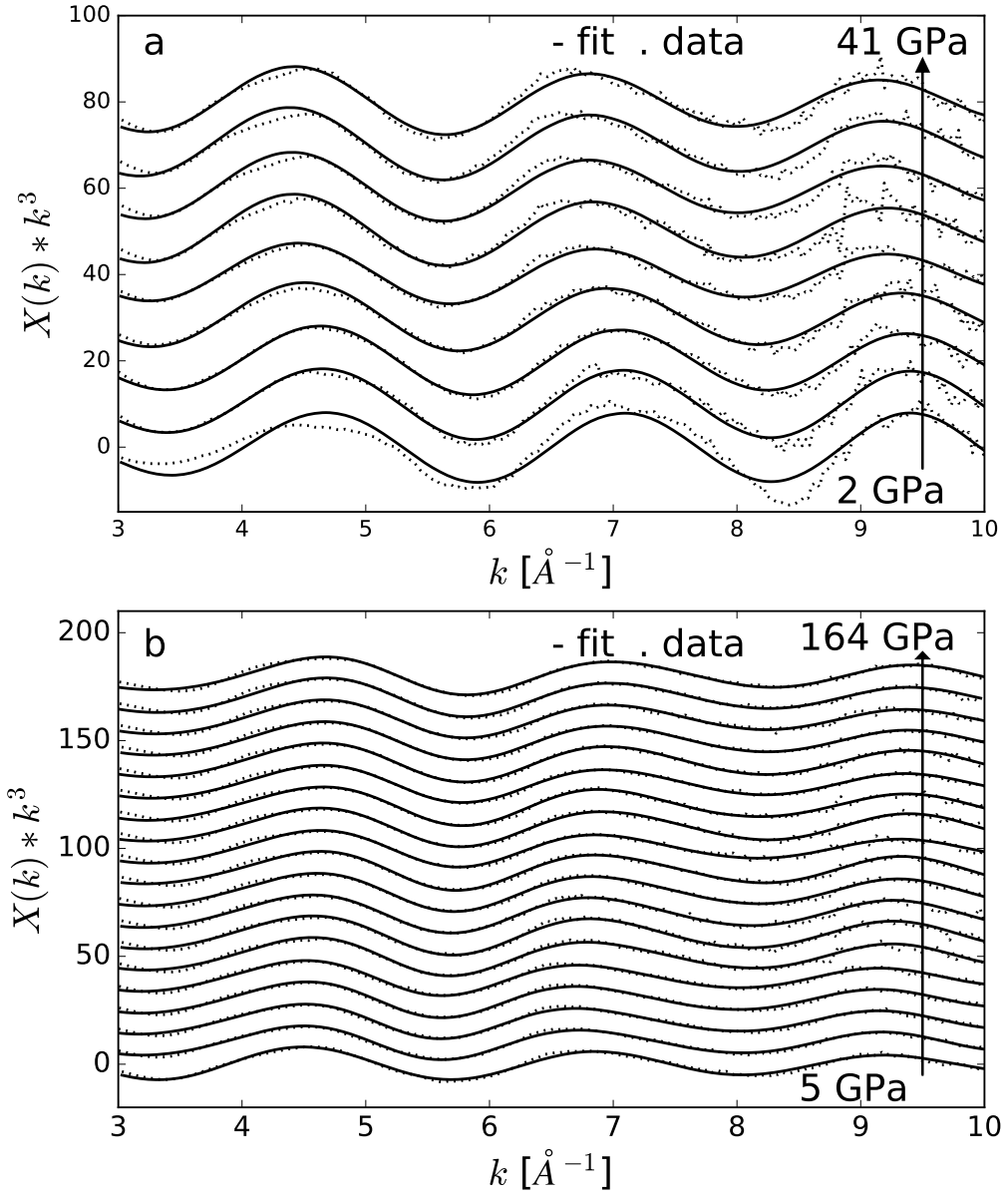

Figure 3.3: k^3 weighted EXAFS functions ($k^3\ \chi\ (k)$) at the Ge K edge of Ab- (Fig. 3.3a) and AbDi-glass (Fig. 3.3b) and corresponding fits as a function of pressure, shown as dashed and solid lines, respectively.

Table 3.4: Fit results on Ge K edge in AbDi-glass (run 2, run 3) upon compression to 164 GPa. Up to 21 GPa only one coordination shell (Ge-O) is used to fit the data. Here free parameters are $R_{\text{Ge-O}}$, $N_{\text{Ge-O}}$, $\sigma^2_{\text{Ge-O}}$ and first shell ΔE_0. Asymmetry parameter $h_{\text{Ge-O}}$ is usually set to a fixed value. Above 26 GPa two coordination shells contribute to the fit. Free parameters are $R_{\text{Ge-O}}$, $R_{\text{Ge-Si}}$, $N_{\text{Ge-O}}$, $\sigma^2_{\text{Ge-O}}$, $\sigma^2_{\text{Ge-Si}}$ and first shell ΔE_0. Asymmetry parameter $h_{\text{Ge-O}}$ and $h_{\text{Ge-Si}}$, as well as second shell ΔE_0 and $N_{\text{Ge-Si}}$ were set to be fixed parameters, whereby second shell ΔE_0 and $N_{\text{Ge-Si}}$ were constrained to be equal to first shell ΔE_0 and to $N_{\text{Ge-O}}$. χ^2 indicates the fit quality. The standard deviation for free fit parameters is given in parentheses and refers to the last printed digit.

Run2						
P [GPa]	$R_{\text{Ge-O}}$	$N_{\text{Ge-O}}$	$\sigma^2_{\text{Ge-O}}$	$h_{\text{Ge-O}}$	ΔE_0	χ^2
5.5 (1)	1.731 (5)	4.4 (5)	0.0033 (5)	0.0 (2)	5.5 (4)	0.94
10.4 (1)	1.775 (5)	4.6 (5)	0.0004 (5)	0.05	7.0 (4)	0.75
15.8 (1)	1.798 (5)	5.2 (5)	0.0002 (5)	0.06	7.1 (4)	0.69
21.4 (2)	1.808 (5)	5.9	0.0016 (5)	0.06	8.5 (4)	0.89
P [GPa]	$R_{\text{Ge-O}}$ $R_{\text{Ge-Si}}$	$N_{\text{Ge-O}}$ $N_{\text{Ge-Si}}$	$\sigma^2_{\text{Ge-O}}$ $\sigma^2_{\text{Ge-Si}}$	$h_{\text{Ge-O}}$ $h_{\text{Ge-Si}}$	ΔE_0	χ_2
26.4 (2)	1.822 (5) 3.09 (5)	5.7 (5)	0.0004 (5) 0.0006 (5)	0.065 0.22	7.5 (4)	0.76
32.2 (2)	1.836 (5) 3.02 (5)	6.2 (5)	0.0004 (5) 0.004 (5)	0.07 0.19	8.1 (4)	0.86
37 (2)	1.829 (5) 3.01 (5)	6.4 (5)	0.0001 (5) 0.004 (5)	0.065 0.19	8.3 (4)	0.87
41.5 (3)	1.826 (5) 3.04 (5)	6.3 (5)	0.0014 (5) 0.004 (5)	0.065 0.2	8.0 (4)	0.97
Run3						
P [GPa]	$R_{\text{Ge-O}}$ $R_{\text{Ge-Si}}$	$N_{\text{Ge-O}}$ $N_{\text{Ge-Si}}$	$\sigma^2_{\text{Ge-O}}$ $\sigma^2_{\text{Ge-Si}}$	$h_{\text{Ge-O}}$ $h_{\text{Ge-Si}}$	ΔE_0	χ^2
61.6 (3)	1.801 (5) 3.0 (7)	6.5 (5)	0.0005 (5) 0.0004 (5)	0.06 0.2	7.5 (4)	1.22
71.5 (3)	1.792 (5) 3.0 (7)	6.3 (5)	0.00001 (5) 0.002 (5)	0.055 0.2	7.1 (4)	1.24
79.4 (3)	1.792 (5) 2.9 (8)	6.0 (5)	0.000002 (5) 0.0005 (5)	0.055 0.19	7.2 (4)	1.25
87.6 (3)	1.786 (5) 2.9 (6)	6.2 (5)	0.0002 (5) 0.0007 (5)	0.055 0.18	7.3 (4)	1.05
92.7 (6)	1.773 (5) 2.9 (6)	5.7 (5)	0.0002 (5) 0.0003 (5)	0.05 0.17	6.9 (4)	1.15
103.9 (7)	1.770 (5) 2.9 (8)	6.2 (5)	0.0032 (5) 0.001 (5)	0.045 0.19	7.4 (4)	1.11
113.6 (7)	1.762 (5) 2.9 (7)	5.7 (5)	0.0003 (5) 0.0004 (5)	0.05 0.19	6.3 (4)	0.94
130.1 (7)	1.754 (5) 2.9 (6)	5.9 (5)	0.0028 (5) 0.004 (5)	0.04 0.18	6.8 (4)	1.09
135 (8)	1.741 (5) 2.9 (7)	5.6 (5)	0.0027 (5) 0.0003 (5)	0.03 0.2	6.1 (4)	1.1
145.2 (10)	1.735 (5) 2.9 (6)	5.6 (5)	0.0043 (5) 0.0006 (5)	0.02 0.2	6.0 (4)	0.91
153.6 (10)	1.732 (5) 2.9 (7)	5.8 (5)	0.0054 (5) 0.0008 (5)	0.005 0.2	6.2 (4)	1.11
163.4 (11)	1.726 (5) 2.9 (6)	5.4 (5)	0.0047 (5) 0.0009 (5)	0.005 0.19	5.4 (4)	0.95

The main peak of the Fourier Transform of Sr-O in Ab-glass has an unusually low magnitude at low pressure, which slightly amplifies as the pressure increases (Fig. 3.6b). The position is relatively constant. It persists as a double peak up to the pressure of 25 GPa (6th peak from the bottom), where the double peak vanishes. The signal coming from the second and third shell does not recognizably shift in R, but it slightly broadens with increasing pressure. (Fig. 3.6b).

The k^3-weighted EXAFS function $k^3\ \chi\ (k)$ and the corresponding Fourier transform of Sr-O in AbDi-glass is shown in Fig. 3.7a and b respectively. Similar to the spectra in Fig. 3.6a, there are no strong spectral variations of the EXAFS function under compression. Beyond 7 $Å^{-1}$ the signal abruptly attenuates (Fig. 3.7a).

The main peak (1.8 Å) of the FT-magnitude of the EXAFS signal of the first (Sr-O) coordination shell in AbDi-glass slightly shifts to the lower R-value beyond ∼8 GPa (Fig. 3.7b). As the pressure increases the signal from the second and third shell (∼2.7 and ∼3.5 Å) broadens.

The k^2 weighted EXAFS spectra of Sr-O with corresponding fits in Ab- and AbDi-glass covering the fitted k-range can be found in Fig. 3.8. In both glasses (Ab-glass, Fig. 3.8a, and AbDi-glass, Fig. 3.8b) the model and the data fit fairly well. At ∼3.6, 6.3 and 8.5 $Å^{-1}$ the mismatches between the experimental data and the fit are due to the multielectronic resonances as already reported by D'Angelo et al. (1996). At pressures below 20 GPa there is a slight mismatch between experimental data and the model also at about 4.5 $Å^{-1}$.

In both Ab-glass and AbDi-glass the Sr-O bond distance in the first coordination shell ($R_{\text{Sr-O}}$) increases with pressure up to 23 and 26 GPa, respectively (Fig. 3.9). Beyond this pressure a continuous decrease of $R_{\text{Sr-O}}$ is observed up to the highest probed pressure of 41 GPa. The overall bond distance increase between the lowest and the maximum measured pressure is very small with $\Delta R \sim 0.027$ Å between 2 and 23 GPa in Ab-glass and 0.024 Å between 5 and 26 GPa in AbDi-glass (see also Table 3.5 and Table 3.6). Interestingly, we found that the asymmetry parameter h has a high contribution on Sr K edge EXAFS signal in both glasses along the entire pressure range of 41 GPa ranging from 0.05 to ∼0.15 (Tables 3.5 and 3.6), indicating a highly disordered coordination environment around Sr.

3.4 Discussion

In this study, we aimed at constraining the compression mechanism of archetypical silicate glasses at the mesoscale beyond Mbar pressures. To achieve this, we probed the local atomic environment of monitoring elements Ge and Sr in the glasses that are accessible using *in-situ* high pressure XAS methods and that can be used as structural analogue elements for major glass forming components such as Si and Ca. We have synthesized glasses based on the albitic composition (run 1) and the albite-diopside eutectic binary composition (run 2, run 3) in which 0.5 formula units of Si were substituted by Ge and 0.5 formula units of Na were substituted by Sr coupled with partial substitution of Si by Al (Tables 3.1, 3.2). Two synthesis protocols have been used to limit loss of Ge during the synthesis of the albite-diopside glasses (run 2, run 3), which also allowed to inspect if there is a dependence of the observed structural changes on Ge concentration. It should be noted that substituting Na by Sr and Si by Al shifts the albitic composition considerably into the binary albite – strontian system, where strontian is the Sr analogue of anorthite feldspar ($SrAl_2Si_2O_8$).

In the following we will first elaborate to what extent the results on the compression

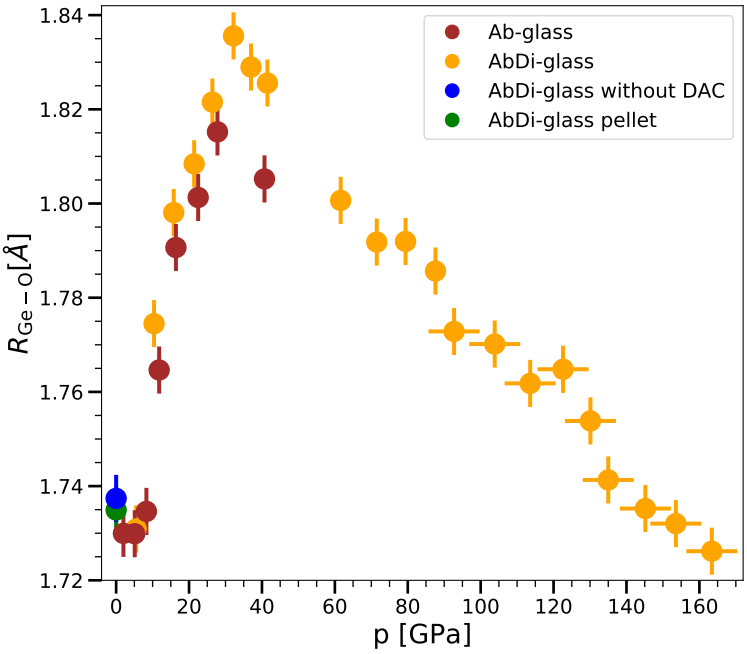

Figure 3.4: Evolution of the average Ge-O bond distances of the first coordination shell ($R_{\text{Ge-O}}$) of Ab- (brown) and AbDi-glass (orange) with pressure, obtained from fitting the experimental EXAFS spectra to a structural model. Additionally, blue circle represents $R_{\text{Ge-O}}$ value obtained for AbDi-glass at ambient pressure without DAC and green circle represents $R_{\text{Ge-O}}$ value obtained for AbDi-glass pressed to a pellet. At pressures below ∼90 GPa uncertainties on pressure are within the symbol size.

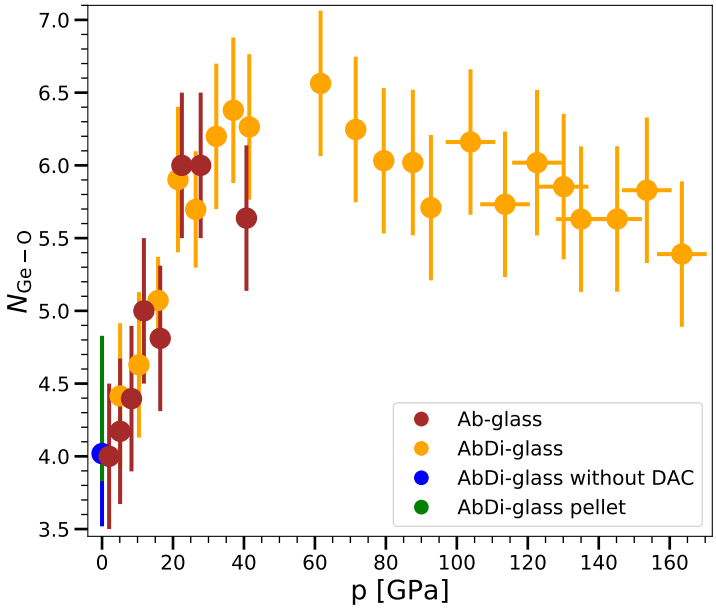

Figure 3.5: Evolution of the fitted number of neighbours in the first coordination shell ($N_{\text{Ge-O}}$) of Ab- and AbDi-glass with pressure. Symbols as in Fig. 3.4.

behaviour of Ge, present as a partial substituent for Si in the doped glasses, is representative for the behaviour of Si in the glasses. Further, we will discuss the role of network modifying cations in the structural densification mechanism based on the results of Sr. Divalent cations such as Ca^{2+} or Mg^{2+} are ubiquitous in natural melts, particularly in those formed by partial melting of the mantle. Many discussions on the properties of silicate melts at extreme pressure are based on insights gained on the simplest chemical systems GeO_2 and SiO_2, which both show a fully polymerized tecto-silicate-like structure at ambient conditions. Thus, the present compositions were chosen in such a way to bridge the knowledge between the simple extraordinary fully polymerized compositions, which are irrelevant for magmas in the lower mantle, and those compositions that are more relevant for mantle-related processes. This systematic strategy allows for assessing the role of composition on the densification mechanism of magmas.

3.4.1 Structural changes of Ge in aluminosilicate glasses upon compression

In both Ab- and AbDi-glass the Ge-O bond distance ($R_{\text{Ge-O}}$) follows very similar pressure trends, showing first a continuous increase up to ∼32 GPa, followed by a continuous decrease up to the highest probed pressure (Fig. 3.4). We interpret the increase of $R_{\text{Ge-O}}$ in terms of Ge coordination increase and a concomitant change of the next-nearest neighbour connectivity from corner-shared tetrahedra to edge-shared octahedra, in agreement with previous observations on germanate glasses (Durben and Wolf, 1991; Hong et al., 2014; Itié et al., 1989; Krstulović et al., 2020). The structural changes around Ge are accompanied by structural changes around oxygen atoms driven by charge balance requirements. In this pressure domain, the glass structure forms an oxygen-closest-packing-like arrangement and the O coordination number changes from 2 to 3 (Krstulović et al., 2020; O'Keeffe and Hyde, 1981).

The subsequent contraction of $R_{\text{Ge-O}}$ persists over the entire remaining pressure range and follows a similar pressure evolution in the two glasses compared to the one of pure Ge-albite glass, $NaAlGe_3O_8$ (Krstulović et al., 2020), as illustrated in Fig. 3.10. It is noticeable that the bond lengths of the Ab-glass are overall shorter than those of AbDi-glass and $NaAlGe_3O_8$-glass. However, this difference is close to the resolution limit of EXAFS analysis, particularly considering the lower quality of the Ab-glass spectra due to the lower Ge content in the Ab-glass (5 wt%) than in AbDi-glass (8 and 15 wt%, run 2, run 3), and in $NaAlGe_3O_8$. Thus, the lower quality of the EXAFS spectra of Ab-glass might be responsible for the shorter Ge-O bond distances in Ab-glass compared to those extracted for AbDi-glass and $NaAlGe_3O_8$. In contrast to Ab-glass, Ge-O bond distances extracted for the two AbDi-glasses (run 2, run 3) gave almost identical results independent of their difference in the Ge content and are similar to the Ge-O bond distances in $NaAlGe_3O_8$ glass (Fig. 3.10).

The onset of $R_{\text{Ge-O}}$ increase in Ab- and AbDi-glass seems to be shifted to slightly higher pressure compared to $NaAlGe_3O_8$. However, due to low data coverage in this pressure range, this cannot be asserted with certainty. These small differences might suggest that even though the Ge content in these silicate glasses is considerably lower than that of Si, its structural evolution differs only slightly from that of the pure germanate glass. In binary GeO_2-SiO_2 glasses the onset of the coordination change for Ge is shifted to higher pressure compared to glassy GeO_2, and the transition range extended over a larger pressure interval with increasing Si content (Majérus et al., 2004). Those observations suggest that in germanate-silicate mixtures, the local structure around Ge would move towards that of Si. The absence of such an effect in the chemically more complex glass compositions studied here might suggest that in more complex systems the structural behaviour of network-forming elements is governed

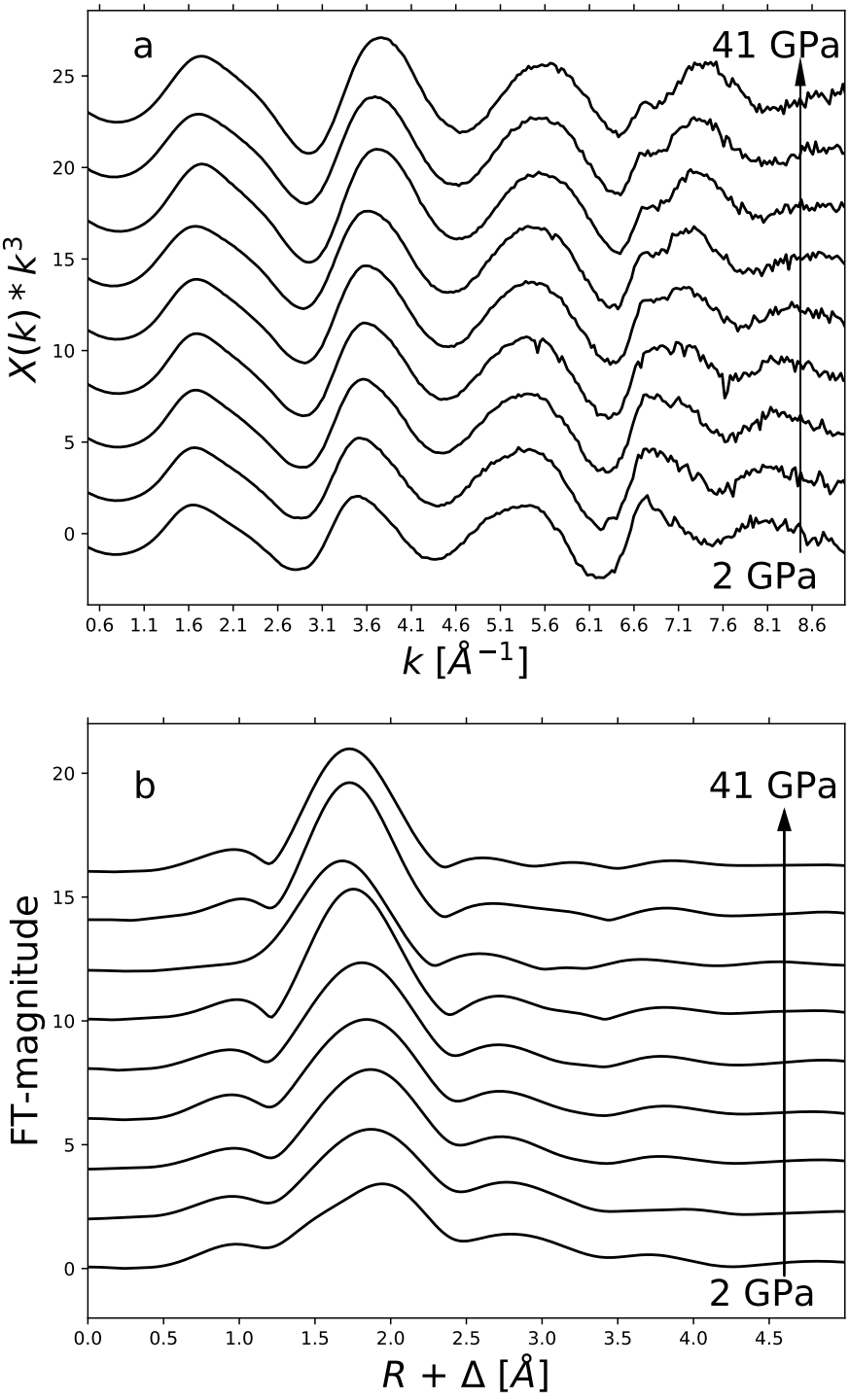

Figure 3.6: a Evolution of k^3 weighted EXAFS functions (k^3 χ (k)) at the Sr K edge of Ab-glass upon compression to 41 GPa. b Magnitude of the Fourier transforms (R) of the EXAFS functions (k^3 χ (k)) of Ab-glass (shown in Fig. 3.6a) to 41 GPa. In contrast to fitted $R_{\text{Sr-O}}$ values (Table 3.5), magnitudes of the Fourier Transforms plotted here are not corrected for the phase-shift.

by the presence of the network modifying cations like Na, Ca, Mg or Sr (see also below), and Al. This conclusion is in agreement with previous vibrational spectroscopic observations in quenched glasses of SiO_2 , $CaAl_2Si_2O_8$ and $CaMgSi_2O_6$, that revealed a strong dependence of the onset pressure to higher coordinated Si on the bulk composition (Williams and Jeanloz, 1988).

Table 3.5: Fit results on Sr K edge in Ab-glass upon compression to 41 GPa. Free parameters are $R_{\text{Sr-O}}$, $R_{\text{Sr-Si}}$, $\sigma^2_{\text{Sr-O}}$, $\sigma^2_{\text{Sr-Si}}$, $h_{\text{Sr-Si}}$ and the first shell ΔE_0. $N_{\text{Sr-O}}$ and $N_{\text{Sr-Si}}$ are treated as fixed parameters and linearly correlated. Second shell ΔE_0 was set to be fixed parameter with equal values to the first shell ΔE_0. Asymmetry parameter $h_{\text{Sr-O}}$ is usually set to a fixed value. χ^2 indicates the fit quality. The standard deviation for free fit parameters is given in parentheses and refers to the last printed digit.

P [GPa]	$R_{\text{Sr-O}}$ $R_{\text{Sr-Si}}$	$N_{\text{Sr-O}}$ $N_{\text{Sr-Si}}$	$\sigma^2_{\text{Sr-O}}$ $\sigma^2_{\text{Sr-Si}}$	$h_{\text{Sr-O}}$ $h_{\text{Sr-Si}}$	ΔE_0	χ^2
2.0 (1)	2.581 (7) 3.49 (10)	6	0.015 (1) 0.004 (5)	0.055 0.15	4.5 (4)	0.09
5.1 (1)	2.584 (7) 3.53 (10)	6.2	0.012 (1) 0.001 (5)	0.07 0.176 (1)	4.8 (4)	0.08
8.3 (1)	2.591 (7) 3.53 (10)	6.3	0.007 (9) 0.002 (4)	0.085 0.182 (1)	5.1 (4)	0.08
11.8 (1)	2.592 (7) 3.52 (10)	6.5	0.006 (9) 0.004 (4)	0.0995 0.187 (1)	5.2 (4)	0.08
16.4 (1)	2.599 (7) 3.49 (10)	7	0.004 (8) 0.009 (4)	0.11 0.184 (1)	5.1 (4)	0.07
22.5 (2)	2.608 (7) 3.470 (10)	7.4	0.002 (8) 0.01 (4)	0.125 0.185 (1)	4.6 (4)	0.07
27.8 (2)	2.602 (7) 3.5 (10)	8	0.0009 (8) 0.02 (4)	0.135 0.180 (1)	5.5 (4)	0.074
32 (2)	2.599 (7) 3.36 (10)	8	0.001 (7) 0.03 (4)	0.136 0.166 (1)	4.6 (4)	0.06
40.7 (3)	2.598 (7) 3.3 (10)	8.7	0.001 (7) 0.04 (4)	0.144 0.1 (4)	4.9 (4)	0.06

The observed strong compositional effect on densification is best understood through the structural role of oxygen. The increase of coordination of the network-forming cations Ge or Si is accompanied by an increase of the oxygen coordination number. Both changes are crucial for complying with constraints for the bond valence sum of oxygen. O'Keeffe and Hyde (1981) have introduced the concept of non-bonded forces for explaining structural properties of compounds that particularly do not comply with structural principles derived from ionic crystals, i.e. the ratio of ionic radii of cation and anion. An important structural parameter for defining the overall structure and atomic coordination numbers was found to be the ratio

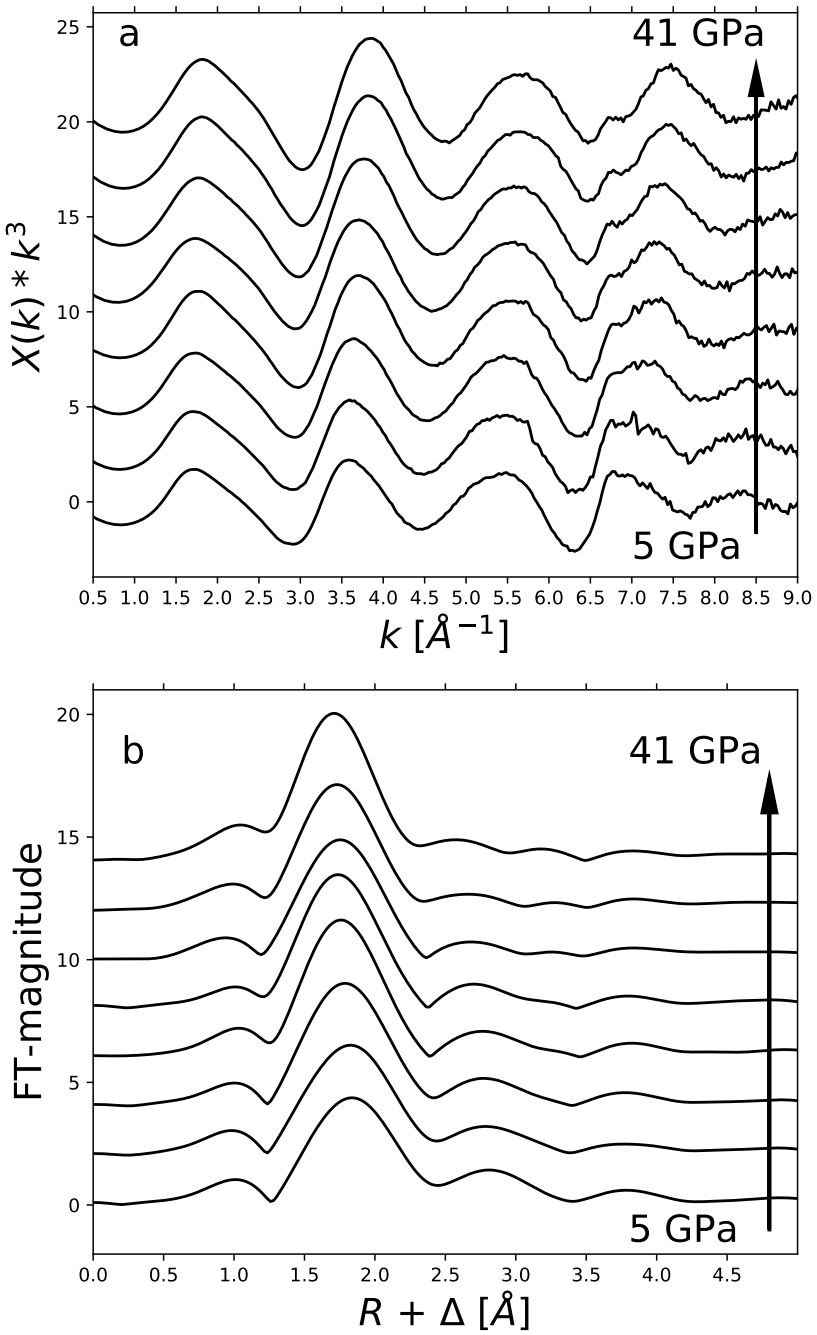

Figure 3.7: a Evolution of k^3 weighted EXAFS functions (k^3 χ (k)) at the Sr K edge of AbDi-glass upon compression to 41 GPa. b Magnitude of the Fourier transforms (R) of the EXAFS functions (k^3 χ (k)) of Sr K edge of AbDi-glass (shown in Fig. 3.7a) to 41 GPa. In contrast to fitted $R_{\text{Sr-O}}$ values (Table 3.6), magnitudes of the Fourier Transforms plotted here are not corrected for the phase-shift.

between the non-bonded cation radius R and the cation anion bond length l (O'Keeffe and Hyde, 1981). In this concept, structural changes are controlled by cation-cation repulsive forces. This concept relies on the observation that compression induces large reductions of anion-anion distances while rather small distance reductions between cations are observed. The parameter R can be considered constant for a given cation and the minimum distance between two non-bonded cations is defined by the sum of their R values. Likewise, the ratio R/l is a cation-specific parameter and indicative for a certain anion coordination number. For example, the ideal R/l ratio is 1.00 for 2 cations coordinating a central anion and is 0.866 for 3 coordinating cations. These anion coordination numbers correspond to 4-fold coordinated cations with corner sharing and 6-fold coordinated cations with edge sharing, respectively. Compression leads to significant variations in l and thus in the R/l ratio and triggers distinct structural changes in a given compound. Chemical pressure, e.g. elemental substitution, would have a similar effect. Larger cations with equivalent or lower charge in comparison to Si^{4+} such as Ge^{4+} , Na^{+} , Mg^{2+} and Ca^{2+} exhibit lower R/l ratios (i.e., R/l for Si = 0.93, Ge = 0.89, Mg = 0.85) due to extended cation-anion bond. Therefore, the critical R/l values, necessary for coordination changes in the anion (cation) are reached at lower pressures in presence of these cations. These considerations provide a simple explanation for the absence of the effect of Si on the structural changes of Ge in the glasses studied here, in contrast to binary GeO_2-SiO_2 glasses (Majérus et al., 2004).

In the pressure range above 32 GPa, the Ge-O distances in AbDi-glass are slightly larger than those in glassy $NaAlGe_3O_8$, however the gradient of the pressure trend is the same in both glasses. Krstulović et al. (2020) have assigned the compressional behaviour of Ge in glassy $NaAlGe_3O_8$ to mere compression of undistorted octahedra due to the similarity of the slope to that of octahedral Ge in rutile-structured GeO_2, extrapolated to higher pressure (see also Spiekermann et al., 2019). Thus, the slope observed for the AbDi-glass suggests similar compressional behaviour of the Ge octahedron in this glass, i.e. mere compression of an undistorted octahedron.

Our observations in chemically complex glasses are in contrast to the reported cation polyhedra compressibilities in amorphous GeO_2 and SiO_2. To compare these different systems, we calculated the reduced cation-anion bond distances (R_{HP}/R_0) from the reported high pressure values (R_{HP}) and their ambient condition values (R_0) as presented in Fig. 3.11). At pressures above the completion of the octahedral coordination, SiO_2 and GeO_2 exhibit roughly similar pressure trends as measured by XRD and valence-to-core XES (Kono et al., 2016; Prescher et al., 2017; Sato and Funamori, 2010; Spiekermann et al., 2019), which strongly diverges from the pressure trend of all shown more complex glasses. EXAFS data on GeO_2 (Hong et al., 2014) do also diverge above ca. 40 GPa, but the available data are limited to 65 GPa. Krstulović et al. (2020) and Spiekermann et al. (2019) have argued based on bond distance – coordination number systematics and bond valence considerations that the evolution of the Ge-O or Si-O distance in GeO_2 and SiO_2 is best explained by octahedral distortion during compression. This would imply that the coordination number determined in those XRD-studies is inconsistent with the Ge/Si-O distance determined at the same time, and this might be related to uncertainties due to limited resolution of this technique and overlap of coordination shells.

As already discussed for the onset of the conversion from tetrahedral to octahedral Ge/Si, the critical threshold values for R/l, as the crucial parameter for changes in coordination or structure, are overstepped at higher pressures for the simple oxide systems. Cold compression leads to polyhedral distortions as the required input energy for bond breaking and therefore increasing densification is not provided, conversion is not provided neither (e.g. Dutta et al., 2018). In the more complex systems, the presence of large cations and NBOs may accommodate larger parts of the densification, inhibiting polyhedral distortion. Further, for the

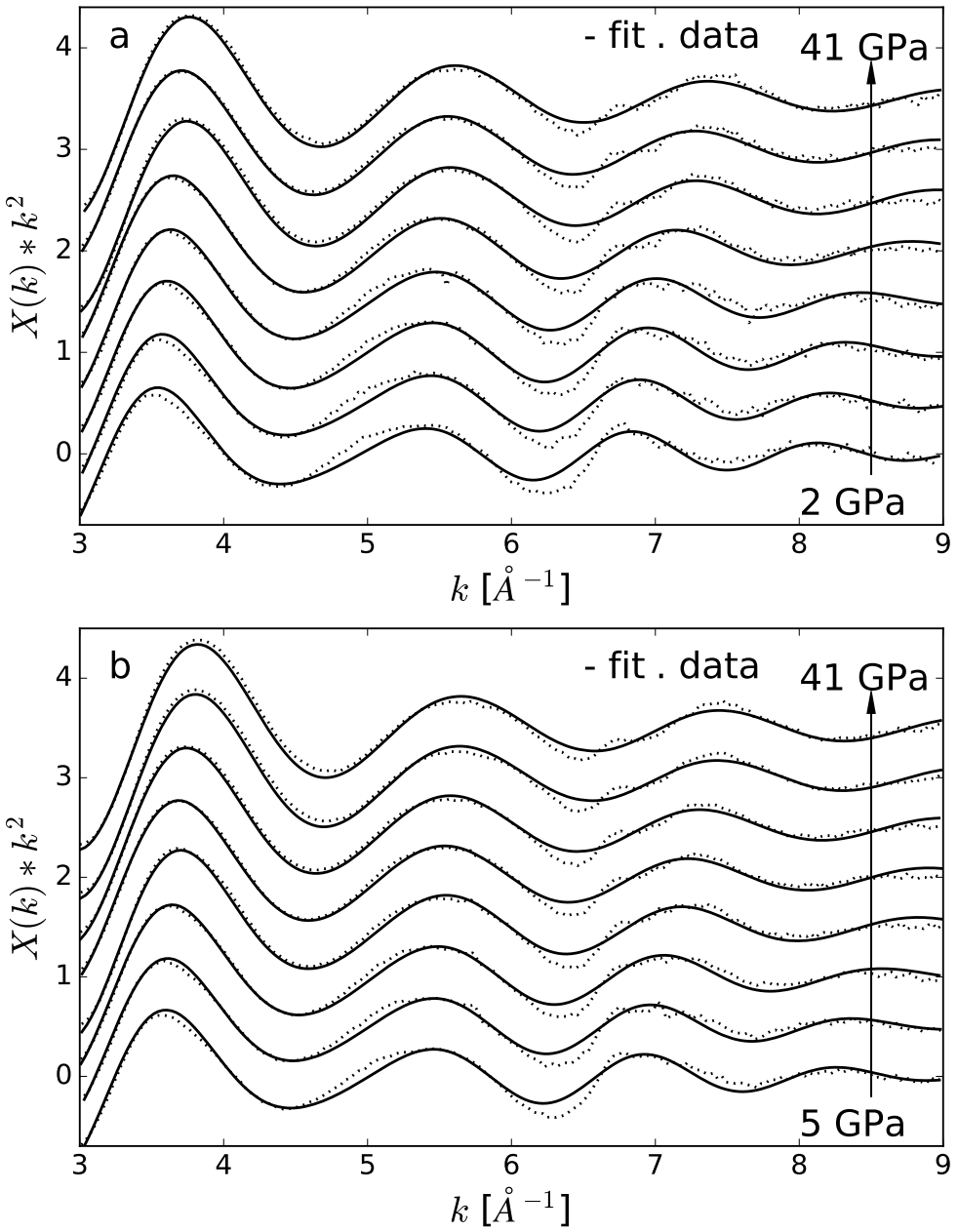

Figure 3.8: k^2 weighted EXAFS spectra (k^2 χ (k)) at the Sr K edge of Ab- (Fig. 3.8a) and AbDi-glass (Fig. 3.8b) and corresponding fits, shown as dashed and solid lines, respectively.

same coordination Al shows a larger average Al-O bond distance compared to Ge-O, and thus lower bond strength. Thus we may suggest that both Al and larger cations (Na, Mg, Ca, Sr) facilitate the simple compression behaviour of the Ge polyhedra in these glasses. This means, that once the next nearest cations Ge...Ge, Ge...Si or Si...Si reach critical threshold distances, further volume shrinkage is accommodated by the reduction of Na-O, Al-O and Ge-O (Si-O) bond lengths. This may proceed until critical values for the next-nearest neighbour distance for all other pairs are reached, e.g. Al...Ge, Na...Ge, Ca...Ge (in analogy also for Si) or constraints for O bond valence sums are violated. Only in this situation polyhedral distortion or further increase of the coordination number (CN) would be observed. The continuously decreasing trend of the Ge-O distance of the AbDi-glass suggests, however, that the critical values have not been reached in the entire investigated pressure range. For $NaAlGe_3O_8$ glass, a flattening of the Ge-O bond-length is observed above 110 GPa, which could indicate the onset of distortion for this germanate glass as proposed by Krstulović et al. (2020).

In this work, we used Ge to monitor pressure induced structural response of Si in aluminosilicate glasses. Due to very strong similarity of the $R_{\text{Ge-O}}$ pressure trend in pure Ge-albite $NaAlGe_3O_8$ (Krstulović et al., 2020) and in predominantly silicate compositions Ab- and AbDi-glass, we assume that primarily larger and lower charge cations than Ge such as Na, Ca, Mg or Sr, as well as Al govern structural response around Ge, but also around Si in the aluminosilicate samples (see for example Ghosh and Karki, 2018). Thus, we cannot conclude whether Si influences the behaviour of Ge, as the structural contribution of alkali and alkaline earth metals is more pronounced.

3.4.2 Structural changes of Sr in aluminosilicate glasses upon compression

Strontium (Sr) is an important trace element of the Earths' interior and is commonly found as substitute for Ca (e.g. Kato et al., 1988). In this role it can be well incorporated in silicate minerals, and, in contrast to many other trace elements, it is also highly compatible in carbonate minerals and carbonaceous melts (Pohlenz et al., 2018; Veksler et al., 1998). In crystalline materials Sr is found in various Ca analogue compounds including $SrSiO_3$ strontium metasilicate (Kato et al., 1988), the feldspar strontian $SrAl_2Si_2O_8$, as $Sr(OH)_2$, and the carbonate strontianite in aragonite structure. The coordination number ($N_{\text{Sr-O}}$) and the Sr-O bond lentghs ($R_{\text{Sr-O}}$) range from 7 to 9 and from 2.565 to 2.915 Å (Biedermann et al., 2020; Chiari et al., 1975; Grueninger and Bäringhausen, 1969; Grundy and Ito, 1974; Machida et al., 1982; Nedić et al., 2008; Nishi, 1997), with the longest bond distances in aluminosilicates and shortest in $Sr(OH)_2$.

In silicate melts, Sr preferentially acts as network modifier (Henderson et al., 1985) where it favourably occupies the vacant sites in the 6-fold silicate-polyhedra ring structures, but also breaks inter-tetrahedral connections, and favours the generation of NBOs. In spite of its tendency to enter NBO-rich environments, in the presence of cations with higher bond strength it can adapt also to BO-dominated environment, due to its lower capacity to supply charge requirements for NBOs (Pohlenz et al., 2018). In aluminosilicate glasses, Sr is often surrounded by BOs, when it charge-compensates Al (Cormier et al., 1999). Thus, in silicate melts and glasses at ambient pressure, Sr can adapt a dual role and it is incorporated in multiple structural sites resulting in a large variety of observed $N_{\text{Sr-O}}$ from 5 to ∼9 and $R_{\text{Sr-O}}$ from 2.5 to 2.74 Å (Charpentier et al., 2018; Cormier et al., 1999; Creux et al., 1995; Johnson et al., 2007; Kohn et al., 1990; McKeown et al., 2003; Pohlenz et al., 2018; Xiang and Du, 2011).

Table 3.6: Fit results on Sr K edge in AbDi-glass upon compression to 41 GPa. Free parameters are $R_{\text{Sr-O}}$, $R_{\text{Sr-Si}}$, $\sigma^2_{\text{Sr-O}}$, $\sigma^2_{\text{Sr-Si}}$, $h_{\text{Sr-Si}}$ and first shell ΔE_0. $N_{\text{Sr-O}}$ and $N_{\text{Sr-Si}}$ are treated as fixed parameters that are linearly correlated. Second shell ΔE_0 was set to be fixed parameter with equal values to the first shell ΔE_0. Asymmetry parameter $h_{\text{Sr-O}}$ is usually set to a fixed value. χ^2 indicates the fit quality. The standard deviation for free fit parameters is given in parentheses and refers to the last printed digit.

P [GPa]	$R_{\text{Sr-O}}$ $R_{\text{Sr-Si}}$	$N_{\text{Sr-O}}$ $N_{\text{Sr-Si}}$	$\sigma^2_{\text{Sr-O}}$ $\sigma^2_{\text{Sr-Si}}$	$h_{\text{Sr-O}}$ $h_{\text{Sr-Si}}$	ΔE_0	χ^2
5.5 (1)	2.581 (7) 3.53 (10)	6.2	0.01 (1) 0002 (4)	0.075 0.181 (1)	5.0 (4)	0.08
10.4 (1)	2.592 (7) 3.53 (10)	6.4	0.008 (9) 0.003 (4)	0.09 0.185 (1)	5.1 (4)	0.07
15.8 (1)	2.593 (7) 3.50 (10)	6.8	0.005 (8) 0.008 (3)	0.105 0.186 (1)	5.0 (4)	0.06
21.4 (2)	2.602 (7) 3.40 (10)	7.5	0.002 (8) 0.02 (3)	0.124 0.163 (1)	5.6 (4)	0.06
26.4 (2)	2.605 (7) 3.40 (10)	7.8	0.002 (7) 0.02 (3)	0.132 0.175 (1)	4.8 (4)	0.06
32.2 (2)	2.603 (7) 3.34 (10)	8.3	0.001 (7) 0.03 (4)	0.139 0.167 (1)	5.1 (4)	0.06
37 (3)	2.598 (7) 3.22 (10)	8.7	0.001 (7) 0.04 (4)	0.149 0.15 (1)	5.2 (4)	0.06
41.5 (3)	2.594 (7) 3.288 (10)	8.9	0.0003 (7) 0.03 (4)	0.148 0.180	5.4 (4)	0.06

Usually, higher values of $R_{\text{Sr-O}}$ and $N_{\text{Sr-O}}$ are found in aluminosilicate glasses (2.54, 2.63, 2.7 Å and $N_{\text{Sr-O}}$ 5.9, 7) compared to alumina-free silicate glasses (2.5, 2.55, 2.62 Å, and $N_{\text{Sr-O}}$ 5.8 and 6) (Cormier et al., 1999). In the same manner, $R_{\text{Sr-O}}$ in peralkaline and peraluminous glass are differing with 2.62 vs. 2.70 Å (Borchert et al., 2014). This variability of $R_{\text{Sr-O}}$ in depolymerized silicate glasses can be explained by the dual role of Sr. If Sr is acting as network modifier low values of $R_{\text{Sr-O}}$ to NBOs are allowed, whereas in association with BOs when Sr takes the role as charge compensator for Al, the values of $R_{\text{Sr-O}}$ are ruled by the O bond valence sum (Cormier et al., 1999; Pohlenz et al., 2018; Simon et al., 2013).

The results of the present study reveal a Sr coordination number ($N_{\text{Sr-O}}$) of ca. 6 and a bond distance ($R_{\text{Sr-O}}$) of 2.58 Å at the lowest probed pressures of 2 and 5.5 GPa for Ab- and AbDi-glass respectively (Tables 3.5 and 3.6). These values are consistent with those previously reported for silicate and aluminosilicate glasses at ambient conditions (Pohlenz et al., 2018; references therein). It should be noted here, that the bond distances and coordination numbers extracted by EXAFS represent average values, which is important for Sr that may occupy different structural sites in a glass as discussed above. Systematic investigations of the local

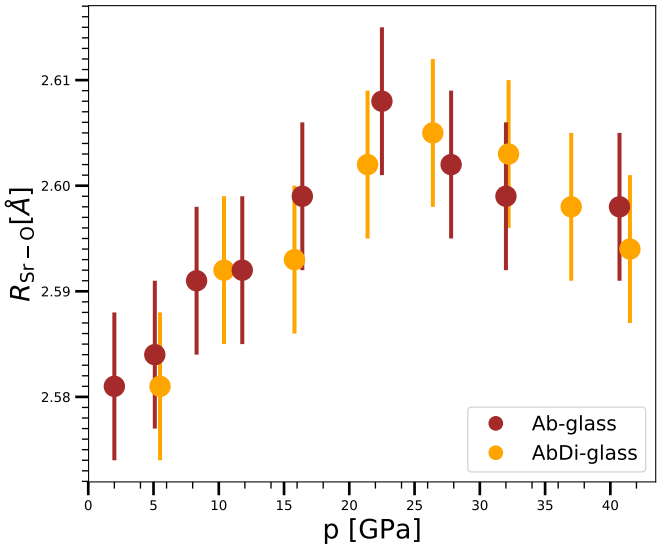

Figure 3.9: Evolution of the average Sr-O distance of the first coordination shell ($R_{\text{Sr-O}}$) of Ab- (brown) and AbDi-glass (orange) with pressure, obtained from fitting the experimental spectra.

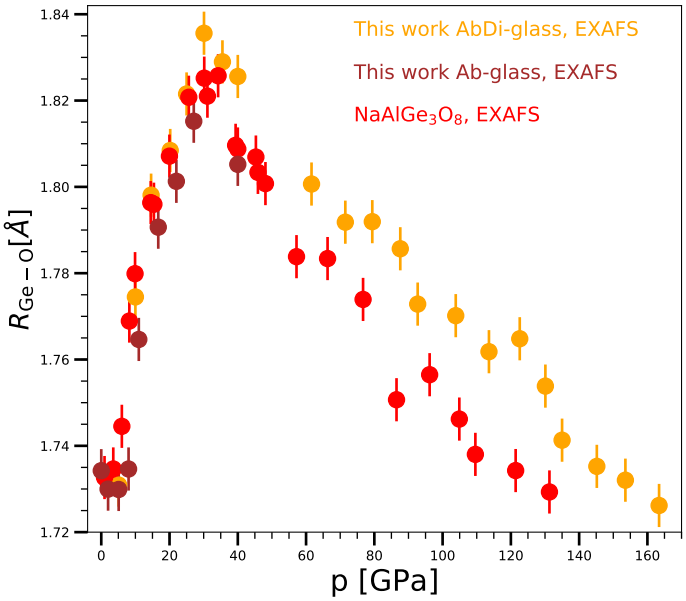

Figure 3.10: Evolution of Ge-O distances as a function of pressure for AbDi- (orange) and Ab-glass (brown) compared to the literature values on $NaAlGe_3O_8$ glass (red) (Krstulović et al., 2020).

atomic environment of Sr in silicate glasses at pressures exceeding conditions of the shallow Earth's mantle are not available. Beyond ∼6 GPa and up to 26 GPa we observe an increase of $R_{\text{Sr-O}}$ with a $\Delta R \leq 0.03$ Å (Fig. 3.9) that is considerably smaller than the one observed for $R_{\text{Ge-O}}$ ($\Delta R = \sim 0.10$ Å) in the same pressure range (Fig. 3.4). This variation in $R_{\text{Sr-O}}$ is also close to the resolution limit of EXAFS, given the limited k-range used for the fit. Beyond this pressure, the $R_{\text{Sr-O}}$ slightly decreases. Along the probed pressure interval, the fitted number of neighbours $N_{\text{Sr-O}}$ continuously increases from ∼6 at the lowest pressure to ∼9 at 41 GPa.

Due to missing data on pressure induced structural changes of Sr in amorphous samples in the literature, we will compare the results of this work with previous observations on Sr in crystalline silicates and carbonates. Further, we will make comparison to pressure driven structural changes of Mg in $MgSiO_3$ glass (Kim et al., 2019), as well as of Ca in amorphous aluminosilicate compounds at high pressure and high temperature revealed by means of MD simulations (Bajgain et al., 2015; Ghosh and Karki, 2018; Spera et al., 2009).

At low pressure, the $R_{\text{Sr-O}}$ and number of neighbours in Ab- and AbDi- glasses are consistent with those in crystalline samples such as $SrSiO_3$ meta-silicate ($N_{\text{Sr-O}} = 7$, $R_{\text{Sr-O}} = 2.65$ Å) or $Sr(OH)_2$ ($N_{\text{Sr-O}} = 7$, $R_{\text{Sr-O}} = 2.60$ Å) (Grueninger and Bäringhausen, 1969; Nishi, 1997) although both compounds are not ideal models of the local structure in glasses. Above 20 GPa and at high temperature, $SrSiO_3$ transforms into the perovskite structure (Xiao et al., 2013; Yusa et al., 2005). This high pressure phase exhibits a 12-fold coordinated Sr with an average $R_{\text{Sr-O}}$ distance of 2.45 Å at 32 GPa (Xiao et al., 2013). The carbonate strontianite exhibits a $N_{\text{Sr-O}}$ of 9 up to about 26 GPa, where it transforms into the post-aragonite structure, with $N_{\text{Sr-O}} = 12$ (Biedermann et al., 2020; Wang et al., 2015) and with much shorter $R_{\text{Sr-O}}$ distances compared to that in strontianite at ambient pressure, i.e. 2.417 vs. 2.565 Å (Biedermann et al., 2020).

A comparison of this compilation with the results determined here at elevated pressure, reveals significantly longer $R_{\text{Sr-O}}$ distances in the studied glasses compared to those reported for 12-fold coordinated Sr in crystalline compounds at similar pressures. Further, the fitted $N_{\text{Sr-O}}$ parameter reached only a value of 9 at the highest pressure. An overestimation of bond distances is rare for EXAFS because usually anharmonicity due to configurational disorder leads to underestimation of bond distances. In our data analysis we have considered this effect by using asymmetric distribution for the fit. As reported earlier, Sr EXAFS shows multi-electronic excitations, MEE (D'Angelo et al., 1996) that distort the EXAFS signal. These MEE often appear in the spectra as step-like features and may affect the phase and amplitude of the EXAFS, especially if the EXAFS signal is weak due to significant disorder. In our extracted EXAFS function (Fig. 3.7a) at about 6.6 Å 1 a MEE is visible, which should correspond to the KM 4,5 excitations. To minimize the effect on the analysis, the Sr data were only k^2-weighted during fitting, which reduces the weight on the higher k-range. Still, we cannot rule out that our results are affected and as shown by D'Angelo et al. (1996), these features may lead to an underestimation of the EXAFS amplitude and thus to underestimated $N_{\text{Sr-O}}$. However, analysis of high-resolution XANES spectra of crystalline compounds, glasses and aqueous solutions by ab-initio modelling of spectra based on structural models (Borchert et al., 2014) revealed structural parameters that are consistent with those found here for low pressure samples. In the light of this potential limitation, the absolute values of the observed number of structural parameters found here should be treated with caution. Still, the relative changes with pressure will likely persist, as shown by other EXAFS examples (e.g. Pohlenz et al., 2018; Simon et al., 2013).

Even though data on Sr in crystalline compounds at these pressures are still scarce and not directly transferable to the present aluminosilicate systems, the discrepancy between

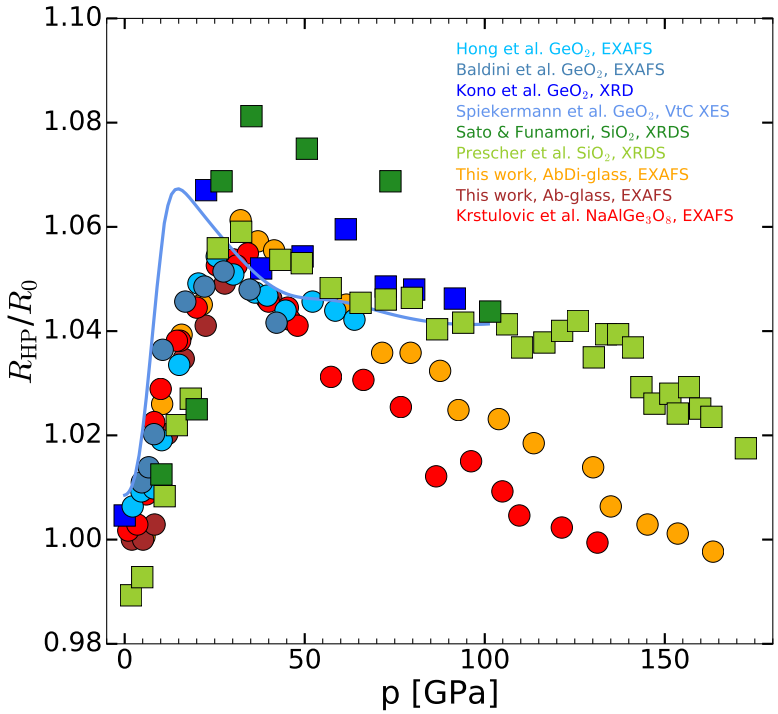

Figure 3.11: Comparison of the pressure induced evolution of the normalized Ge-O i.e. Si-O bond distance expressed by the ratio R_{HP}/R_0 for Ab-glass, AbDi-glass, $NaAlGe_3O_8$ glass (warm colours), GeO_2 glass (blue colours), SiO_2 glass (green colours). Squares are used for XRD, circles for EXAFS, and full line for VtC-XES.

the reports for $SrSiO_3$ perovskite (Xiao et al., 2013; Yusa et al., 2005), but also for $SrCO_3$ in post-aragonite (Biedermann et al., 2020; Wang et al., 2015) on one hand, and aluminosilicate glasses studied here on the other hand, require explanation. Following the observation on the crystalline samples, one could assume that also in aluminosilicate glasses Sr, as a large cation, might be able to tolerate further oxygen neighbours without extension of distances. In contrast, Mg in amorphous $MgSiO_3$ under compression shows continuous reduction of the Mg-O distance along with a constant increase of the number of neighbours from 5 to ∼8 (Kim et al., 2019). The increase of $R_{Sr\text{-}O}$ distances could be at least to some extent explained in the light of the charge-compensating role of Sr cations, which may inhibit contraction of $R_{Sr\text{-}O}$, in contrast to $MgSiO_3$ glass, where Mg acts as a typical network modifier.

Along with the potential role of Sr as charge compensator for Al, the tendency of the Sr-O bond distance to increase with pressure may thus be a sign for a stronger increase of the coordination number than in the case of Mg. We assume that the fitted $N_{Sr\text{-}O}$ is a lower limit of possible coordination numbers at the highest probed pressure of 41 GPa in aluminosilicate glasses studied here. A coordination number of at least 9 may be also supported by MD simulation studies on anorthititic and basaltic liquids at high pressure and temperature conditions (Bajgain et al., 2015; Ghosh and Karki, 2018; Spera et al., 2009). In these studies, the coordination number of Ca, which we may assume as structurally similar to Sr, increases strongly up to 20 or 30 GPa, where it reaches coordination number 9 (Ghosh and Karki, 2018) and 10 (Bajgain et al., 2015; Spera et al., 2009). We conclude that Sr in studied aluminosilicate glasses plays a dual role as network modifier and charge compensator and that it, similar to Ge, experiences strongest structural variations within the first ∼20 to ∼30 GPa.

3.4.3 Implications for melts in the lower mantle

Comparably large and highly compressible cations such as alkali and alkaline earth metals are important constituents of natural melts throughout the Earth's mantle. Thus, particularly the AbDi-glass represents an important cross-link between simple fully polymerized melt compositions and those that are relevant for processes in the deep Earth. In the literature, potential natural melt compositions of the deep Earth were approached so far, by studying $MgSiO_3$ glass as a representative of the ambient lower mantle mineralogy (Kim et al., 2019; Kono et al., 2018; Murakami and Bass, 2011; Petitgirard et al., 2015). Of particular interest in those studies was the question whether these melts may reach densities similar to or higher than those of the corresponding crystalline counterparts, such as bridgmanite. This is an important constraint for the potential presence of high-density silicate magmas at the base of the mantle, which is often inferred to explain observed ultra-low velocity zones (ULVZ) close to the core-mantle boundary (CMB) (Nomura et al., 2014; Yuan and Romanowicz, 2017).

The hypothesis that the lower mantle may produce a partial melt that is sufficiently dense to adequately represent the ULVZs was put under question due to its high melting temperature (Andrault et al., 2014; Thomas and Asimow, 2013). A CMB temperature far above ∼4150 K would be required to partially melt pyrolitic or chondritic material and would require a much hotter core (Andrault et al., 2014). Andrault et al. (2014) showed that suppression of the melting temperature could be reached by introducing minute amounts of highly fusible components, such as alkalies or volatiles. Along with these discussions, subducted oceanic crust as the origin of the large low shear velocity provinces (LLSVPs) and ULVZ at the base of the mantle has been proposed (Andrault et al., 2014; Jones et al., 2020; Pradhan et al., 2015; Thomson et al., 2019). Recently, Jones et al. (2020) used large-scale geodynamic modelling to demonstrate that LLSVPs at the CMB could originate from subducted basaltic, initially cold, lithosphere that accumulates at the CMB due to its excess density. According to their model, these large provinces are basalt-rich at the lower 100 to 200 km, and grade into the surrounding peridotite towards the sides and the top. The reduced velocity is related to warming over billions of years (Jones et al., 2020). At the edges and at the bottom of these large provinces, in ULVZs, the presence of the molten MORB-component was proposed based on their lower melting temperature compared to the bulk mantle at pressure conditions of the CMB (Andrault et al., 2014; Pradhan et al., 2015). According to these studies, such partial melts could be gravitationally stable at the conditions of the CMB, which is consistent with measurements of the density of molten basalt up to 60 GPa and 2300 K (Sanloup et al., 2013).

In the light of the recent work on structural properties of glasses (Kim et al., 2019; Kono et al., 2016; Kono et al., 2018; Krstulović et al., 2020; Prescher et al., 2017; Spiekermann et al., 2019) and our data on the AbDi-glass we may conclude, that the density of a stagnant basaltic melt may be related to the difference in composition rather than to a different structural densification mechanism in non-crystalline compounds, consistent with findings of Andrault et al. (2014) and Thomson et al. (2019).

Acknowledgements

We thank the entire staff of the beamline BM23 of the European Synchrotron Radiation Facility (ESRF), in particular S. Pascarelli and O. Mathon, for providing us two experimental sessions to perform the experiment. We strongly recognize the technical support provided by F. Perrin and S. Pasternak. We warmly thank also J. Jacobs from the high-pressure sample environment for his assistance with high-pressure instrumentation, and R. Torchio for providing

the measurements on reference samples. We highly acknowledge Christina Günter (Institute of Geosciences, University of Potsdam) for the chemical analysis of the samples as well as Rico Fuchs for help during the sample synthesis. We also thank H. P. Nabein from German Research Centre for Geosciences (GFZ) for checking the amorphous nature of the synthesized glasses using XRD. M.W. would like to acknowledge funding by Deutsche Forschungsgemeinschaft (DFG) through Project Wi 2000/13-1.

Adenis, A., Debayle, E., Ricard, Y., 2017. Attenuation tomography of the upper mantle. Geophys. Res. Lett. 44 (15), 7715–7724. https://doi.org/10.1002/2017GL073751.

Andrault, D., Petitgirard, S., Lo Nigro, G., Devidal, J.L., Veronesi, G., Garbarino, G., Mezouar, M., 2012. Solid-liquid iron partitioning in Earth's deep mantle. Nature 487 (7407), 354–357. https://doi.org/10.1038/nature11294.

Andrault, D., Pesce, G., Bouhifd, M.A., Bolfan-Casanova, N., Heńot, J.M., Mezouar, M., 2014. Melting of subducted basalt at the core-mantle boundary. Science 344 (6186), 892–895. https://doi.org/10.1126/science.1250466.

Anzellini, S., Dewaele, A., Occelli, F., Loubeyre, P., Mezouar, M., 2014. Equation of state of rhenium and application for ultra high pressure calibration. J. Appl. Phys. 115 (4) https://doi.org/10.1063/1.4863300.

Bajgain, S., Ghosh, D.B., Karki, B.B., 2015. Structure and density of basaltic melts at mantle conditions from first-principles simulations. Nat. Commun. 6 https://doi.org/10.1038/ncomms9578.

Baldini, M., Aquilanti, G., Mao, H.K., Yang, W., Shen, G., Pascarelli, S., Mao, W.L., 2010. High-pressure EXAFS study of vitreous GeO_2 up to 44 GPa. Phys. Rev. B - Condensed Matter Mater. Phys. 81 (2) https://doi.org/10.1103/PhysRevB.81.024201.

Benmore, C.J., Soignard, E., Amin, S.A., Guthrie, M., Shastri, S.D., Lee, P.L., Yarger, J.L., 2010. Structural and topological changes in silica glass at pressure. Phys. Rev. B - Condensed Matter Mater. Phys. 81 (5) https://doi.org/10.1103/PhysRevB.81.054105.

Biedermann, N., Bykova, E., Morgenroth, W., Efthimiopoulos, I., Mueller, J., Spiekermann, G., Glazyrin, K., Pakhomova, A., Appel, K., Wilke, M., 32, 2020. Equation of state and high-pressure phase behavior of $SrCO_3$. Eur. J. Mineral.

Boehler, R., De Hantsetters, K., 2004. New anvil designs in diamond-cells. High Pressure Res. 24 (3), 391–396. https://doi.org/10.1080/08957950412331323924.

Borchert, M., Wilke, M., Schmidt, C., Kvashnina, K., Jahn, S., 2014. Strontium complexation in aqueous solutions and silicate glasses: Insights from high energy resolution fluorescence detection X-ray spectroscopy and ab-initio modeling. Geochim. Cosmochim. Acta

142, 535–552. https://doi.org/10.1016/j. gca.2014.07.010.

Buffett, B.A., Garnero, E.J., Jeanloz, R., 2000. Sediments at the top of Earth's core. Science 290 (5495), 1338–1342. https://doi.org/10.1126/science.290.5495.1338.

Charpentier, T., Okhotnikov, K., Novikov, A.N., Hennet, L., Fischer, H.E., Neuville, D.R., Florian, P., 2018. Structure of strontium aluminosilicate glasses from molecular dynamics simulation, neutron diffraction, and nuclear magnetic resonance studies. J. Phys. Chem. B 122 (41), 9567–9583. https://doi.org/10.1021/acs.jpcb.8b05721.

Chiari, G., Calleri, M., Bruno, E., Ribbe, E., 1975. The structure of partially disordered, synthetic strontium feldspar. Am. Mineral. 60, 111–119.

Cormier, L., Calas, G., Creux, S., Gaskell, P.H., Bouchet-Fabre, B., Hannon, A.C., 1999. Environment around strontium in silicate and aluminosilicate glasses. Phys. Rev. B 59, 13517–13520. https://doi.org/10.1103/PhysRevB.59.13517.

Creux, S., Bouchet-Fabre, B., Gaskell, P.H., 1995. Anomalous wide angle X-ray scattering study of strontium silicate and aluminosilicate glasses. J. Non-Cryst. Solids 192–193, 360–363. https://doi.org/10.1016/0022-3093(95)00377-0.

D'Angelo, P., Nolting, H.F., Pavel, N.V., 1996. Evidence for multielectron resonances at the Sr K edge. Phys. Rev. A - Atomic, Mol. Optical Phys. 53 (2), 798–805. https://doi.org/10.1103/PhysRevA.53.798.

Durben, D.J., Wolf, G.H., 1991. Raman spectroscopic study of the pressure-induced coordination change in GeO_2 glass. Phys. Rev. B 43 (3), 2355–2363. https://doi.org/10.1103/PhysRevB.43.2355.

Dutta, R., White, C.E., Greenberg, E., Prakapenka, V.B., Duffy, T.S., 2018. Equation of state of the α PbO_2 and Pa3-type phases of GeO_2 to 120 GPa. Phys. Rev. B 98 (14). https://doi.org/10.1103/physrevb.98.144106.

Fiquet, G., 2018. Melting in the Earth's deep interior. In: Magmas Under Pressure: Advances in High-Pressure Experiments on Structure and Properties of Melts. Elsevier, pp. 115–134. https://doi.org/10.1016/B978-0-12-811301-1.00004-6.

Ghosh, D.B., Karki, B.B., 2018. First-principles molecular dynamics simulations of anorthite ($CaAl_2Si_{28}$) glass at high pressure. Phys. Chem. Miner. 45 (6), 575–587. https://doi.org/10.1007/s00269-018-0943-4.

Grueninger, H.W., Bäringhausen, H., 1969. Die Kristallstruktur von Strontiumhydroxid $Sr(OH)_2$. ZAAC - J. Inorg. Gen. Chem. 368 (1–2), 53–61.

https://doi.org/10.1002/zaac.19693680109.

Grundy, H.D., Ito, J., 1974. The refinement of the crystal structure of a synthetic non-stoichiometric Sr feldspar. Am. Mineral. 59 (11 12), 1319–1326.

Ha, M.T., Garofalini, S.H., 2017. Local structure of network modifier to network former ions in soda-lime alumino-borosilicate glasses. J. Am. Ceram. Soc. 100 (2), 563–573. https://doi.org/10.1111/jace.14565.

Henderson, P., Nolan, J., Cunningham, G.C., Lowry, R.K., 1985. Structural controls and mechanisms of diffusion in natural silicate melts. Contrib. Mineral. Petrol. 89, 263–272. https://doi.org/10.1007/BF00379459.

Hirose, K., Fei, Y., Ma, Y., Mao, H.K., 1999. The fate of subducted basaltic crust in the Earth's lower mantle. Nature 397 (6714), 53–56. https://doi.org/10.1038/16225.

Hong, X., Newville, M., Duffy, T.S., Sutton, S.R., Rivers, M.L., 2014. X-ray absorption spectroscopy of GeO_2 glass to 64 GPa. J. Phys. Condens. Matter 26 (3). https://doi.org/10.1088/0953-8984/26/3/035104.

Irifune, T., Kurio, A., Sakamoto, S., Inoue, T., Sumiya, H., 2003. Materials: Ultrahard polycrystalline diamond from graphite. Nature 421, 599–600. https://doi.org/10.1038/421806b.

Itié, J.P., Polian, A., Calas, G., Petiau, J., Fontaine, A., Tolentino, H., 1989. Pressure-induced coordination changes in crystalline and vitreous GeO_2. Phys. Rev. Lett. 63 (4), 398–401. https://doi.org/10.1103/PhysRevLett.63.398.

Johnson, J.A., Urquidi, J., Holland, D., Johnson, C.E., Appelyard, P.G., 2007. Strontium environment transition in tin silicate glasses by neutron and X-ray diffraction. J. Non-Cryst. Solids 353, 4084–4092. https://doi.org/10.1016/j.jnoncrysol.2007.06.015.

Jones, T.D., Maguire, R.R., van Keken, P.E., Ritsema, J., Koelemeijer, P., 2020. Subducted oceanic crust as the origin of seismically slow lower-mantle structures. Progr. Earth Planet. Sci. 7 (1) https://doi.org/10.1186/s40645-020-00327-1.

Kato, T., Ringwood, A.E., Irifune, T., 1988. Experimental determination of element partitioning between silicate perovskites, garnet and liquids: constraints on early differentiation of the mantle. Earth Planet. Sci. Lett. 89, 123–145.

Kim, Y.H., Yi, Y.S., Kim, H.I., Chow, P., Xiao, Y., Shen, G., Lee, S.K., 2019. Structural transitions in $MgSiO_3$ glasses and melts at the core-mantle boundary observed via inelastic X-ray scattering. Geophys. Res. Lett. 46 (23), 13756–13764.

https://doi.org/10.1029/2019GL085889.

Kohn, S.C., Charnock, J.M., Henderson, C.M.B., Greaves, G.N., 1990. The structural environments of trace elements in dry and hydrous silicate glasses; a manganese and strontium K-edge X-ray absorption spectroscopic study. Contrib. Mineral. Petrol. 105, 359–368. https://doi.org/10.1007/BF00306545.

Kono, Y., Kenney-Benson, C., Ikuta, D., Shibazaki, Y., Wang, Y., Shen, G., Navrotsky, A., 2016. Ultrahigh-pressure polyamorphism in GeO_2 glass with coordination number > 6. Proc. Natl. Acad. Sci. U. S. A. 113 (13), 3436–3441. https://doi.org/10.1073/pnas.1524304113.

Kono, Y., Shibazaki, Y., Kenney-Benson, C., Wang, Y., Shen, G., 2018. Pressure-induced structural change in $MgSiO_3$ glass at pressures near the Earth's core–mantle boundary. Proc. Natl. Acad. Sci. U. S. A. 115 (8), 1742–1747. https://doi.org/10.1073/pnas.1716748115.

Krstulović, M., Rosa, A.D., Biedermann, N., Spiekermann, G., Irifune, T., Muñoz, M., Wilke, M., 2020. Ge coordination in $NaAlGe_3O_8$ glass upon compression to 131 GPa. Phys. Rev. B 101, 214103. https://doi.org/10.1103/PhysRevB.101.214103.

Lee, S.K., Lin, J.F., Cai, Y.Q., Hiraoka, N., Eng, P.J., Okuchi, T., Mao, H., Meng, Y., Hu, M. Y., Chow, P., Shu, J., Li, B., Fukui, H., Lee, B.H., Kim, H.N., Yoo, C.S., 2008. X-ray Raman scattering study of $MgSiO_3$ glass at high pressure: Implication for triclustered $MgSiO_3$ melt in Earth's mantle. Proc. Natl. Acad. Sci. U. S. A. 105 (23), 7925–7929. https://doi.org/10.1073/pnas.0802667105.

Letoullec, R., Pinceaux, J.P., Loubeyre, P., 1988. The Membrane Diamond Anvil Cell: a new device for generating continuous pressure and temperature variations. High Pressure Res. 1 (1), 77–90. https://doi.org/10.1080/08957958808202482.

Machida, K.I., Adachi, G.Y., Shiokawa, J., Shimada, M., Koizumi, M., 1982. Structure and high-pressure polymorphism of strontium metasilicate. Acta Crystallogr. Sec. B Struct. Crystallogr. Crystal Chem. 38 (2), 386–389.
https://doi.org/10.1107/s0567740882003045.

Majérus, O., Cormier, L., Itié, J.-P., Galoisy, L., Neuville, D.R., Calas, G., 2004. Pressure-induced Ge coordination change and polyamorphism in SiO_2 - GeO_2 glasses. J. Non-Cryst. Solids 34–38. https://doi.org/10.1016/j.jnoncrysol.2004.07.039, 345 and 346.

Mao, H.K., Bell, P.M., Shaner, J.W., Steinberg, D.J., 1978. Specific volume measurements of Cu, Mo, Pd, and Ag and calibration of the ruby R1 fluorescence pressure gauge from 0.06 to 1Mbar. J. Appl. Phys. 49, 3276. https://doi.org/10.1063/1.325277.

Mathon, O., Beteva, A., Borrel, J., Bugnazet, D., Gatla, S., Hino, R., Kantor, I., Mairs, T., Munoz, M., Pasternak, S., Perrin, F., Pascarelli, S., 2015. The time-resolved and extreme conditions XAS (Texas) facility at the European Synchrotron Radiation Facil-

ity: the general-purpose EXAFS bending-magnet beamline BM23. J. Synchrotron Radiat. 22, 1548–1554. https://doi.org/10.1107/S1600577515017786.

McKeown, D.A., Kot, W.K., Pegg, I.L., 2003. X-ray absorption studies of the local strontium environments in borosilicate waste glasses. J. Non-Cryst. Solids 317, 290–300. https://doi.org/10.1016/S0022-3093(02)01816-1.

Meade, C., Hemley, R.J., Mao, H.K., 1992. High-pressure x-ray diffraction of SiO_2 glass. Phys. Rev. Lett. 69 (9), 1387–1390. https://doi.org/10.1103/PhysRevLett.69.1387.

Murakami, M., Bass, J.D., 2010. Spectroscopic evidence for ultrahigh-pressure polymorphism in SiO_2 glass. Phys. Rev. Lett. 104 (2)
https://doi.org/10.1103/PhysRevLett.104.025504.

Murakami, M., Bass, J.D., 2011. Evidence of denser $MgSiO_3$ glass above 133 gigapascal (GPa) and implications for remnants of ultradense silicate melt from a deep magma ocean. Proc. Natl. Acad. Sci. U. S. A. 108 (42), 17286–17289. https://doi.org/10.1073/pnas.1109748108.

Mysen, B.O., Virgo, D., Seifert, F.A., 1985. Relationships between properties and structure of aluminosilicate melts. Am. Mineral. 70, 88–105.

Nedić, B., Kremenović, A., Dondur, V., Dimitrijević, R., 2008. Strontium deficient feldspar - Structure and X - Ray powder diffraction line broadening analysis. Cryst. Res. Technol. 43 (3), 266–272. https://doi.org/10.1002/crat.200710974.

Nishi, F., 1997. Strontium metasilicate, $SrSiO_3$. Acta Crystallogr. Sect. C: Cryst. Struct. Commun. 53 (5), 534–536. https://doi.org/10.1107/S0108270196015338.

Niu, Y., O'Hara, M.J., 2004. Basaltic melts in the lower mantle condltions are denser than ambient solid peridotites. In: Hekinian, R., Cheminée, J.-L., Stoffers, P. (Eds.), Oceanic hotspots. Interplate Submarine Magmatism and Tectonism. Springer-Verlag Berlin Heidelberg. https://doi.org/10.1007/978-3-642-18782-7.

Nomura, R., Hirose, K., Uesugi, K., Ohishi, Y., Tsuchiyama, A., Miyake, A., Ueno, Y., 2014. Low core-mantle boundary temperature inferred from the solidus of pyrolite. Science 343 (6170), 522–525. https://doi.org/10.1126/science.1248186.

Ohtani, E., Maeda, M., 2001. Density of basaltic melt at high pressure and stability of the melt at the base of the lower mantle. Earth Planet. Sci. Lett. 193 (1–2), 69–75. https://doi.org/10.1016/S0012-821X(01)00505-2.

O'Keeffe, M., Hyde, B.G., 1981. The role of nonbonded forces in crystals. In: O'Keeffe, M., Navrotsky, A. (Eds.), Structure and Bonding in Crystals, Vol. 1. Academic

Press Inc., New York, p. 227. Chap. 10.

Petitgirard, S., Malfait, W.J., Sinmyo, R., Kupenko, I., Hennet, L., Harries, D., Dane, T., Burghammer, M., Rubie, D.C., 2015. Fate of $MgSiO_3$ melts at core-mantle boundary conditions. Proc. Natl. Acad. Sci. U. S. A. 112 (46), 14186–14190. https://doi.org/10.1073/pnas.1512386112.

Petitgirard, S., Malfait, W.J., Journaux, B., Collings, I.E., Jennings, E.S., Blanchard, I., Kantor, I., Kurnosov, A., Cotte, M., Dane, T., Burghammer, M., Rubie, D.C., 2017. SiO_2 Glass Density to Lower-Mantle pressures. Phys. Rev. Lett. 119 (21) https://doi.org/10.1103/PhysRevLett.119.215701.

Petitgirard, S., Sahle, C.J., Weis, C., Gilmore, K., Spiekermann, G., Tse, J.S., Wilke, M., Cavallari, C., Cerantolla, V., Sternemann, C., 2019. Magma properties at deep Earth's conditions from electronic structure of silica. Geochem. Perspect. Lett. 9, 32–37. https://doi.org/10.7185/geochemlet.1902.

Pohlenz, J., Rosa, A.D., Mathon, O., Pascarelli, S., Belin, S., Landrot, G., Murzin, V., Veligzhanin, A., Shiryaev, A., Irifune, T., Wilke, M., 2018. Structural controls of CO_2 on Y, La and Sr incorporation in sodium-rich silicate - carbonate melts by *in-situ* high P-T EXAFS. Chem. Geol. 486, 1–15. https://doi.org/10.1016/j.chemgeo.2017.12.023.

Pradhan, G.K., Fiquet, G., Siebert, J., Auzende, A.L., Morard, G., Antonangeli, D., Garbarino, G., 2015. Melting of MORB at core-mantle boundary. Earth Planet. Sci. Lett. 431, 247–255. https://doi.org/10.1016/j.epsl.2015.09.034.

Prescher, C., Prakapenka, V.B., Stefanski, J., Jahn, S., Skinner, L.B., Wang, Y., 2017. Beyond sixfold coordinated Si in SiO_2 glass at ultrahigh pressures. Proc. Natl. Acad. Sci. U. S. A. 114 (38), 10041–10046. https://doi.org/10.1073/pnas.1708882114.

Rehr, J.J., Kas, J.J., Vila, F.D., Prange, M.P., Jorissen, K., 2010. Parameter-free calculations of X-ray spectra with FEFF9. Phys. Chem. Chem. Phys. 12, 5503–5513. https://doi.org/10.1039/b926434e.

Rosa, A.D., Mathon, O., Torchio, R., Jacobs, J., Pasternak, S., Irifune, T., Pascarelli, S., 2019. Nano-polycrystalline diamond anvils: Key devices for XAS at extreme conditions: their use, scientific impact, present status and future needs. High Pressure Res. 40, 65. https://doi.org/10.1080/08957959.2019.1700978.

Sanloup, C., Drewitt, J.W.E., Konôpková, Z., Dalladay-Simpson, P., Morton, D.M., Rai, W., van Westrenen, N., Morgenroth, W., 2013. Structural change in molten basalt at deep mantle conditions. Nature 503 (7474), 104–107. https://doi.org/10.1038/nature12668.

Sato, T., Funamori, N., 2010. High-pressure structural transformation of SiO_2 glass up to 100 GPa. Phys. Rev. B - Condensed Matter Mater. Phys. 82 (18)

https://doi.org/10.1103/PhysRevB.82.184102.

Shen, G., Mei, Q., Prakapenka, V.B., Lazor, P., Sinogeikin, S., Meng, Y., Park, C., 2011. Effect of helium on structure and compression behavior of SiO_2 glass. Proc. Natl. Acad. Sci. U. S. A. 108 (15), 6004–6007. https://doi.org/10.1073/pnas.1102361108.

Simon, S., Wilke, M., Chernikov, R., Klemme, S., Hennet, L., 2013. The influence of composition on the local structure around yttrium in quenched silicate melts - Insights from EXAFS. Chem. Geol. 346, 3–13.

Spera, F.J., Nevins, D., Ghiorso, M., Cutler, I., 2009. Structure, thermodynamic and transport properties of $CaAl_2Si_2O_8$ liquid. Part I: Molecular dynamics simulations. Geochim. Cosmochim. Acta 73 (22), 6918–6936. https://doi.org/10.1016/j.gca.2009.08.011.

Spiekermann, G., Harder, M., Gilmore, K., Zalden, P., Sahle, C.J., Petitgirard, S., Wilke, M., Biedermann, N., Weis, C., Morgenroth, W., Tse, J.S., Kulik, E., Nishiyama, N., Yavas, H., Sternemann, C., 2019. Persistent Octahedral Coordination in Amorphous GeO_2 up to 100 GPa by Kβ' X-Ray Emission Spectroscopy. Phys. Rev. X 9 (1). https://doi.org/10.1103/PhysRevX.9.011025.

Stebbins, J.F., 1995. Dynamics and structure of silicate and oxide melts: Nuclear magnetic resonance studies. In: Stebbins, J.F., McMillan, P.F., Dingwell, D.B. (Eds.), Structure, Dynamics and Properties of Silicate Melts, Vol. 32. Mineralogical Society of America, Washington, D.C., p. 191. Chap. 7.

Thomas, C.W., Asimow, P.D., 2013. Direct shock compression experiments on premolten forsterite and progress toward a consistent high-pressure equation of state for CaO-MgO-Al_2O_3-SiO_2-FeO liquids. J. Geophys. Res. Solid Earth 118 (11), 5738–5752. https://doi.org/10.1002/jgrb.50374.

Thomson, A.R., Crichton, W.A., Brodholt, J.P., Wood, I.G., Siersch, N.C., Muir, J.M.R., Dobson, D.P., Hunt, S.A., 2019. Seismic velocities of $CaSiO_3$ perovskite can explain LLSVPs in Earth's lower mantle. Nature 572 (7771), 643–647. https://doi.org/10.1038/s41586-019-1483-x.

Tse, J.S., Klug, D.D., Le Page, Y., 1992. High-pressure densification of amorphous silica. Phys. Rev. B 46 (10), 5933–5938. https://doi.org/10.1103/PhysRevB.46.5933.

Vaccari, M., Aquilanti, G., Pascarelli, S., Mathon, O., 2009. A new EXAFS investigation of local structural changes in amorphous and crystalline GeO_2 at high pressure. J. Phys. Condens. Matter 21 (14). https://doi.org/10.1088/0953-8984/21/14/145403.

Veksler, I.V., Petibon, C., Jenner, G.A., Dorfman, A.M., Dingwell, D.B., 1998. Trace element partitioning in immiscible silicate–carbonate liquid systems: an initial experimental

study using a centrifuge autoclave. J. Petrol. 39, 2095–2104.
https://doi.org/10.1093/petroj/39.11-12.2095.

Wang, M., Liu, Q., Nie, S., Li, B., Wu, Y., Gao, J., Wei, X., Wu, X., 2015. High-pressure phase transitions and compressibilities of aragonite-structure carbonates: $SrCO_3$ and $BaCO_3$. Phys. Chem. Miner. 42, 517–527. https://doi.org/10.1007/s00269-015-0740-2.

Weigel, C., Cormier, L., Calas, G., Galoisy, L., Bowron, D.T., 2008. Nature and distribution of iron sites in a sodium silicate glass investigated by neutron diffraction and EPSR simulation. J. Non-Cryst. Solids 354 (52–54), 5378–5385.
https://doi.org/10.1016/j.jnoncrysol.2008.09.030.

Williams, Q., Jeanloz, R., 1988. Spectroscopic evidence for pressure-induced coordination changes in silicate glasses and melts. Science 239 (4842), 902–905.
https://doi.org/10.1126/science.239.4842.902.

Winterer, M., 1997. XAFS - a data analysis program for materials science in proceedings of the 9th international conference on x-ray absorption fine structure. J. Phys. IV France 7, C2–243.

Wolf, G.H., McMillan, P.F., 1995. Pressure effects on silicate melt structure and properties. In: Stebbins, J.F., McMillan, P.F., Dingwell, D.B. (Eds.), Structure, Dynamics and Properties of Silicate Melts, Vol. 32. Mineralogical Society of America, Washington, DC, p. 50. Chap. 11.

Xiang, Y., Du, J., 2011. Effect of strontium substitution on the structure of 45S5 bioglasses. Chem. Mater. 23, 2703–2717. https://doi.org/10.1021/cm102889q.

Xiao, W., Tan, D., Zhou, W., Liu, J., Xu, J., 2013. Cubic perovskite polymorph of strontium metasilicate at high pressures. Am. Mineral. 98 (11–12), 2096–2104.
https://doi.org/10.2138/am.2013.4470.

Yuan, K., Romanowicz, B., 2017. Seismic evidence for partial melting at the root of major hot spot plumes. Science 357 (6349). https://doi.org/10.1126/science.aan0760.

Yusa, H., Akaogi, M., Sata, N., Kojitani, H., Kato, Y., Ohishi, Y., 2005. Unquenchable hexagonal perovskite in high-pressure polymorphs of strontium silicates. Am. Mineral. 90 (5–6), 1017–1020. https://doi.org/10.2138/am.2005.1835.

Zen, E.A., 1986. Aluminum enrichment in silicate melts by fractional crystallization: some mineralogic and petrographic constraints. J. Petrol. 27 (5), 1095–1117.
https://doi.org/10.1093/petrology/27.5.1095.

Zen, E.A., 1988. Phase relations of peraluminous granitic rocks and their petrogenetic

implications. Annu. Rev. Earth Planet. Sci. 16, 21–51. https://doi.org/10.1007/s13398-014-0173-7.2.

Chapter 4

Effect of temperature on the densification of silicate melts to lower Earth's mantle conditions

Manuscript under review

Effect of temperature on the densification of silicate melts to lower Earth's mantle conditions

Marija Krstulović[1, 2], Angelika D. Rosa[1], Dario Ferreira Sanchez[3], Lélia Libon[2], Christian Albers[4], Margarita Merkulova[5], Daniel Grolimund[3],Tetsuo Irifune[6], Max Wilke[2]

[1]European Synchrotron Radiation Facility, ESRF, 71 Avenue des Martyrs, 38000 Grenoble, France
[2]University of Potsdam, Institute of Geosciences, Karl-Liebknecht-Str. 24-25, 14476 Potsdam-Golm, Germany
[3]Swiss Light Source, SLS, Paul Scherrer Institut, Forschungsstrasse 111, 5232 Villigen, Switzerland
[4]Technische Universität Dortmund, Department of Physics, Otto-Hahn-Str. 4 44227 Dortmund, Germany
[5]Gent University, Faculty of Sciences, Department of Geology, Pore-scale Processes in Geomaterials Research Group (PProGRess)/UGCT,Ghent University, 9000 Ghent, Belgium
[6]Ehime University Johoku Campus, Geodynamics Research Center, 2-5 Bunky-ocho, Matsuyama, Ehime 790-0826, Japan

(Submitted on 18.03.2021)

Physical properties of silicate melts play a key role for global planetary dynamics, controlling for example volcanic eruption styles, mantle convection and elemental cycling in the deep Earth. They are significantly modified by structural changes at the atomic scale due to external parameters such as pressure and temperature or due to chemistry. Structural rearrangements such as 4- to 6-fold coordination change of Si with increasing depth may influence profoundly melt properties, but have been so far mostly studied at ambient temperature due to the experimental difficulties. In order to investigate the structural properties of silicate melts and their densification mechanisms at the relevant conditions of the deep Earth's interior, we studied haplo basaltic glasses and melts (albite-diopside composition) at high pressure and temperature conditions in resistively and laser-heated diamond anvil cells using X-Ray Absorption Near Edge Structure Spectroscopy. Samples were doped with 10 wt% of Ge, which is accessible with this experimental technique and which commonly serves as an analogue to monitor the network forming cation Si. We acquired spectra on Ge K edge up to 47 GPa and 5000 K and derived average Ge-O coordination number $N_{Ge\text{-}O}$, as well as bond distances $R_{Ge\text{-}O}$ as a function of pressure. Our results demonstrate a continuous transformation from tetrahedral to octahedral coordination between ca. 5 and $\sim$ 30 GPa at ambient temperature. Above 1600 K the data reveal a reduction of the completion pressure of the octahedral coordination by ca. 30 %. The results permit to derive the influence of temperature on the Si coordination changes in natural melts in the Earth's interior. We propose that the complete transition to octahedral coordination is reached in basaltic melts at about 40 GPa, corresponding to a depth of ca. 1200

km in the uppermost lower mantle. At core-mantle boundary (2900 km, 130 GPa, 3000 K) the existence of buoyant melts has been proposed to explain observed low seismic velocity features. Our results highlight that the composition of melt plays a key role for the melt density at such extreme conditions, as it may strongly influence the structural response.

*Corresponding author: krstulov@uni-potsdam.de

4.1 Introduction

Silicate melts have been shaping the evolution of the Earth throughout its history from the early stages of the core formation about 4.5 billions years ago to the present day (Bouhifd et al., 2017). As a part of the largest Earth's reservoir, silicate melts play a crucial role in the planetary dynamics, and understanding of their properties at various thermodynamic settings is thus of fundamental scientific relevance.

Experimental *in-situ* investigations of atomic-scale properties of silicate melts at pressures and temperatures relevant for the deep mantle conditions are very difficult. Therefore, mostly glasses studied at high pressure and ambient temperature have been used as an approximation for the melt properties within the planetary interior (Benmore et al., 2010; Krstulović et al., 2021, 2020; Petitgirard et al., 2019; Sato and Funamori, 2010). While this is a good approximation, the structure of the glasses compressed at room temperature likely differs from the structure of analogue samples compressed at high temperature (Cochain et al., 2015; Ghosh and Karki, 2018, references therein, Pohlenz et al., 2018).

At ambient conditions, structurally silicate melts consists of Si tetrahedra comprised by four oxygen atoms at the tips. These oxygen atoms connect two adjacent tetrahedra and are commonly referred to as bridging oxygens (BOs). If all oxygen atoms are BOs, the interconnected tetrahedra build continuous fully polymerized network. In natural systems, commonly alkali and alkaline earth metals are present, occupying interstitial positions between tetrahedral units. They break the network and reduce the connectivity, generating oxygens that are bonded to only one Si-tetrahedron, so called non-bridging oxygen atoms (NBO). As the number of NBOs per tetrahedron increases, the number of strong bonds reduces, which lowers the degree of polymerization. Aluminum (Al) is another building block in natural melts that can strongly influence the polymerization degree. This is because it can act either as network former providing a framework and rigidity of the glass, or as network modifier, breaking apart the structure through the formation of the NBOs (Allwardt et al., 2003; Krstulović et al., 2021; 2020). Due to high structural and chemical similarity to Si, Ge has been studied extensively as an analogue for Si in the framework of experimental investigation of silicate glasses and melts under compression (Baldini et al., 2010; Hong et al., 2014; Itié et al., 1989). The usage of Ge as an analogue to Si has practical advantages due to its lower pressure of the 4- to 6-fold conversion, and its better accessibility to X-ray spectroscopy techniques.

Under compression the number of oxygen atoms attached to Si (Ge, Al) increases from 4 to 6 and symmetry changes from tetrahedral to octahedral (Baldini et al., 2010; Itié et al., 1989; Williams and Jeanloz, 1988), and concomitantly the number of cations attached to oxygen increases from 2 to 3 (see Krstulović et al., 2021; 2020; O'Keeffe and Hyde, 1981). This increase is extending gradually over a large pressure range (Kono et al., 2014; Krstulović et al., 2021; 2020; Petitgirard et al., 2017; 2019). During the transition tetrahedral and octahedral coordination coexist, whereby with increasing pressure the portion of lower coordinated units decreases, and the fraction of the higher coordinated units increases. This compression behavior is characteristic for all (alumino)silicate and -germanate glasses and melts. However, variations in chemical composition lead to considerable differences in the densification mechanism, as clearly demonstrated in a comparative study on amorphous silicate, anorthite and diopside up to 40 GPa (Williams and Jeanloz, 1988) or as shown in more recent studies on complex aluminogermanate and aluminosilicate glasses (Krstulović et al., 2021; 2020). Williams and Jeanloz (1988) showed that the presence of alkaline earths and particularly of Al considerably shift the structural changes to lower pressure. Krstulović et al. (2021; 2020) revealed differences in the densification mechanism of aluminosilicate (-germanate) glasses compared to

end-member glasses that are especially prominent at pressures above the completion of the octahedral coordination.

A comparative molecular dynamics (MD) study on cold and hot compressed amorphous anorthite reported on delayed structural changes in glasses compared to liquids due to kinetic barrier (Ghosh and Karki, 2018). The study showed also that in the liquid phase the strongest changes around all atoms take place within the first 20 to 30 GPa, further confirmed by other MD studies on molten anorthite and basalt up to megarbar pressures and at about 6000 K (Bajgain et al., 2015; Spera et al., 2009). In a pioneering experimental study on molten basalt compressed up to 60 GPa and at 2200 to ca. 2300 K (Sanloup et al., 2013) structural changes of Si are completed at about 35 GPa, which is a lower pressure compared to what was commonly observed on cold compressed SiO_2 glasses (Benmore et al., 2010; Murakami and Bass, 2010; Petitgirard et al., 2017; Prescher et al., 2017). However, the question whether the observed shift of the structural transformation in molten basalt to lower pressure is related to the increased chemical complexity or the temperature remains open, because room condition data on compressed basaltic glass are not available.

In this work we aim to identify the role of temperature in the densification process of chemically complex silicate glasses. As in our previous works (Krstulović et al., 2021, 2020), we employed X-Ray Absorption Spectroscopy (XAS) coupled to the diamond anvil cell (DAC) to investigate the local structure of glasses and melts at high pressure conditions. Diamond exhibits however, a high absorption of X-ray energies below 10 keV hindering thus studies of low Z-elements such as Si (K edge at 1.8 keV). To circumvent this problematic we doped minor amounts of Ge to partially substitute Si in studied glass. Ge mimics the behavior of network forming cations (Si, Al) and allows to perform XAS measurements in high pressure devices due to its high K edge energy (11.1 keV) (see Krstulović et al., 2020). We report on pressure and temperature induced structural changes of a modified albite-diopside glass probed at pressures up to 47 GPa and to high temperatures up to above 5000 K. Albit-diopside glass represents an analogue for basaltic melts ubiquitous at various depths in the Earth's interior.

Local structural changes in this glass composition have been already characterized previously at high pressure and room temperature using the Extended X-Ray Absorption Fine Structure (EXAFS) signal due to its high sensitivity to bond length variation which can be directly related to coordination number of specific elements (Krstulović et al., 2021, 2020). Application of high temperature leads to non negligible damping of the EXAFS signal, but affects less the XANES region on which present high pressure and temperature study therefore is focused. Our previous findings at ambient temperature and high pressure serve as a reference to deduce the densification mechanism at simultaneous high pressure and temperature from changes in the XANES features. Combining the results with our previous works allowed us to separate the influence of the chemical composition and temperature on the densification mechanism. An important finding of this study is that compression induced structural changes are shifted to lower pressure when temperature exceeds 1600 K. The experimental results of this study and those of our previous works are used to infer the seismic detectability of ultra dense basaltic melts in the Earth's lower mantle.

4.2 Methods

A glass with modified albite-diopside composition and nominal chemical formula $Na_{0.45}Ca_{0.1}Mg_{0.05}Sr_{0.5}Al_{1.35}Si_{1.95}Ge_{0.5}O_{7.8}$ was synthesized from oxide and carbonate powders of SiO_2, Al_2O_3, MgO, Na_2CO_3, $CaCO_3$, $SrCO_3$ and GeO_2 in proper stoichiometric ratios. The

glass was doped with ca. 5000 ppm Y, which will however not be considered here. A ground fraction of the synthesized glass was additionally doped with 2 wt% Fe_2O_3 to allow coupling of the laser. The new mixture was additionally ground for homogenization and shortly molten at 1600 °C. The detailed description of the glass synthesis as well as the concentrations in wt% of the glass without Fe_2O_3 contribution is provided in Krstulović et al. (2021), where it is referred to as AbDi-glass (run 3). The details on the concentrations in wt% of the glass doped by 2 wt% Fe_2O_3 are presented in Table 4.1.

Table 4.1: Measured concentrations in wt% of oxides in AbDi-glass used in run 3

SiO_2	Al_2O_3	MgO	FeO	CaO	Na_2O	SrO	GeO_2	Σ
40.62	22.93	1.11	1.54	1.84	4.25	16.73	10.75	100.05

4.2.1 High pressure and high temperature XAS experiments

Three high pressure and hight temperature XAS experiments in transmission mode were carried out on Ge K edge at different beamlines and synchrotron facilities, including run 1 at the ESRF angle-dispersive XAS beamline BM23, run 2 at angle-dispersive XAS beamline microXAS at SLS and run 3 at energy-dispersive XAS beamline of the ESRF ID24-S. Details about experimental runs and pressure and temperature conditions covered are detailed in Table 4.2.

Table 4.2: Experimental runs - overview

Beamline	P/T	Culet diameter (μm)	Hole diameter (μm)
BM23	2 GPa, $\leq$ 793 K	250	120
	$\leq$ 23 GPa, 773 K	300	150
MicroXAS	$\leq$ 42 GPa, 273 K	300	150
	$\leq$ 47 GPa, 473 K	250	120
	$\leq$ 40 GPa, 673 K	300	150
	$\leq$ 20 GPa, 873 K	250	125
ID24	$\leq$ 37 GPa, 273 K	300	150
	3.5 GPa, $\leq$ 4000 K	400	200
	8 GPa, $\leq$ 5100 K	300	150
	12 GPa, 1600 K	250	125
	16 GPa, $\leq$ 3500 K	300	150
	19 GPa, $\leq$ 3200 K	250	120
	38 GPa, $\leq$ 2000 K	400	200

In all runs membrane driven diamond anvil cells of Le Toullec type were employed to generate high pressures (Le Toullec et al., 1988). The cells were equipped with nano-polycrystalline diamond anvils (Irifune et al., 2003) that provide glitch free spectra (Rosa et al., 2019). The anvils were of Boehler-Almax design (Boehler and de Hantsetters, 2004) with culet diameters ranging from 150 to 300 µm (Table 4.2). Pre-indented Rhenium gaskets to ideal thicknesses were used in all experiments and a hole was drilled by a laser in the center of the indentation that served as a sample chamber (Table 4.2). In all runs the sample chambers were filled entirely with the synthetic glass without pressure transmitting medium, as the gases used could infiltrate and diffuse into the void spaces of the amorphous sample and modify its structural response under compression (Shen et al., 2011).

4.2.2 Resistive heated DAC experiments at BM23 (ESRF) and at microXAS (SLS) beamlines

For experiments at the beamline BM23 (Mathon et al., 2015) the X-ray beam was tuned to the target energy by using a double crystal fixed-exit monochromator equipped with two Si(111) crystals. The beam was focused to 5×5 µm² by two Pt-coated Kirkpatrick-Baez mirrors (KB-mirrors) inclined to 4 mrad. These mirrors served additionally for the rejection of higher order harmonics. Additionally, two Rh-coated mirrors inclined to 3 mrad were employed in front of the KB-mirrors to achieve a higher-order harmonic rejection. Simultaneous transmission acquisitions of the absorption signal of the sample and the reference material (Pt-foil) were conducted by using three ionization chambers filled with appropriate gas mixtures. Collected EXAFS spectra cover the k-range up to 13 Å^{-1}, however, due to low signal to noise ratio above 11 Å^{-1} the data considered for analysis was usually restricted to the XANES domain.

In both experiments homogeneous heating of the sample up to 873 K was achieved using a resistively heating device placed around the diamond anvil cell (RH-DAC) developed at the ESRF sample environment. A K-type thermocouple was placed in contact with the diamond on the transmission side so that the central part of the diamond and the sample chamber remained free for transmission XAS measurements. Due to the high thermal conductivity of diamond the temperature read at this position corresponds closely to the sample temperature. This was verified in a calibration run based on the melting of a $NaNO_3$ crystal that revealed a temperature offset of 0.3°C at 303.2°C. In both RH-DAC runs the pressure was determined at high temperature from the lattice parameter of Au obtained from X-Ray Diffraction (XRD) on a small pellet of Au powder placed near the gasket rim, the well characterized thermal equation of state of Au (Matsui, 2010) and the temperature measured from the thermocouple (details about the resistive heating apparatus will be presented in a future publication). For XRD measurements, a MarCCD 165 diffraction detector was installed in the beamline placed 160 mm from the sample and the beam was tuned to an energy of 18 keV corresponding to a wavelength of 0.6888 Å. Detector to sample distance, detector tilt and rotation parameters were obtained from a standard measurement of a CeO_2 and LaB_6 powder at BM23 and MicroXAS, respectively. Diffraction data were acquired without sample oscillation and with an exposure time of 60 seconds before and after the acquisition of the XAS data. In both experiments Fe-free glass (see Krstulović et al., 2021) was used.

4.2.3 Laser-heated DAC experiments at ID24-S (ESRF)

For high-pressure experiments at temperatures above $\sim$ 900 K, laser heated DAC experiments (LH-DAC) were conducted at the S-branch of the ID24 beamline (Kantor et al., 2018; Pascarelli et al., 2016) due to its suitability to perform LH-DAC measurements coupled to micro-focused X-ray beams and fast detection techniques. The beam energy was tuned to the Ge K edge using two U32 undulators closed to a gap of $\sim$ 14.6 mm providing an energy range over 1000 eV above the edge. Fine vertical focusing was achieved using a set of two silicon coated horizontal mirrors inclined to 4 mrad. Fine horizontal focusing on the sample was achieved by an elliptically bent Si(111) polychromator crystal. A Hamamatsu camera equipped with an energy-position sensitive chip was used to acquire the signal behind the sample (I1). The beam intensity before the sample (I0) was taken shortly before and after I1 and outside the diamond anvil cell, as the sample chamber was entirely filled with the sample (without pressure transmitting medium). At the 11.2 keV the smallest focusing of 4.8×4.8 µm^2 at the Ge K edge was only achieved in a restricted energy range of about 150 eV because beam

penetration into the banded polychromator crystal becomes significant at this energy, resulting in a higher spatial and energy spread of the diffracted beam and thus to the formation of tails. In the present experiment we therefore acquired only XANES data. An integration time of 4 ms for XAS acquisitions was sufficient to obtain high-quality XANES data during the heating runs due to the high photon flux at ID24.

Similar to run 1 and 2, in run 3 high pressure in the sample was reached by increasing the membrane pressure in DAC equipped with nano-polycrystalline diamonds of the Le Toullec type. The sample was loaded in a small hole (see Table 4.2) drilled in the Re-gasket. A micrometric ruby crystal was loaded into the sample chamber close to the rim of the Re-gasket. The pressure in the sample was accurately determined before and after each heating run from the shift of the ruby fluorescence peak, excited by a green laser. For the pressure calculation the non-hydrostatic ruby pressure scale was used (Mao et al., 1978). The sample was heated using two infrared 120WNd:YAG fiber-coupled lasers (1064 nm wavelength) that were focused onto the sample using lenses with a focal distance of 50 mm. The sample was heated from both sides in order to reduce axial temperature gradient in the sample. The laser beams enter the sample with an angle of 30 degrees with respect to the direction normal to the sample allowing the generation of large (20-30 µm) heating spots, ensuring a flat temperature profile in the central hot-spot region that was probed by the 5 times smaller X-ray beam. The temperature in the central portion of the hot-spot was determined *in-situ* from spectral radiometry and by collecting the emitted light from the sample using a set of optical lenses. For this experimental run the glass was doped with Fe_2O_3 to ensure coupling of the YAG laser with the sample and a homogeneous heating. Because in this work Fe was used for purely experimental purposes, both, Fe-free, and Fe doped glass will be here after referred to as AbDi-glass.

4.2.4 XAS data analysis

All spectra were analyzed by the software package XAFS (Winterer, 1997). The pre-edge background was subtracted by fitting a polynomial function to the signal below the edge between 11015 and 11080 eV. Subsequently the spectra were normalized to the Ge K edge combining a Gaussian and an Error function to the edge position (E_0). The present study focuses mostly on the XANES part of the signal because of the temperature induced high signal to noise ratio in the EXAFS part.

Only in experiment at BM23 conducted at 773 K up to 23 GPa the EXAFS data were of sufficiently high quality for further analysis. For this purpose, normalized spectra were converted from energy into the k-space χ(k). After conversion the background in the post-edge region was subtracted using a smoothing spline function with 8 knots extending from 0 to 10.7 Å^{-1}. For the EXAFS analysis the extended absorption spectra were fitted in k-space using unfiltered data. The k^3 weighted Ge spectra were Fourier transformed without phase-shift correction using a Kaiser-Bessel window. The signal used for analysis covers the range from 3 to 10.4 Å^{-1}. To calculate the backscattering amplitude and the phase-shift, as well as the photo-electron mean free path, a FEFF9 code was used (Rehr et al., 2010). We fitted Ge K edge EXAFS data using Ge-O model only in tetrahedral coordination for the first (Ge-O) coordination shell and for all pressure points, because the introduction of additional scattering paths did not considerably change the fit results. An asymmetric pair distribution function (PDF) was used to reduce the anharmonic effects (Pohlenz et al., 2018, Winterer, 1997). Free fit parameters were first shell mean bond distance $R_{\text{Ge-O}}$, first shell coordination number parameter $N_{\text{Ge-O}}$, the bond distance variance or the EXAFS or the Debye-Waller Factor $\sigma^2_{\text{Ge-O}}$ and the energy mismatch between the experimental and theoretical energy scales ΔE_0,

which is a non-structural parameter. Only the asymmetry parameter $h_{\text{Ge-O}}$ was treated as a fixed parameter. The values of the asymmetry parameter were changed manually for each pressure step with increasing h values until the best fit for each pressure point was reached. The quality of the fit was derived mainly from the χ^2 statistics. The non-structural parameter, amplitude reduction factor S_0^2 was set to 1.

4.3 Results

In studied AbDi-glass the data set collected in the pressure range up to 23 GPa and at 773 K provided sufficiently good EXAFS signals. The main results of the EXAFS analysis are presented in FIG. 4.1. In the k^3-weighted EXAFS function the fitted k-range extends from 3 to 10.4 Å^{-1} (FIG. 4.1A). The oscillations at 2.5 Å^{-1} broaden as the pressure increases, which is particularly visible above ca. 8 GPa. At about 4.5 Å^{-1} and above, the oscillations do not considerably change their shape and position under compression. Above $\sim$ 7 Å^{-1} the spectra become noisy, but are still sufficiently well defined, which is why larger fit window was considered for the data analysis. The Fourier Transform magnitudes (FT) of the EXAFS functions have the main peak at about 1.3 Å, which corresponds to signal coming from the first coordination shell (FIG. 4.1B). This peak shows a low magnitude and a significant broadening that increases in the pressure range between 10 and 20 GPa. Its intensity is rather constant under compression, except for the highest probed pressure of 23 GPa. The position of the main peak is virtually constant along R-values (here R corresponds to inter-atomic distances uncorrected for phase shift). The signals beyond the first peak of the FT can not be clearly resolved. From the parametrization of the EXAFS functions, the numerical values of the fitted Ge-O bond distances under compression were extracted and are presented in FIG. 4.1C as black squares. The inter-atomic distances continuously increase at pressures above 6.6 GPa up to the highest probed pressure of 23 GPa. The data are additionally compared to the Ge-O bond distances obtained under compression at room temperature, shown as orange circles (Krstulović et al., 2021). Both data sets follow very similar pressure trend.

Except for the presented data set at 773 K, other data acquired on the Ge K edge within the three experimental runs were restricted to the XANES region. In FIG. 4.2 the pressure evolution of normalized Ge K edge XANES spectra of AbDi-glass acquired at room temperature in run 2 (left) and run 3 (right) are shown. In both runs the first XANES peak maximum (FXPM) continuously shifts to higher energy values with increasing pressure, with overall ΔFXPM = 1.8 eV and 1.9 eV in run 2 and 3, respectively, indicated by two vertical lines in the left and right upper plot, respectively. In order to better resolve spectral variations under compression we calculated differential spectra by subtracting the XANES spectra acquired at the lowest pressure from those at high pressure (FIG. 4.2B, FIG. 4.2D). XANES spectra exhibit significant changes in three distinct regions, referred to as A, B and C in FIG. 4.2D. The region A reflects changes in the edge at about 11113 eV. As the pressure increases, the edge moves continuously to higher energies. Region B covers the variations of the first XANES peak and its maximum (FXP(M)) under compression between 11113 at 11123 eV and reveals a systematic intensity increase and broadening with pressure. In both run 2 and 3 we observed the strongest intensity increase of the main FXPM in a similar pressure range, between 5 and 23 GPa in run 2 (FIG. 4.2B) and between 6 and 24 GPa in run 3 (FIG. 4.2D). The shoulder after the FXP located between 11120 and 11140 eV is referred to as C (FIG. 4.2D). We observed a continuous intensity reduction of the FXP shoulder with pressure which is consistent with the variations observed in the edge region (A) and with the FXP(M) (B).

Normalized Ge K edge XANES spectra of AbDi-glass and corresponding difference

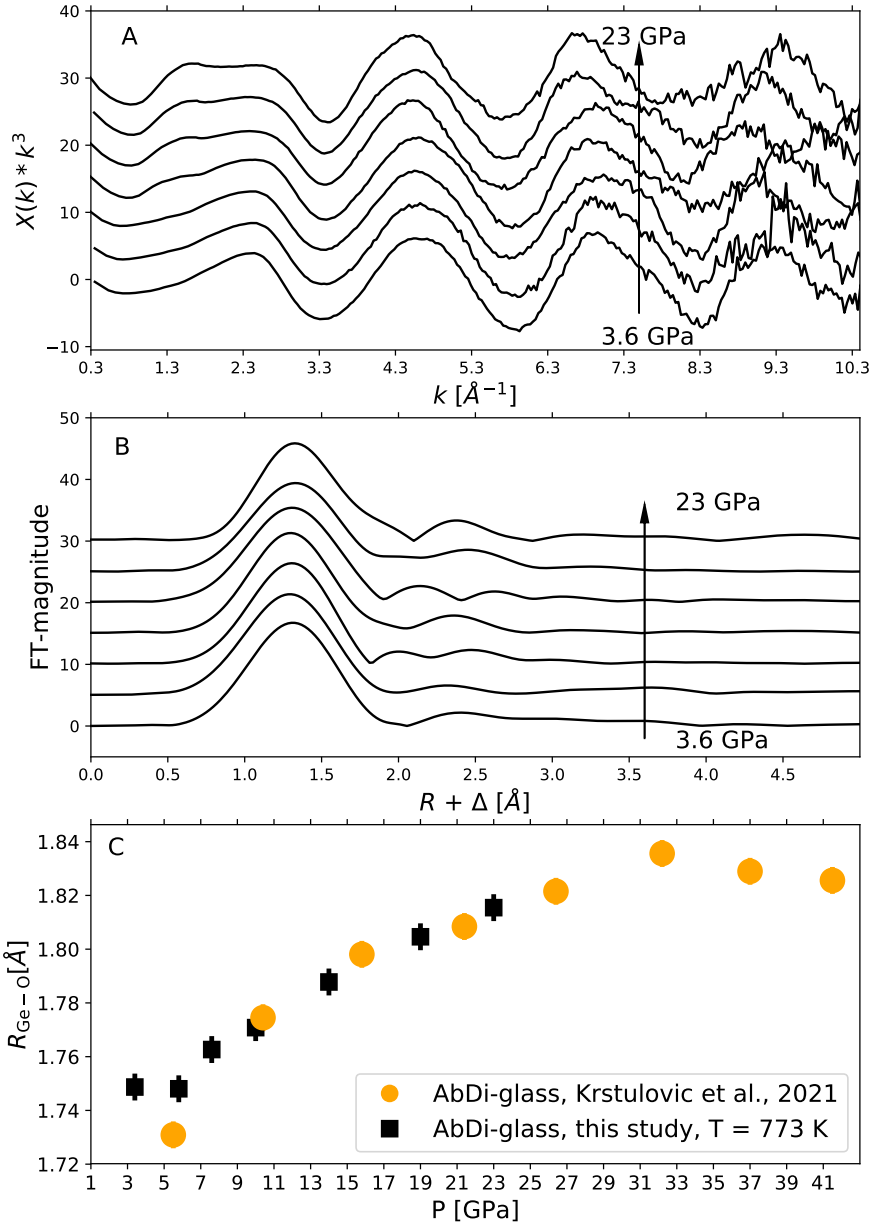

Figure 4.1: Evolution of k^3 weighted EXAFS spectra at the Ge K edge of AbDi-glass as a function of pressure up to 23 GPa and at constant temperature of 773 K (A). Magnitude of the Fourier Transforms of the EXAFS functions shown in A (B). Plotted magnitudes are not corrected for the phase-shift. Evolution of the average Ge-O bond distances of the first coordination shell $R_{\text{Ge-O}}$ of AbDi-glass with increasing pressure up to 23 GPa and at 773 K (black squares) compared to AbDi-glass under compression at room temperature shown as yellow circles (Krstulović et al., 2021) (C).

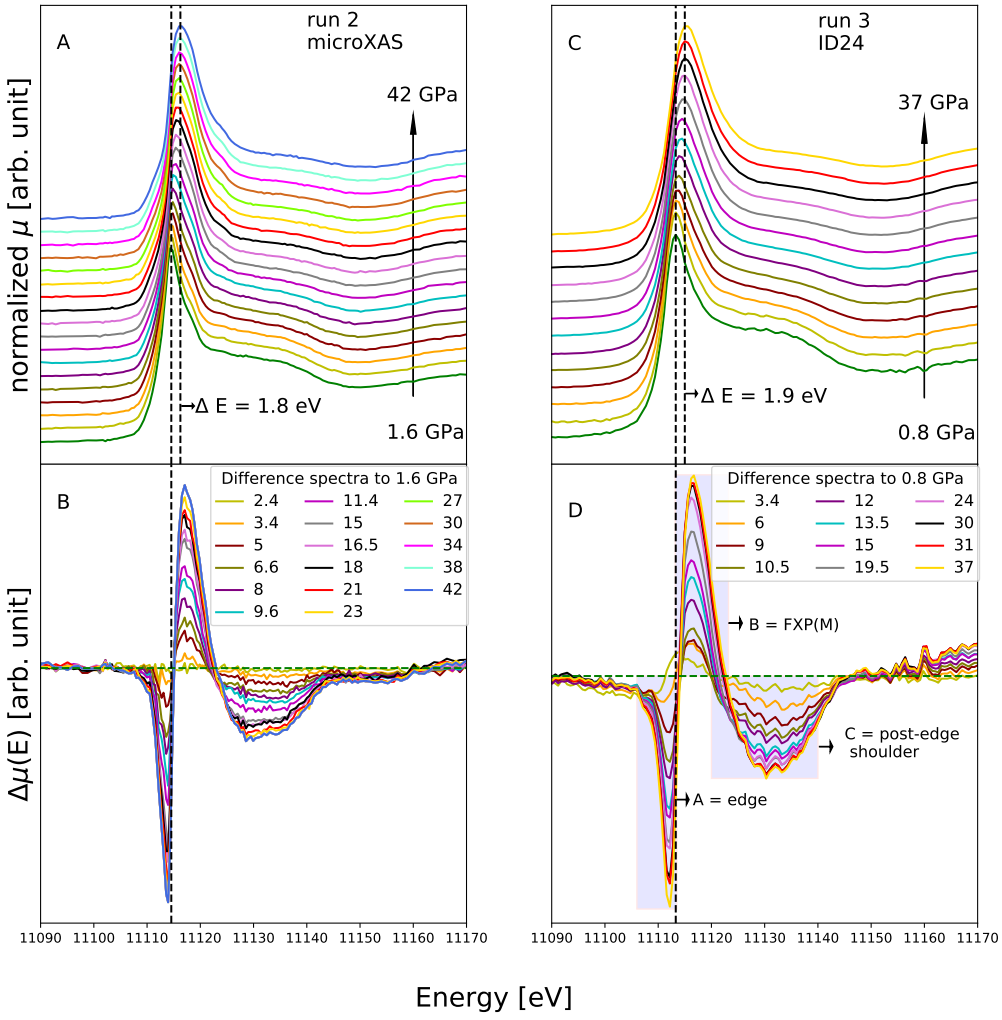

Figure 4.2: Normalized Ge K edge XANES spectra of AbDi-glass under compression up to 42 and 37 GPa and at room temperature of the data acquired in run 2 and 3 (FIG. 4.2A, FIG. 4.2C, respectively). Two vertical lines in FIG. 4.2A, as well as in 4.2C show the shift of the energy point of the FXMP between the lowest and the highest probed pressure. The differences of the XANES spectra at high pressure to the spectrum at the lowest probed pressure are presented in FIG. 4.2B and FIG. 4.2D. In FIG. 4.2D three spectral features are highlighted as example. The feature referred to as A shows the changes of the edge. The feature referred to as B highlights the variations of the first XANES peak and its maximum, FXP(M) under compression, and C shows the changes of the post-edge shoulder that emerges between $\sim$ 11120 and 11140 eV.

spectra of the data collected at simultaneous high pressure and temperature conditions up to 873 K and 47 GPa in the RH-DAC experiments in run 1 and 2 (see Table 4.2) are presented in the Figures 5.1 - 5.5 of the supplemental information (SI). Normalized spectra acquired during laser-heating, run 3 (see Table 4.2) up to 5000 K and 38 GPa are presented in the Figures 5.6 - 5.9 of the SI. XANES spectra acquired in the isothermal runs at 473, 673, 773 and 873 K (FIG. 5.2 - 5.5) follow similar trends with pressure as those acquired at room temperature (FIG.4.2). In order to correlate local structural changes observed in the XANES during the isobaric high temperature laser-heating runs to those observed during cold compression, we compiled spectra acquired at similar temperatures of 273, 1600, 2000 and 4000 K and various pressures (FIG. 4.3). At all elevated temperatures, we observe similar spectral changes as already observed at room temperature condition in FIG. 4.2 in the three different regions of the XANES. On the other side, at isobaric conditions with increasing temperature the energy position of the edge shows no shift to higher energies, but rather to the lower, as we can see in FIG. 5.1 (2 GPa, $\leq$ 773 K), as well as in FIG. 5.6 - 5.9 (see SI) at temperatures above 1700 K and at various isobaric settings.

FIG. 4.4 reports the relative shift of the energy point of the FXPM at high pressure to the point at ambient pressure (ΔFXPM) as a function of pressure for the spectra collected at different temperature regimes. In the upper plot the data on AbDi-glass from this study and from Krstulović et al., 2021 and on amorphous $NaAlGe_3O_8$ (Krstulović et al., 2020) collected at room temperature, are plotted together with the data collected within RH-DAC experiments at temperatures up to 873 K (FIG. 4.4A). In the bottom plot the data collected within the LH-DAC experiment that cover temperatures $\geq$ 1600 K are compared to one of the data sets collected at the lower temperature regime (FIG 4.4B). All data follow very consistent pressure dependent shift of the FXPM with the steepest increase in the pressure range up to about 25 GPa. At higher pressures the FXPM still slightly shifts to higher energy values, but its trend is less steep. The data collected at temperatures of 1600 K and above have steeper pressure trend up to about 20 GPa and more dramatic flattening of the pressure trend above 20 GPa compared to the data at lower temperatures (FIG. 4.4B). The pressure dependent evolution of the FXPM correlates well with the relative changes of the integrated area of the B-peak (shown as an example in FIG. 4.2D) as a function of pressure and at various temperatures (FIG. 4.5). The energy range of 10 eV under the B-peak in all considered data sets was taken for the integration.

From the relative shift of the energy point of the FXPM (FIG. 4.4) we derived the coordination number $N_{\text{Ge-O}}$, shown in FIG. 4.6. In order to correlate our observations on XANES feature variations to structural parameters such as coordination number, we used our previous results obtained from EXAFS analysis of amorphous $NaAlGe_3O_8$ (Krstulović et al., 2020) compressed at room temperature. The study on $NaAlGe_3O_8$ glass provided very accurate EXAFS fit parameter values along the entire probed pressure range including also values at very low pressure, as well as very reliable data for the FXPM shift (Krstulović et al., 2020). Therefore the results on $NaAlGe_3O_8$ were used rather than previously studied AbDi-glass (Krstulović et al., 2021). For the data calibration, we first established the linear relationship between the average Ge-O bond distances $R_{\text{Ge-O}}$ and (ΔFXPM) determined for the same spectra of amorphous $NaAlGe_3O_8$ (Krstulović et al., 2020). This linear calibration is shown in FIG. 4.6A. It shows the change of the Ge-O bond distances as a function of the FXPM shift up to the distance where octahedral coordination is reached (1.821 Å). At higher pressure, the maximum of the FXP still shifts but is only associated to further compression of the Ge-O polyhedron. The change in the color indicates the change of the Ge-O coordination number that follows from the relationship between ΔFXPM and $R_{\text{Ge-O}}$ as indicated in the color map. The critical value of the shift of FXPM where the octahedral coordination number is reached is 1.86 eV.

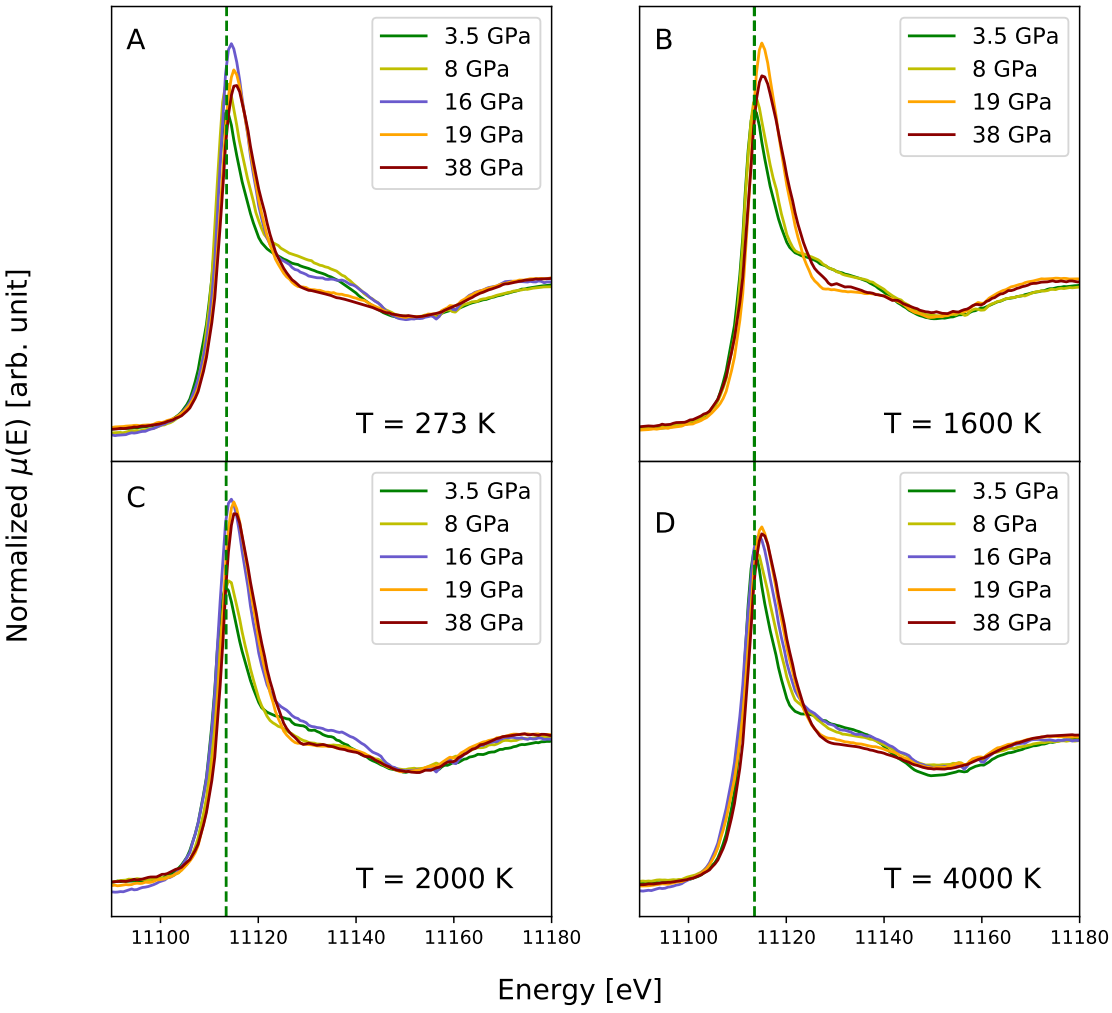

Figure 4.3: Normalized Ge K edge XANES spectra of AbDi-glass as a function of increasing pressure up to 38 GPa and at constant temperatures of 273 K (A), 1600 K (B), 2000 K (C) and 4000 K (D). The vertical green dashed line indicates the position of the main XANES peak at 3.5 GPa.

The coordination number values calculated from the ΔFXPM for the data collected up to 38 GPa and 4000 K are shown in FIG. 4.6B. Light blue circles show coordination number values up to 4.3, black circles between 4.4 and 5.7, and pink circles extracted coordination number values above 5.7 (FIG. 4.6B).

4.4 Discussion

Major objective of this work was to constrain the role of the temperature in the process of the pressure induced structural changes in basaltic melts. For this we probed the local structure of Ge doped as a minor element in silicate glasses with albite-diopside quasi-eutectic binary composition using *in-situ* high-pressure and high-temperature XAS. Ge was used as a structural analogue for Si, which is a major component of the natural melts, but is not accessible using X-ray spectroscopy. Within three experiments we explored the structural evolution of Ge in multiple pressure and temperature settings with the pressure extending up to maximum 48 GPa and with temperatures extending up to ca. 5000 K. The analyzed data imply that the strongest structural variations occur within the first $\sim$ 30 GPa, depending on the temperature. This is primarily indicated by a strong shift of the FXPM in this pressure range (FIG. 4.4). The shift of the energy point of the FXPM, ΔFXPM, is a reliable marker for the structural changes extracted from XANES data. The observations on the shift of the FXPM are supported by the relative change of the peak area integral of the difference spectra of the normalized XANES spectra (FIG. 4.5). These two parameters, both gained from the normalized XANES spectra, provide a rough orientation about the changes in the structure. However, they do not provide direct numerical values of the physical parameters, which describe structural properties of the system, such as the coordination number. In order to deduce the local coordination environment in this chemically complex compound from experimentally gained data, we used the sensitivity of the energy position of the white line to the local coordination environment to derive the coordination number values of Ge K edge of AbDi-glass under compression at different temperature regimes. Based on the calculated values, Ge-O coordination number $N_{\text{Ge-O}}$, mapped in the pressure-temperature diagram (FIG. 4.6B) suggests that temperatures up to 900 K have no visible influence on the structural changes under compression. In all data sets studied in this temperature interval the coordination number increases gradually from 4 to 6 with the completion of the octahedral coordination number somewhere between 25 and 30 GPa (FIG. 4.6B). The XANES analysis for runs up to temperatures of 900 K is supported by EXAFS data studied at 773 K up to 23 GPa (FIG. 4.1C), where the extracted Ge-O bond distances continuously increase within the probed pressure range, indicating that the coordination number 6 is not reached up to 23 GPa. At temperatures of $\sim$ 1600 K and above structural changes are shifted to lower pressure. At these temperatures both the onset of the structural transformations and the completion of the octahedral coordination are shifted to lower pressure, and the completion is reached already at 20 GPa. This corresponds to a shift of about 30 % to lower pressure compared to the values determined for the data collected at lower temperatures. The onset of the structural transformations is much less affected by high temperatures, so that at above 1600 K a shift of maximum 15 % to lower pressure can be accounted for.

The fact that up to 900 K no effect is observed indicates that the sample is still in the solid glassy state and even elevated temperature provides no kinetic enhancement of the transformation. Using the viscosity model of Giordano et al. (2008) the glass transition temperature is estimated at ca. 1000 K (i.e. viscosity = 10^{12} Pa s), which supports this explanation. Further, thermal expansion may counteract the structural transformation, leading

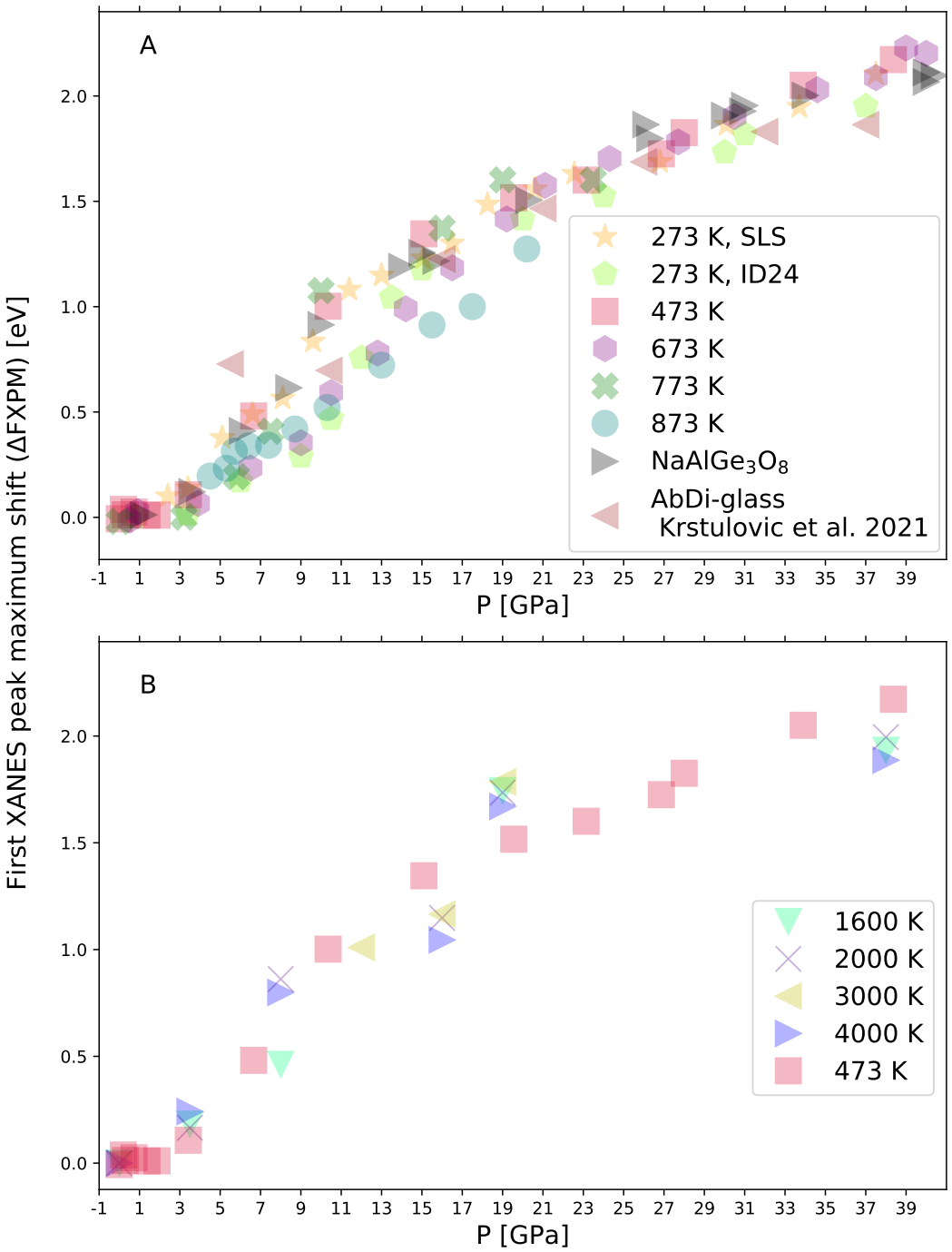

Figure 4.4: Energy shift of the fitted FXPM of Ge K edge of AbDi-glass as a function of increasing pressure at room temperature in run 2 and run 3, as well as in AbDi-glass (Krstulović et al., 2021) and in $NaAlGe_3O_8$ (Krstulović et al., 2020), and at high temperatures up to 873 K (A). Energy shift of the fitted FXPM of Ge K edge of AbDi-glass as a function of increasing pressure at very high temperatures of $\geq$ 1600 K plotted together with the data set acquired at 473 K for comparison (B).

to a non-detectable effect of the temperature on the coordination transformation in the glass. Compressing the undercooled liquid at T > 1000 K could possibly show a shift of the transformation to lower pressure. However, this T-range was not accessible with our apparatus. In the runs using laser heating with higher temperature, the molten state is probed, and thus, the onset and the progress of the structural changes are shifted to lower pressure.

The effect of the thermal expansion on the studied melt can be demonstrated by the intensity variations of the white line at constant pressure and increasing temperature (see FIG. 5.6 - 5.9). The data show that at 3.5 and 8 GPa with increasing temperature the peak intensity of the white line continuously decreases at all temperatures $\geq$ 1600 K (FIG. 5.6, 5.7). At higher pressures of 19 and 38 GPa, the intensity of the white line first increases at temperatures up to about 1700 K. Between 1700 and 3000 K the intensity is rather constant, whereas only above 3000, and particularly above 4000 K the intensity shrinks (FIG. 5.8, 5.9). The behavior of the white line intensity can be explained in the light of the effect of the thermal expansion in relation to coordination symmetry. It has been previously reported that for four-fold coordinated cations thermal expansion has a strong effect, whereas it plays negligible role for six-fold coordinated species (Nemausat et al., 2017). The authors of the study relate this to symmetry differences between four- and six-fold coordinated cations. In octahedra bond lengths are longer than in tetrahedra, which gives more freedom to the six-fold coordinated cations (Nemausat et al., 2017). If we use this as a guideline for the deduction of the local coordination environment of Ge at various pressure and temperature constellations, we can attribute the constant reduction of the peak intensity with increasing temperature at 3.5 and 8 GPa to tetrahedral coordination of Ge in the melt. On the other side, the absence of this reduction at temperatures lower than 3000 K at 19 and 38 GPa might suggest that Ge in the melt at these pressures is already octahedraly coordinated, and that much higher temperatures are required to promote the effect of thermal expansion. While this scenario is possible, it is worth considering the possibility that at high pressures (e.g. $\geq$ 19 GPa) the material might crystallize at temperatures below $\sim$ 2000 K, which would cause the intensity increase of the white line, as well, due to increase in ordering. As crystallization will likely happen without coordination change at a given pressure, the line position is not affected and would not change the picture in FIG. 4.6.

4.5 Implications

4.5.1 Si coordination in lower mantle melts

Considering the results of this work on Ge, and keeping in mind previously reported structural behavior of Si in molten basalt and anorthite (Ghosh and Karki, 2018; Sanloup et al., 2013), we will elaborate the structural behavior of Si in aluminosilicate melts as a function of pressure and temperature in the following. According to both mentioned studies, six-fold coordination of Si is completed at about 30 to maximum 35 GPa (Ghosh and Karki, 2018; Sanloup et al., 2013). In cold compressed SiO_2 glass a variety of pressures of the completion of the octahedral coordination number has been reported (Benmore et al., 2010; Murakami and Bass, 2010; Petitgirard et al., 2017; Prescher et al., 2017; Sato and Funamori, 2010). However, several studies, including more recent ones provide more robust evidence for the completion of the octahedral coordination number of Si in SiO_2 glass at about 50 or 60 GPa (Murakami and Bass, 2010; Petitgirard et al., 2017; Prescher et al., 2017), which is at considerably higher pressure compared to observations made on molten basalt and anorthite. If we assume that at temperatures of the stable melt the transition is at pressures that are up to about 30% lower,

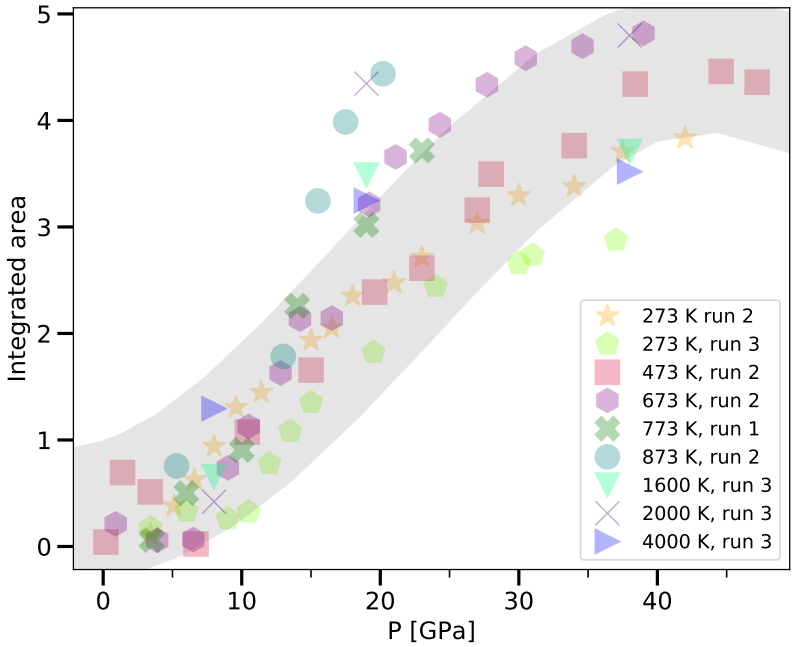

Figure 4.5: Integrated area expressed in absolute values of the B-peak (shown as an example in FIG. 4.2D) of the difference spectra of the normalized Ge K edge XANES spectra of AbDi-glass as a function of increasing pressure at various temperature regimes. The energy range of 10 eV under the B-peak was taken for the integration.

even for SiO_2 melt a transition to 6-fold coordination can be expected at about 45 GPa latest. This estimate is strongly supported by the latest determination of the melting curve of SiO_2 (Andrault et al. 2020) which shows a considerable change in slope at 40 GPa (see FIG.4.7), separating the low density melt from the high density melt. This is still higher than for the basaltic system (Sanloup et al., 2013) but the difference can be related to compositional effects (Krstulović et al. 2021; Williams Jeanloz 1988).

In this sense, the pressure of the completion of the six-fold coordinated Si, reported by Ghosh and Karki (2018) and Sanloup et al. (2013) is supported by the observed shift of ca. 30 % in hot compressed AbDi-melt compared to the glass compressed at lower and ambient temperature. Overall, we could expect that Si in natural silicate melts in the Earth should reach full octahedral coordination at about 40 GPa, which corresponds to the upper lower mantle conditions roughly at about 1200 km depth (see FIG. 4.7). Because at low pressure our data support lower influence of the temperature on the onset of the structural transformations (maximum 15 %), based on previous reports on cold compressed SiO_2 (Murakami et al., 2010; Petitgirard et al., 2019; Prescher et al., 2017), we can propose that in natural melts this occurs at latest at 15 GPa. A schematic comparison of the structural evolution in SiO_2 glass and aluminosilicate melts can be found in FIG.4.7.

Regarding the question about the existence of a high density basaltic melt at the bottom of the mantle, Krstulović et al. (2021) provided an evidence that in cold compressed AbDi-glass at pressures above ca. 30 GPa the glass experiences a strong volume reduction, which can be deduced from the dramatic reduction of the average Ge-O bond lengths at very high pressures. This is a strong indicator that in studied cold compressed glass primarily alkali, alkaline earths and Al are responsible for the strong compressibility, inhibiting further structural transformations of Si beyond octahedral coordination. FeO will behave structurally in a similar

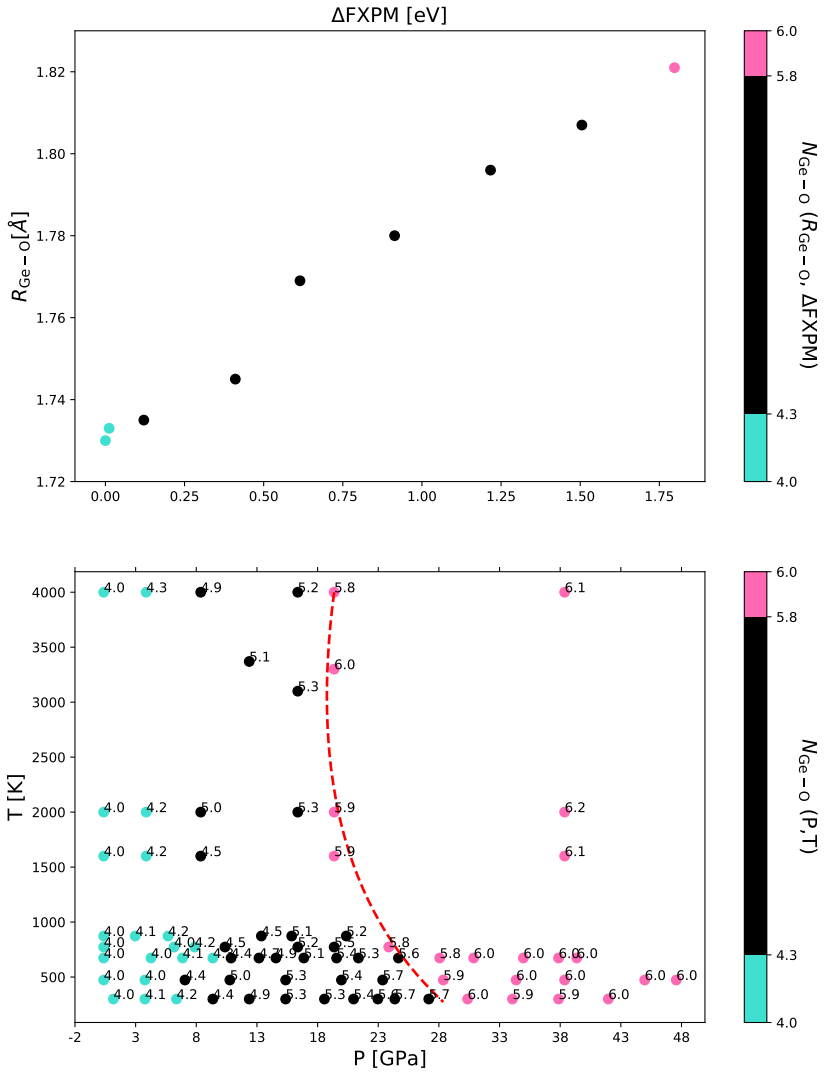

Figure 4.6: Relationship between the Ge-O bond distances and ΔFXPM of amorphous $NaAlGe_3O_8$ (Krstulović et al., 2020), which was used as a calibration for the derivation of the Ge-O coordination number in this study. The coordination number values resulting from the FXPM shift show change from 4 (light blue) to 6 (pink). Black circles correspond to the values in the intermediate range (top plot). First shell Ge-O coordination number evolution ($N_{\text{Ge-O}}$) of Ge K edge of AbDi-glass as a function of pressure and temperature derived from the XANES spectra of this work (bottom plot). The pressure range extends up to maximum 48 GPa, whereas the covered temperature range extends up to 4000 K. Light blue circles cover coordination number up to 4.3, black the range between 4.4 and 5.7 coordination number, and pink circles the coordination number 5.8 and higher, with 6 as a maximum coordination number. Red dashed curve indicates the pressure of the completion of the octahedral coordination at different temperatures. At $\geq$ 1600 K errors in temperatures of at least 100 to 200 K should be considered.

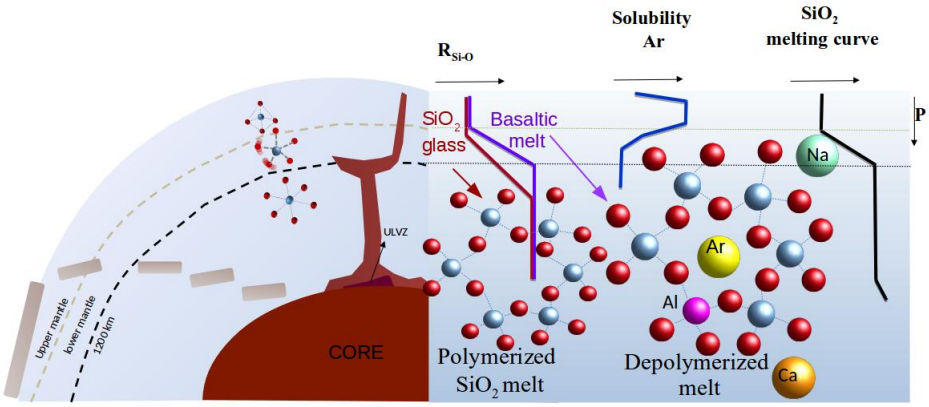

Figure 4.7: Conceptual sketch of the Earth's interior highlighting discussed physical and chemical processes. On the left side the Earth's interior, subdivided on two large media - mantle (blue) and core (red), is schematically presented with subducted oceanic lithosphere (grey), mantle plumes (orange), and the ultra-low velocity zone, ULVZ located at the root of the plume (dark red). The boundaries between upper and lower mantle, as well as the depth of 1200 km are marked with dashed lines crossing along the entire cartoon. The right side of the plot shows the evolution of the Si-O coordination number $N_{\text{Si-O}}$ as a function of depth (pressure) in fully polymerized SiO_2 glass (e.g. Petitgirard et al, 2019) and in depolymerized basaltic melts (derived based on this work) shown as red and purple lines, respectively, as well as the structures of corresponding compounds. Blue line presents the solubility of Ar in silicate melts (Bouhifd and Jephcoat, 2006) as a function of pressure (depth), and green line the melting curve of SiO_2 (Andrault et al., 2014).

manner, and it has a strong effect on the melt density (e.g. Lange and Carmichael, 1987). Thus possible high density melts are mainly chemically induced. It has been previously reported that subducted basaltic oceanic lithosphere has much larger density than the surrounding pyrolite (Ringwood, 1982). Higher density allows the subducted basaltic oceanic slab to reach depths of about 700 km (Ringwood, 1982, references therein). In more recent works it has been proposed that subducted MORB lithosphere can even reach the CMB (Andrault et al., 2014; references therein; Pradhan et al., 2015). This scenario is supported by observed high polyhedral compressibility of AbDi-glass in Krstulović et al. (2021). The question about its partial melting at considered conditions remains open. According to Andrault et al. (2014), melting of basalt at CMB conditions occurs around 3800 K, which is 350 K below the mantle solidus (Andrault et al., 2014). Pradhan et al. (2015) reported that higher temperatures of at least 4000 K are needed for partial melting of MORB at the CMB. Both temperatures are higher than the usually reported temperature at the CMB (3570 - 3750 K) (see for details Pradhan et al., 2015, references therein). Recently even higher CMB temperature could be suggested from melting curves of Fe (Anzellini et al., 2013; Morard et al., 2017). The present literature data do not allow to conclude whether basalt can reach partial melting at the CMB or not. However, its overall lower melting temperature compared to the pyrolitic one, makes it a good candidate for the explanation of the origin of the partial melts at the CMB region and our structural considerations would support this compositional estimate.

4.5.2 Transport of noble gases in the deep mantle

Noble gases exhibit high solubilities in silicate melts (up to wt.%) at pressures below 15 GPa corresponding to the upper mantle (Bouhifd and Jephcoat, 2006; Bouhifd et al., 2020). At these conditions, silicate melts have open sixfold tetrahedral ring structures in which inert volatiles and molecules may be easily incorporated. Beyond this pressure, noble gases show a drastic reduction of their solubility in silicate melts, which has been ascribed to the collapse of the 6-fold tetrahedral rings due to the densification mechanism of silicate melts (Bouhifd and Jephcoat, 2006). Due to this incorporation mechanism, the highest solubilities are observed for polymerized silica-rich compositions while basaltic melts exhibit lower solubility. Our results suggest that there will be a drastic further reduction at the on-set of the 4-6 fold coordination change if there is no other incorporation mechanism active in dense silicate melts at extreme pressure, where the melt consists of a closely packed structure of oxygen. The high partition coefficients between metallic and silicate melt determined at high pressure (Bouhifd et al. 2013, 2020) corroborate this speculation, which should be constrained by data at > 20 GPa. Thus, the structural properties of melts at lower mantle conditions may considerably affect the overall noble gas budget and all associated isotope signatures of the whole mantle. This finding may be similarly important for halogens and other volatile species that enter in the same site.

Acknowledgements

We thank the entire staff of the beamline BM23 of the European Synchrotron Radiation Facility (ESRF), in particular S. Pascarelli and O. Mathon, for providing us two experimental sessions to perform the experiment. We strongly recognize the technical support provided by F. Perrin and S. Pasternak. We are particularly grateful for the support provided by J. Jacobs from the high-pressure sample environment group of the ESRF for his assistance with high-pressure instrumentation, and R. Torchio for providing the measurements on reference samples. We further thank B. Meyer from microXAS beamline of the Paul Scherrer Institute (PSI), for technical support during the experiment and Toru Shinmei from GRC for the synthesis of the nano-polycrystalline diamonds. We highly acknowledge Christina Günter (Institute of Geosciences, University of Potsdam) for the chemical analysis of the samples (Electron microprobe analysis) as well as Rico Fuchs for help during the sample synthesis. We also thank H. P. Nabein from German Research Centre for Geosciences (GFZ) for checking the amorphous nature of the synthesized glasses using XRD. M.W. would like to acknowledge funding by Deutsche Forschungsgemeinschaft (DFG) through Project Wi 2000/13-1.

Allwardt, J. R., Lee, S. K., Stebbins, J. F. (2003). Bonding preferences of non-bridging O atoms: Evidence from 17O MAS and 3QMAS NMR on calcium aluminate and low-silica Ca-aluminosilicate glasses. American Mineralogist, 88(7), 949–954. https://doi.org/10.2138/am-2003-0701

Andrault, D., Morard, G., Garbarino, G., Mezouar, M., Bouhifd, M. A., Kawamoto, T. (2020). Melting behavior of SiO_2 up to 120 GPa. Physics and Chemistry of Minerals, 47(2). https://doi.org/10.1007/s00269-019-01077-3

Andrault, D., Pesce, G., Bouhifd, M.A., Bolfan-Casanova, N., Heńot, J.M., Mezouar, M. (2014). Melting of subducted basalt at the core-mantle boundary. Science 344 (6186), 892–895. https://doi.org/10.1126/science.1250466

Anzellini, S., Dewaele, A., Mezouar, M., Loubeyre, P., Morard, G., (2013). Melting of iron at earth's inner core boundary based on fast X-ray diffraction. Science, 340(6131), 464–466. https://doi.org/10.1126/science.1233514

Bajgain, S., Ghosh, D. B., Karki, B. B. (2015). Structure and density of basaltic melts at mantle conditions from first-principles simulations. Nature Communications, 6. https://doi.org/10.1038/ncomms9578

Baldini, M., Aquilanti, G., Mao, H. K., Yang, W., Shen, G., Pascarelli, S., Mao, W. L. (2010). High-pressure EXAFS study of vitreous GeO_2 up to 44 GPa. Physical Review B - Condensed Matter and Materials Physics, 81(2). https://doi.org/10.1103/PhysRevB.81.024201

Benmore, C. J., Soignard, E., Amin, S. A., Guthrie, M., Shastri, S. D., Lee, P. L., Yarger, J. L. (2010). Structural and topological changes in silica glass at pressure. Physical Review B - Condensed Matter and Materials Physics, 81(5). https://doi.org/10.1103/PhysRevB.81.054105

Boehler, R., De Hantsetters, K. (2004). New anvil designs in diamond-cells. High Pressure Research, 24(3), 391–396. https://doi.org/10.1080/08957950412331323924

Bouhifd, M. A., Clesi, V., Bolfan-Casanova, N., Hammouda, T., Cartier, C., Manthilake, G., Monteux, J., Andrault, D., Boujibar, A. (2017). Silicate melts during Earth's core formation. Chemical Geology, 461, 128–139. https://doi.org/10.1016/j.chemgeo.2016.12.035

Bouhifd, M. A., Jephcoat, A. P. (2006). Aluminium control of argon solubility in silicate melts under pressure. Nature, 439(7079), 961–964. https://doi.org/10.1038/nature04583

Bouhifd, M. A., Jephcoat, A. P., Heber, V. S., Kelley, S. P. (2013). Helium in earth's

early core. Nature Geoscience, 6(11), 982–986. https://doi.org/10.1038/ngeo1959

Bouhifd, A. M., Jephcoat, A. P., Porcelli, D., Kelley, S. P., Marty, B. (2020). Potential of Earth's core as a reservoir for noble gases: Case for helium and neon. Geochemical Perspectives Letters, 15–18. https://doi.org/10.7185/geochemlet.2028

Cochain, B., Sanloup, C., de Grouchy, C., Crépisson, C., Bureau, H., Leroy, C., Kantor, I., Irifune, T. (2015). Bromine speciation in hydrous silicate melts at high pressure. Chemical Geology, 404, 18–26. https://doi.org/10.1016/j.chemgeo.2015.03.015

Ghosh, D. B., Karki, B. B. (2018). First-principles molecular dynamics simulations of anorthite ($CaAl_2Si_2O_8$) glass at high pressure. Physics and Chemistry of Minerals, 45(6), 575–587. https://doi.org/10.1007/s00269-018-0943-4

Giordano D., Russel J.K., Dingwell D. (2008) Viscosity of magmatic liquids: A model. Earth and Planetary Science Letters 271, 123–134

Hong, X., Newville, M., Duffy, T. S., Sutton, S. R., Rivers, M. L. (2014). X-ray absorption spectroscopy of GeO_2 glass to 64 GPa. Journal of Physics Condensed Matter, 26(3). https://doi.org/10.1088/0953-8984/26/3/035104

Irifune, T., Kurio, A., Sakamoto, S., Inoue, T., Sumiya, H. (2003). Materials: Ultrahard polycrystalline diamond from graphite. Nature 421, 599–600.
https://doi.org/10.1038/421806b

Itié, J. P., Polian, A., Calas, G., Petiau, J., Fontaine, A., Tolentino, H. (1989). Pressure-induced coordination changes in crystalline and vitreous GeO_2. Physical Review Letters, 63(4), 398–401. https://doi.org/10.1103/PhysRevLett.63.398

Kantor, I., Marini, C., Mathon, O., Pascarelli, S. (2018). A laser heating facility for energy-dispersive X-ray absorption spectroscopy. Review of Scientific Instruments, 89(1). https://doi.org/10.1063/1.5010345

Kono, Y., Kenney-Benson, C., Ikuta, D., Shibazaki, Y., Wang, Y., Shen, G., Navrotsky, A. (2016). Ultrahigh-pressure polyamorphism in GeO_2 glass with coordination number $>$ 6. Proceedings of the National Academy of Sciences of the United States of America, 113(13), 3436–3441. https://doi.org/10.1073/pnas.1524304113

Krstulović, M., Rosa, A. D., Biedermann, N., Irifune, T., Wilke, M. (2021). Structural changes in aluminosilicate glasses up to 164 GPa and the role of alkali, alkaline earth cations and alumina in the densification mechanism. Chemical Geology,
https://doi.org/10.1016/j.chemgeo.2020.119980

Krstulović, M., Rosa, A. D., Biedermann, N., Spiekermann, G., Irifune, T., Muñoz, M., Wilke, M. (2020). Ge coordination in $NaAlGe_3O_8$ glass upon compression to 131 GPa.

Physical Review B, 101(21). https://doi.org/10.1103/PhysRevB.101.214103

Lange, R.A. and Carmichael, I.S.E. (1987) Densities of Na_2O–K_2O-CaO-MgO-FeO-Fe_2O_3–Al_2O_3–TiO_2–SiO_2 liquids: New measurements and derived partial molar properties. Geochimica et Cosmochimica Acta, 51, 2931–2946.

Letoullec, R., Pinceaux, J. P., Loubeyre, P. (1988). The Membrane Diamond Anvil Cell: A New Device For Generating Continuous Pressure And Temperature Variations. High Pressure Research, 1(1), 77–90. https://doi.org/10.1080/08957958808202482

Mao, H. K., Bell, P. M., Shaner, J. W., Steinberg, D. J. (1978). Specific volume measurements of Cu, Mo, Pd, and Ag and calibration of the ruby R1 fluorescence pressure gauge from 0.06 to 1 Mbar. Journal of Applied Physics, 49(6), 3276–3283. https://doi.org/10.1063/1.325277

Mathon, O., Beteva, A., Borrel, J., Bugnazet, D., Gatla, S., Hino, R., Kantor, I., Mairs, T., Munoz, M., Pasternak, S., Perrin, F., Pascarelli, S. (2015). The time-resolved and extreme conditions XAS (Texas) facility at the European Synchrotron Radiation Facility: The general-purpose EXAFS bending-magnet beamline BM23. Journal of Synchrotron Radiation, 22, 1548–1554. https://doi.org/10.1107/S1600577515017786

Matsui, M., 2010. High temperature and high pressure equation of state of gold. In Journal of Physics: Conference Series (Vol. 215). https://doi.org/10.1088/1742-6596/215/1/012197

Morard, G., Andrault, D., Antonangeli, D., Nakajima, Y., Auzende, A. L., Boulard, E., Cervera, S., Clark, A., Lord, O.T., Siebert, J., Svitlyk, V., Garbarino, G., Mezouar, M. (2017). Fe–FeO and Fe–Fe_3C melting relations at Earth's core–mantle boundary conditions: Implications for a volatile-rich or oxygen-rich core. Earth and Planetary Science Letters, 473, 94–103. https://doi.org/10.1016/j.epsl.2017.05.024

Murakami, M., Bass, J.D., 2010. Spectroscopic evidence for ultrahigh-pressure polymorphism in SiO_2 glass. Phys. Rev. Lett. 104 (2) https://doi.org/10.1103/PhysRevLett.104.025504.

Nemausat, R., Gervais, C., Brouder, C., Trcera, N., Bordage, A., Coelho-Diogo, C., Florian P., Pakhmatullin, A., Errea, I., Paulatto, L., Lazzeri, M., Cabaret, D. (2017). Temperature dependence of X-ray absorption and nuclear magnetic resonance spectra: Probing quantum vibrations of light elements in oxides. Physical Chemistry Chemical Physics, 19(8), 6246–6256. https://doi.org/10.1039/c6cp08393e

O'Keeffe, M., Hyde, B.G., 1981. The role of nonbonded forces in crystals. In: O'Keeffe, M., Navrotsky, A. (Eds.), Structure and Bonding in Crystals, Vol. 1. Academic

Press Inc., New York, p. 227. Chap. 10

Pascarelli, S., Mathon, O., Mairs, T., Kantor, I., Agostini, G., Strohm, C., Pasternak, S., Perrin, F., Berruyer, G., Chappelet, P., Clavel, C., Dominguez, M. C. (2016). The Time-resolved and Extreme-conditions XAS (Texas) facility at the European Synchrotron Radiation Facility: The energy-dispersive X-ray absorption spectroscopy beamline ID24. In Journal of Synchrotron Radiation (Vol. 23, pp. 353–368). International Union of Crystallography. https://doi.org/10.1107/S160057751501783X

Petitgirard, S., Malfait, W.J., Journaux, B., Collings, I.E., Jennings, E.S., Blanchard, I., Kantor, I., Kurnosov, A., Cotte, M., Dane, T., Burghammer, M., Rubie, D.C. (2017). SiO_2 Glass Density to Lower-Mantle pressures. Phys. Rev. Lett. 119 (21) https://doi.org/10.1103/PhysRevLett.119.215701.

Petitgirard, S., Sahle, C. J., Weis, C., Gilmore, K., Spiekermann, G., Tse, J. S., Wilke, M., Cavallari, C., Cerantola, V., Sternemann, C. (2019). Magma properties at deep Earth's conditions from electronic structure of silica. Geochemical Perspectives Letters, 9, 32–37. https://doi.org/10.7185/geochemlet.1902

Pohlenz, J., Rosa, A.D., Mathon, O., Pascarelli, S., Belin, S., Landrot, G., Murzin, V., Veligzhanin, A., Shiryaev, A., Irifune, T., Wilke, M., 2018. Structural controls of CO_2 on Y, La and Sr incorporation in sodium-rich silicate - carbonate melts by *in-situ* high P-T EXAFS. Chem. Geol. 486, 1–15. https://doi.org/10.1016/j.chemgeo.2017.12.023.

Pradhan, G. K., Fiquet, G., Siebert, J., Auzende, A. L., Morard, G., Antonangeli, D., Garbarino, G., 2015. Melting of MORB at core-mantle boundary. Earth and Planetary Science Letters, 431, 247–255. https://doi.org/10.1016/j.epsl.2015.09.034

Prescher, C., Prakapenka, V. B., Stefanski, J., Jahn, S., Skinner, L. B., Wang, Y. (2017). Beyond sixfold coordinated Si in SiO_2 glass at ultrahigh pressures. Proceedings of the National Academy of Sciences of the United States of America, 114(38), 10041–10046. https://doi.org/10.1073/pnas.1708882114

Rehr, J. J., Kas, J. J., Vila, F. D., Prange, M. P., Jorissen, K. (2010, June 7). Parameter-free calculations of X-ray spectra with FEFF9. Physical Chemistry Chemical Physics. https://doi.org/10.1039/b926434e

Ringwood, A. E., 1982. Phase transformations and differentiation in subducted lithosphere: implications for mantle dynamics, basalt petrogenesis, and crustal evolution. Journal of Geology, 90(6), 611–643. https://doi.org/10.1086/628721

Rosa, A. D., Mathon, O., Torchio, R., Jacobs, J., Pasternak, S., Irifune, T., Pascarelli, S. (2019). Nano-polycrystalline diamond anvils: key devices for XAS at extreme conditions: their use, scientific impact, present status and future needs. High Pressure Research.

https://doi.org/10.1080/08957959.2019.1700978

Sanloup, C., Drewitt, J. W. E., Konôpková, Z., Dalladay-Simpson, P., Morton, D. M., Rai, N., Van Westrenen, W., Morgenroth, W. (2013). Structural change in molten basalt at deep mantle conditions. Nature, 503(7474), 104–107. https://doi.org/10.1038/nature12668

Sato, T., Funamori, N. (2010). High-pressure structural transformation of SiO_2 glass up to 100 GPa. Physical Review B - Condensed Matter and Materials Physics, 82(18). https://doi.org/10.1103/PhysRevB.82.184102

Shen, G., Mei, Q., Prakapenka, V. B., Lazor, P., Sinogeikin, S., Meng, Y., Park, C. (2011). Effect of helium on structure and compression behavior of SiO_2 glass. Proceedings of the National Academy of Sciences of the United States of America, 108(15), 6004–6007. https://doi.org/10.1073/pnas.1102361108

Spera, F.J., Nevins, D., Ghiorso, M., Cutler, I., (2009). Structure, thermodynamic and transport properties of $CaAl_2Si_2O_8$ liquid. Part I: Molecular dynamics simulations. Geochim. Cosmochim. Acta 73 (22), 6918–6936. https://doi.org/10.1016/j. gca.2009.08.011.

Williams, Q., Jeanloz, R. (1988). Spectroscopic evidence for pressure-induced coordination changes in silicate glasses and melts. Science, 239(4842), 902–905. https://doi.org/10.1126/science.239.4842.902

Winterer, M., (1997). XAFS - a data analysis program for materials science in proceedings of the 9th international conference on X-ray absorption fine structure. J. Phys. IV France 7, C2–243.

Chapter 5

Supplemental Information to Chapter 4

Effect of temperature on the densification of silicate melts to lower Earth's mantle conditions

Marija Krstulović[1, 2], Angelika D. Rosa[1], Dario Ferreira Sanchez[3], Lélia Libon[2], Christian Albers[4], Margarita Merkulova[5], Daniel Grolimund[3],Tetsuo Irifune[6], Max Wilke[2]

[1]European Synchrotron Radiation Facility, ESRF, 71 Avenue des Martyrs, 38000 Grenoble, France

[2]University of Potsdam, Institute of Geosciences, Karl-Liebknecht-Str. 24-25, 14476 Potsdam-Golm, Germany

[3]Swiss Light Source, SLS, Paul Scherrer Institut, Forschungsstrasse 111, 5232 Villigen, Switzerland

[4]Technische Universität Dortmund, Department of Physics, Otto-Hahn-Str. 4 44227 Dortmund, Germany

[5]Gent University, Faculty of Sciences, Department of Geology, Pore-scale Processes in Geomaterials Research Group (PProGRess)/UGCT,Ghent University, 9000 Ghent, Belgium

[6]Ehime University Johoku Campus, Geodynamics Research Center, 2-5 Bunkyocho, Matsuyama, Ehime 790-0826, Japan

Corresponding Author: Marija Krstulović, krstulov@uni-potsdam.de

Keywords: silicate melts, densification, high pressure, high temperature, XANES, coordination number

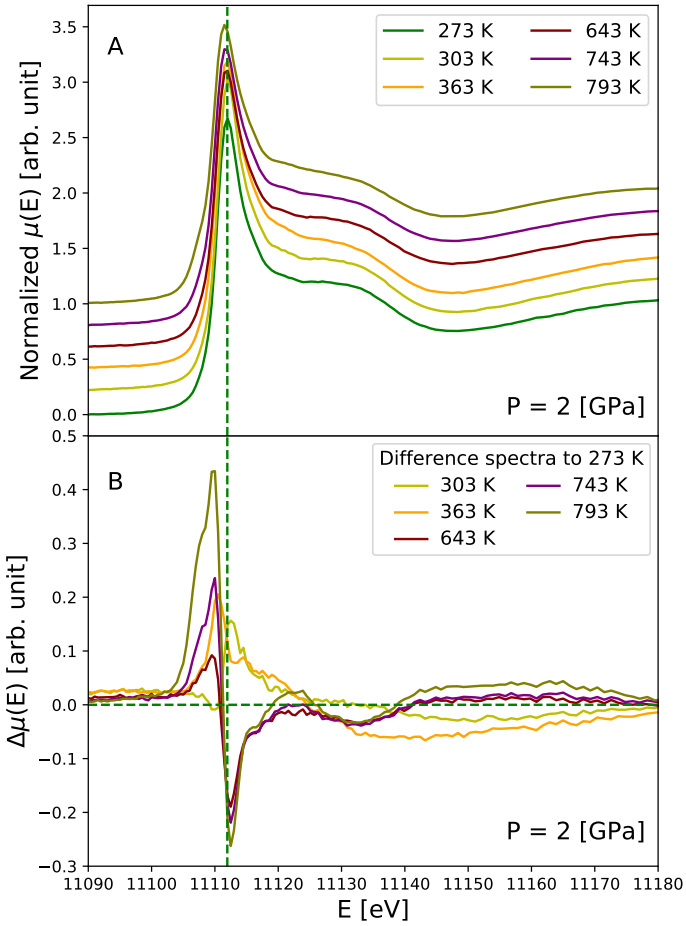

Figure 5.1: Normalized Ge K edge XANES spectra of AbDi-glass at isobaric conditions of 2 GPa and with temperature increasing from 273 to 793 K. The spectra are incrementally shifted along the vertical axis for the sake of clarity. The vertical dashed line cuts the spectra at the energy point of the maximum of the main XANES peak or first XANES peak maximum FXPM at 273 K (FIG. 5.1A). Difference spectra of the corresponding normalized XANES spectra at high temperature to the spectrum at room temperature (FIG. 5.1B)

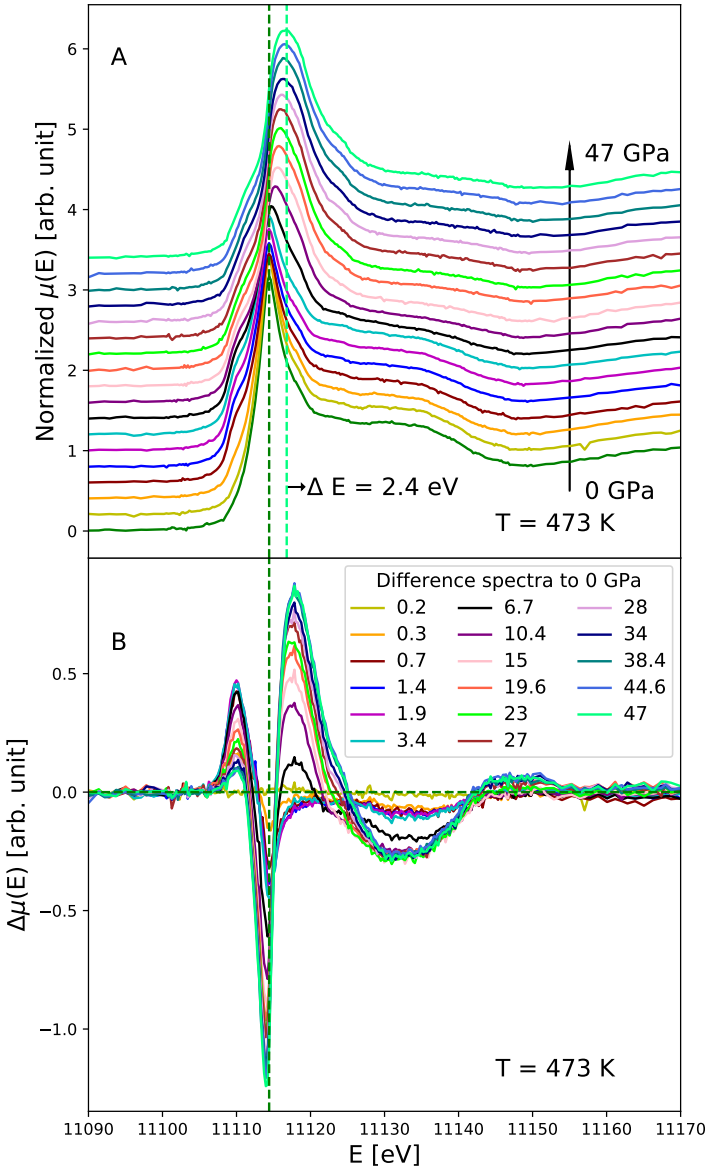

Figure 5.2: Normalized Ge K edge XANES spectra of AbDi-glass at isothermal conditions of 473 K and under compression to 47 GPa. The spectra are incrementally shifted along the vertical axis for the sake of clarity. The vertical dashed line cuts the spectra at the energy point of the maximum of the main XANES peak or first XANES peak maximum FXPM at room pressure, whereas vertical light green line cuts the FXPM of the spectrum acquired at the highest probed pressure of 47 GPa (FIG. 5.2A). Difference spectra of the corresponding high pressure normalized XANES spectra to the spectrum at ambient pressure (FIG. 5.2B).

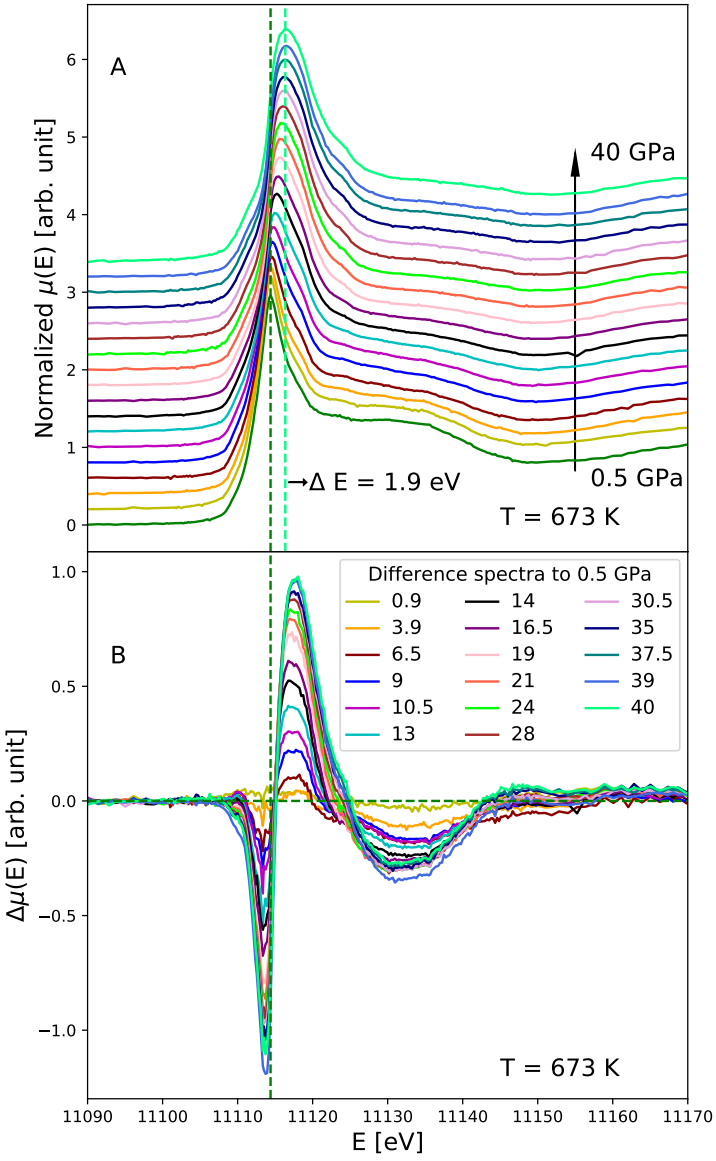

Figure 5.3: Normalized Ge K edge XANES spectra of AbDi-glass at isothermal conditions of 673 K and under compression to 40 GPa. The spectra are incrementally shifted along the vertical axis for the sake of clarity. The vertical dashed line cuts the spectra at the energy point of the maximum of the main XANES peak or first XANES peak maximum FXPM at the lowest probed pressure of 0.5 GPa, whereas the vertical dashed light green line cuts the FXPM of the spectrum acquired at the maximum probed pressure of 40 GPa (FIG. 5.3A). Difference spectra of the corresponding high pressure normalized XANES spectra to the spectrum at the lowest probed pressure (FIG. 5.3B).

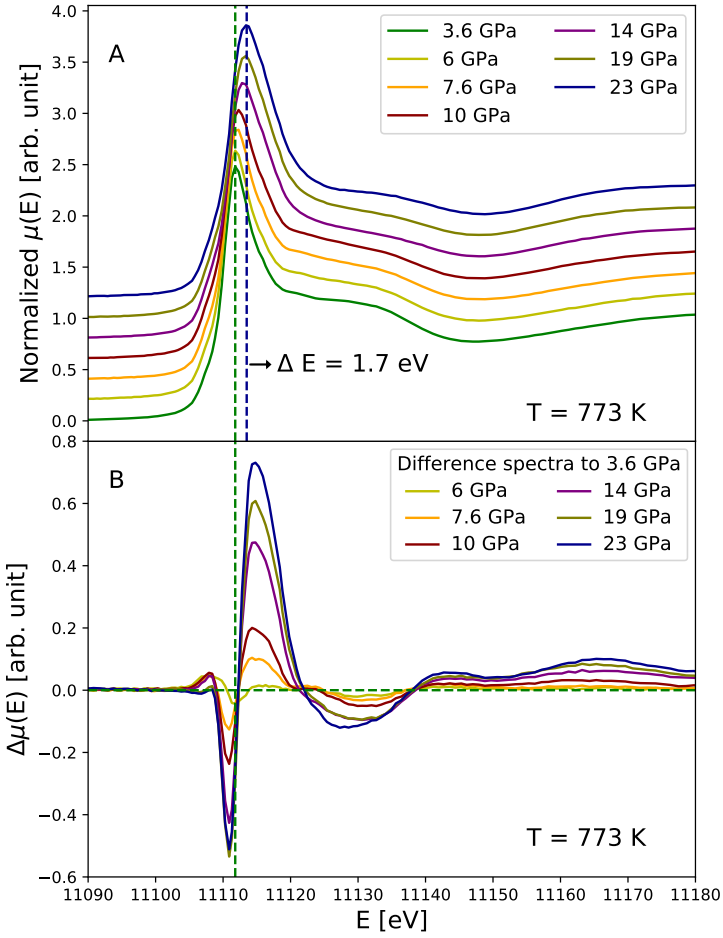

Figure 5.4: Normalized Ge K edge XANES spectra of AbDi-glass at isothermal conditions of 773 K and under compression to 23 GPa. The spectra are incrementally shifted along the vertical axis for the sake of clarity. The vertical green dashed line cuts the spectra at the energy point of the maximum of the main XANES peak or first XANES peak maximum FXPM at the lowest probed pressure of 3.6 GPa, whereas the violet dashed line cuts the FXPM of the spectrum at the highest probed pressure of 23 GPa (FIG. 5.4A). Difference spectra of the corresponding high pressure normalized XANES spectra to the spectrum at the lowest probed pressure (FIG. 5.4B).

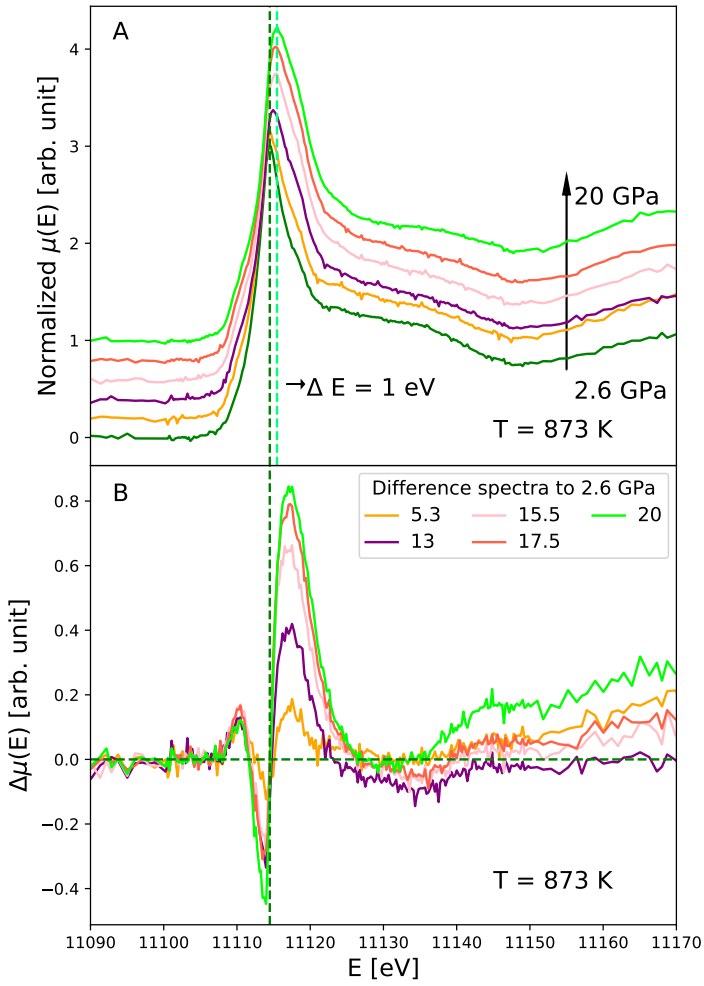

Figure 5.5: Normalized Ge K edge XANES spectra of AbDi-glass at isothermal conditions of 873 K and under compression to 20 GPa. The spectra are incrementally shifted along the vertical axis for the sake of clarity. The vertical green dashed line cuts the spectra at the energy point of the maximum of the main XANES peak or first XANES peak maximum FXPM at the lowest probed pressure of 2.6 GPa, whereas the light green dashed line cuts the FXPM of the spectrum at the highest probed pressure of 20 GPa (FIG. 5.5A). Difference spectra of the corresponding high pressure normalized XANES spectra to the spectrum at the lowest probed pressure (FIG. 5.5B).

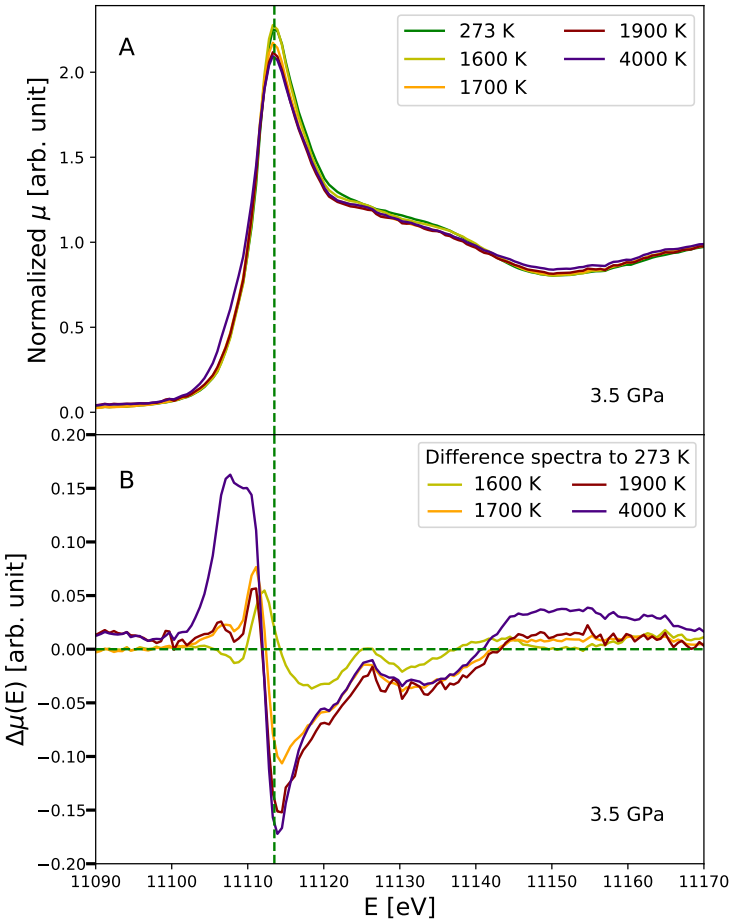

Figure 5.6: Normalized Ge K edge XANES spectra of AbDi-glass at isobaric conditions of 3.5 GPa and at temperatures increasing from 273 to 4000 K. The vertical green dashed line cuts the spectra at the energy point of the maximum of the main XANES peak or first XANES peak maximum FXPM at room temperature (FIG. 5.6A). Difference spectra of the corresponding normalized XANES spectra at high temperature to the spectrum at room temperature (FIG. 5.6B).

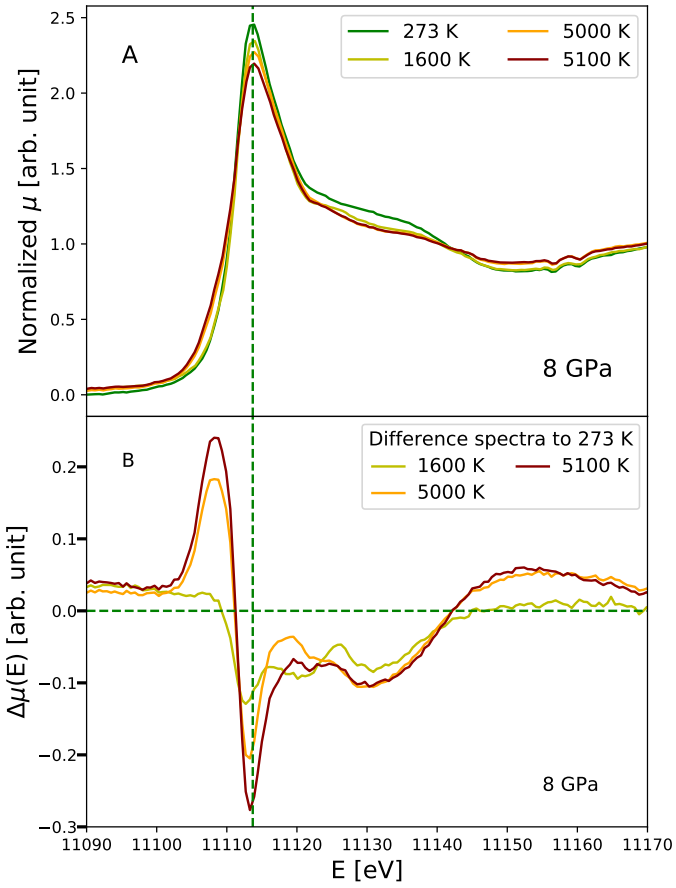

Figure 5.7: Normalized Ge K edge XANES spectra of AbDi-glass at isobaric conditions of 8 GPa and at temperatures increasing from 273 to 5100 K. The vertical green dashed line cuts the spectra at the energy point of the maximum of the main XANES peak or first XANES peak maximum FXPM at room temperature (FIG. 5.7A). Difference spectra of the corresponding normalized XANES spectra at high temperature to the spectrum at room temperature (FIG. 5.7B).

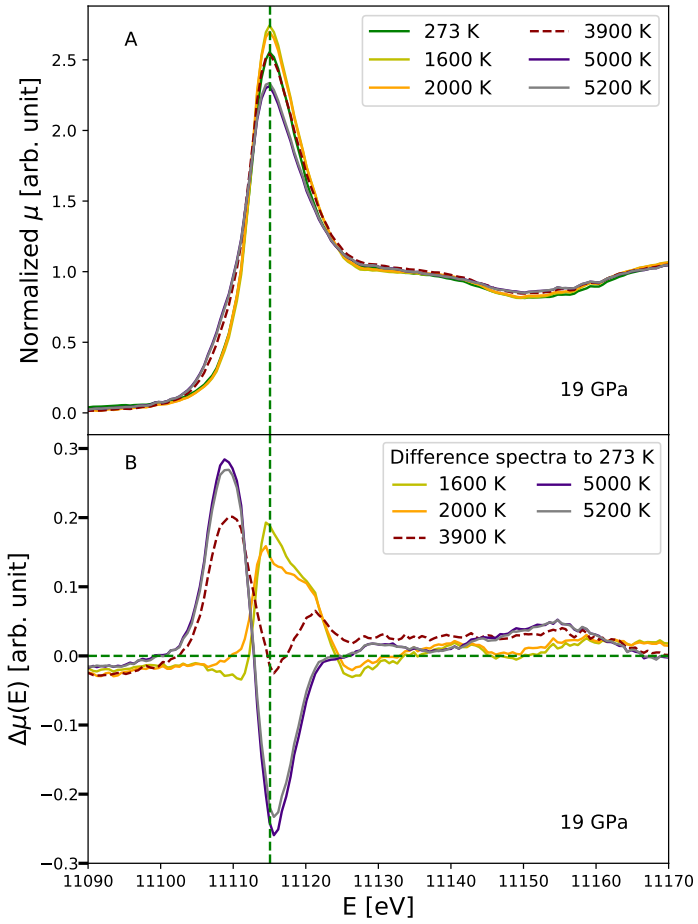

Figure 5.8: Normalized Ge K edge XANES spectra of AbDi-glass at isobaric conditions of 19 GPa and at temperatures increasing from 273 to 5200 K. The vertical green dashed line cuts the spectra at the energy point of the maximum of the main XANES peak or first XANES peak maximum FXPM at room temperature (FIG. 5.8A). Difference spectra of the corresponding normalized XANES spectra at high temperature to the spectrum at room temperature (FIG. 5.8B).

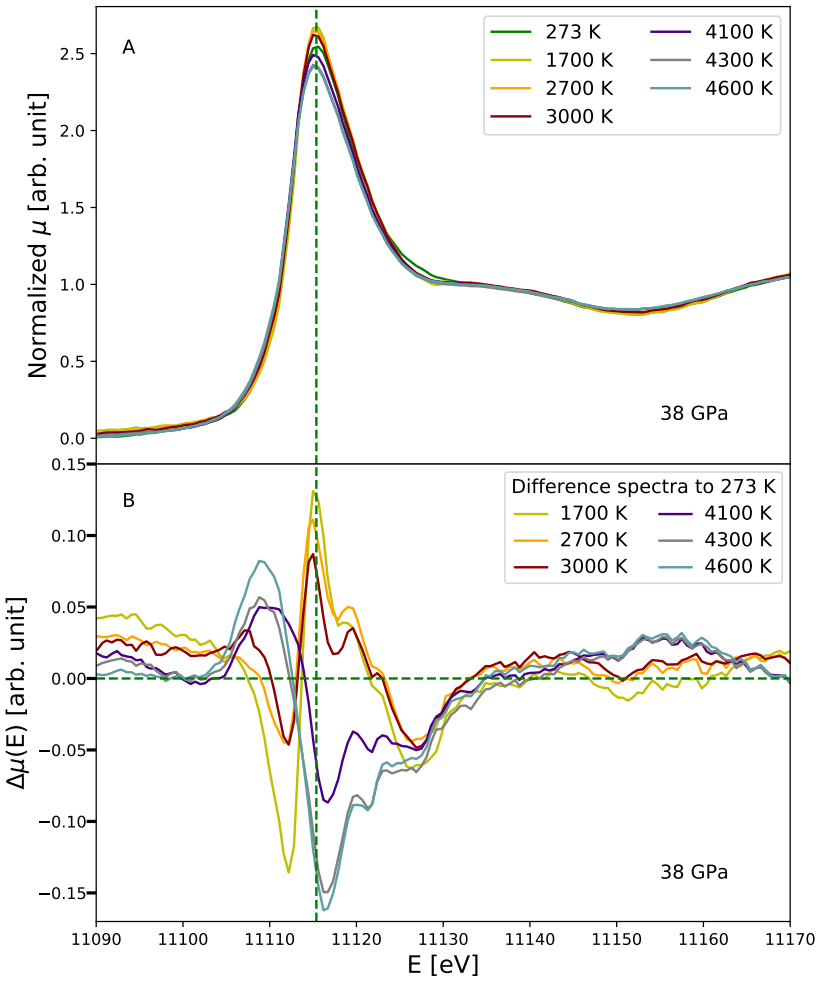

Figure 5.9: Normalized Ge K edge XANES spectra of AbDi-glass at isobaric conditions of 38 GPa and at temperatures increasing from 273 to 4600 K. The vertical green dashed line cuts the spectra at the energy point of the maximum of the main XANES peak or first XANES peak maximum FXPM at room temperature (FIG. 5.9A). Difference spectra of the corresponding normalized XANES spectra at high temperature to the spectrum at room temperature (FIG. 5.9B).

Chapter 6

Discussion and conclusions

The focus of this thesis was the investigation of the structural changes in silicate glasses and melts at high pressure and temperature conditions in order to constrain the structure of natural basaltic melts at the conditions of the deep Earth interior. We performed multiple extensive XAS experiments coupled to high pressure and temperature instrumentation (DAC, RH-DAC, LH-DAC) on aluminosilicate and aluminogermanate glasses in order to track their atomic-scale structure. Ge K edge in Ge-albite glass $NaAlGe_3O_8$ at room temperature up to 131 GPa, as well as Ge and Sr K edge in Ge and Sr doped albite and albite-diopside glasses up to 42 and 164 GPa, were studied primarily using EXAFS. Further, a series of XAS experiments on Ge K edge in albite-diopside composition was performed up to maximum 48 GPa, and with temperatures up to about 5000 K, primarily using XANES spectra. In performed experiments, network forming Ge and network modifying Sr served as monitoring elements for geologically relevant elements Si, Al (network former) and Ca, Na, K or Mg (network modifiers) that cannot be directly studied using XAS coupled to the high-pressure instrumentation. The results provide a comprehensive dataset on the compression-induced densification mechanism in silicate melts depending on two main factors: composition and temperature.

Main findings of this work can be summarized in the following 5 points. 1) In aluminosilicate glasses and melts structural changes of both network formers and network modifiers can be characterized as a smooth and gradual process. 2) Ge coordination number increases from 4 to 6, and Sr coordination from 6 to at least 9 within the first ∼25 to 30 GPa. 3) At pressures above 25 - 30 GPa, in all studied glasses and around both studied elements the structural transformations terminate and are replaced by pure isostructural compaction that persists as a unique compression mechanism up to ultra-high pressure conditions. 4) In aluminosilicate glasses Ge polyhedra have much higher compressibility than Ge and Si polyhedra in GeO_2 and SiO_2 glasses. 5) High temperature shifts the tetrahedral to octahedral structural transformation in aluminosilicate melts to lower pressure compared to glasses.

In the following paragraph, the results of this work will be discussed with respect to the effects of the chemical composition on the densification process of Ge and Sr. First, we will pay attention on the densification process of network formers vs. network modifiers in the studied glasses. Further, the role of Al, alkali and alkaline earth metals on the densification process will be elucidated. In this context, structural evolution of the glasses studied here will be compared with observations from the literature. Finally, the role of the temperature on the densification mechanism will be introduced in the discussion.

1) Structural evolution of network formers vs. network modifiers:

In this thesis, structural changes of network formers and network modifiers in silicate glasses and melts have been a subject of investigation. In this context we studied Ge as a monitoring element for network forming cations such as Si, and Sr as a monitoring element for network modifying cations such as Ca, Na, Mg but also trace elements Y or La, for example. Our study showed that under compression both, Ge and Sr undergo gradual structural transformations, i.e. a change in coordination, within the first ∼25 – 30 GPa, which is best expressed in terms of the evolution of the inter-atomic distances and the coordination number parameter (Chapter 2, Chapter 3). However, apart from this generally similar trend of the fitted parameters, the fitted bond distances of these two elements reveal that there are severe differences between the response of Ge and Sr to compression. While the overall Ge-O distance increase during the 4- to 6-fold conversion is about 0.1 Å, much smaller overall increase of the Sr-O distances of less than 0.03 Å characterizes the 6- to ∼9-fold conversion of Sr in the same materials. Weak increase of Sr-O distances during the conversion of the Sr coordination is followed by a weak shrinkage of the Sr-O bond lengths at pressures exceeding ∼26 GPa. Also here, Ge behaves in a different way and exhibits considerable shrinkage of the interatomic distances at pressures above the completion of the octahedral coordination of Ge. The fact that in both cases above 26 i.e. 30 GPa the bond distances constantly shorten, indicates that the polyhedra undergo isostructural compaction and that no further changes in the coordination symmetry or number occur. Further increase of the coordination number would require increase of the bond distances according to the bond valence theory (Brown, 2009; Pauling, 1929). According to this theory, the increase of the Ge-O bond lengths during tetrahedral to octahedral coordination change is ruled by the local charge requirements, and the contraction of the Ge-O bond lengths in tetrahedral coordination is not possible because the bond-valence sum around oxygen atoms would exceed the ideal value, which is for BO 2. According to this rule, local charge requirements dictate the increase of the metal to oxygen bond distances during the increase of the coordination number (O'Keeffe Hyde, 1981; Chapter 2). Because the data on Sr are limited to the pressure of about 42 GPa it is not possible to fully rule out further potential changes in the structure of Sr at pressures exceeding 42 GPa.

In addition to the bond valence rule, an important concept explaining differences in the behavior of cations during structural changes is the concept of nonbonded forces in crystalline and non-crystalline materials developed by O'Keeffe and Hyde (1981). According to this theory the central parameter defining the overall structure is the ratio between the nonbonded cation radius R and the cation-anion bond length l. According to this concept, structural changes are governed by cation-cation repulsive forces based on observations of large reductions of anion-anion distances under compression, and small reduction of cation-cation distances (O'Keeffe and Hyde. 1981; see also Chapter 2 and Chapter 3). Following this rule, we can see that for larger cations such as network modifying Sr, the R/l ratio is smaller (≤ 0.70 calculated from Sr...Sr and Sr-O distances for Sr in perovskite structure, Albornoz et al., 2013) compared to Ge (0.89, O'Keeffe and Hyde, 1981) or Si (0.93, O'Keeffe and Hyde, 1981) as the presence of larger cations increases the cation-cation distances. At very high pressure larger cation-cation distances allow stronger reduction of nonbonded distances between for example Ge...Sr or Si...Sr than for example between Ge...Ge or Si...Si, therefore critical threshold of Ge...Ge or Si...Si distances is reached at lower pressure than between Ge or Si and larger network modifying cations (Sr, Ca, Na). This is important contribution of the large network modifying cations on the compression style of network formers as it promotes their increased structural flexibility under compression.

This concept is, together with the bond valence theory, the main explanation for the

above described differences in the compression response of Ge and Sr. Several following aspects that are related to the bond-valence rule and (or) to the theory on nonbonded forces can be considered when speaking about differences in the overall bond distance extension between Ge-O and Sr-O during the structural transformations. One is the difference in the roles that Ge and Sr play in the glass. Due to their overall larger network flexibility, network modifier like Sr can tolerate shorter distances to their neighbors compared to network formers. In contrast to network forming cations like Ge, larger network modifying cations like Sr can provide more space for oxygen atoms. Apart from their different role in the system, the differences between Ge-O and Sr-O bond length extension are primarily based on the ionic size differences between Ge and Sr, where higher compressibility of larger Sr ions compared to Ge facilitates more efficient packing of anions (oxygen) without considerable bond distance extension, which is also related to the theory of nonbonded forces as the nonbonded radius for Sr is much larger than for Ge, smaller overall Sr-O bond length extension under compression is required compared to Ge. Finally, the overall larger coordination number difference between these two cations is a third reason. All these factors facilitate smaller overall Sr-O bond distance extension during structural transformations compared to Ge-O distances. We observe that the increase of the bond distance is not linearly correlated to the increase of the coordination number under compression. Whereas the average Sr-O bond distance is larger than the average Ge-O bond length because of the larger coordination number of Sr compared to Ge (at ambient pressure Sr is 6-fold coordination, whereas Ge is 4-fold coordinated), and also because of the lower charge of Sr compared to Ge, the increase from the 4- to 6-fold coordination of Ge requires much larger increase of the Ge-O distances than the increase of the Sr-O distances from 6 to at least 9 (Chapter 3), which can be related to the above mentioned difference of the R/l ratio in Sr compared to Ge.

2) Compositional effect on the densification mechanism of silicate glasses under compression:

Major task of this thesis was understanding the role of the chemical complexity on the densification process of silicate glasses and melts. This goal was successfully reached and is clearly demonstrated in Chapter 2 and 3. Results presented consistently evidence the considerable role of Al, alkali and alkaline earth cations on the compaction of silicate/germanate glasses. The influence of these cations on the densification mechanism in studied glasses is best expressed in the context of the behavior of the Ge-O distances in these glasses compared to Ge-O and Si-O distances in simple SiO_2 and GeO_2 glasses (Kono et al., 2017; Prescher et al., 2017; Sato and Funamori, 2010; Spiekermann et al., 2019). Whereas in the pressure range of the tetrahedral to octahedral conversion Ge-O distances in the complex glasses studied here follow similar pressure trend to simple oxides, at pressures beyond the completion of the octahedral coordination (above ∼30 GPa) Ge-O distances in aluminoslicate and aluminogermanate glasses experience much stronger reduction under compression compared to Si-O and Ge-O bond lengths in simple oxides (Chapter 2, Chapter 3). This is best demonstrated by the comparison of the relative bond distance evolution in aluminosilicate glasses from this work and the Si-O distaneces (Prescher et al., 2017; Sato and Funamori, 2010) and Ge-O distances (Baldini et al., 2010; Hong et al., 2014; Spiekermann et al., 2019) from SiO_2 and GeO_2 glasses. A low Si-O and Ge-O bond distance reduction in simple oxides at pressures above ∼30 GPa is due to presence of only highly charged cations Ge and Si, which causes octahedral distortion in these compounds under compression due to strong cation-cation repulsion (O'Keeffe and Hyde, 1981). On the other side, strong reduction of the Ge-O distances in complex $NaAlGe_3O_8$ and albite-diopside glass at pressures above the completion of the octahedral coordination are due to pure shrinkage of undistorted octahedra. This is facilitated by the presence of large network modifying cations and thus NBOs that may accommodate larger parts of the densification,

inhibiting polyhedral distortion. Moreover, compared to Ge, Al shows for the same coordination number larger bond distance which is due to its overall lower charge, and correspondingly lower bond strength of Al. Thus, both, Al and the network modifiers contribute to the higher polyhedral compressibility in aluminosilicate glasses compared to pure oxides. In this way the polyhedral volume shrinkage is possible even once the second nearest neighbors Ge...Ge, Ge...Si and Si...Si reach their critical threshold distances thanks to further reduction of Na-O, Al-O, Ca-O or Si-O and Ge-O as long as the next nearest neighbors (Na-Ge, Al-Ge, Ca-Ge) reach their critical threshold distance, as explained by the theory of nonbonded forces (O'Keeffe and Hyde, 1981). Only once this threshold is reached, the distortion of the polyhedra occurs (Chapter 2, Chapter 3) which is not clearly observed in studied aluminogermanate and aluminosilicate glasses within the entire probed pressure range.

In addition to Ge-O bond distances, which we tracked beyond megabar pressures in order to elucidate densification mechanism in aluminosilicate and aluminogermanate glasses and the influence of chemical composition on the densification process, we studied also local coordination environment of Sr, which is presented in Chapter 3. In the pressure range of the structural transformations from 6- to ∼9-fold, which covers the pressure range up to about 26 GPa, the Sr-O distances slightly increase. Beyond this pressure, the distances slightly shorten. Thus, in studied complex glasses, Sr also shows that structural transformations occur in the pressure range up to maximum 26 i.e. 30 GPa, and that at higher pressures the densification mechanism is characterized by isostructural compaction of the polyhedral units. Because this is the only study on the structural properties of Sr in glasses at pressures exceeding upper mantle conditions (Pohlenz et al., 2018), it was not possible to make a direct comparison of the behavior of Sr in aluminosilicate glasses to Sr in in $SrSiO_3$ glass as literature data are not available. We therefore compared the behavior of the Sr-O distances in aluminosilicate glasses from this work to Sr-O distances in crystalline $SrSiO_3$ (Xiao et al., 2013; Yusa et al., 2005) and $SrCO_3$ (Biedermann et al., 2020) as well as with Mg-O distances in $MgSiO_3$ glass that was probed to megabar pressure (Kim et al., 2019). Even though crystalline samples are not truly appropriate for the comparison, we learned that Sr-O distances in aluminosilicate glasses reach their maximum at about 26 GPa, which corresponds well to the pressure of the conversion from the carbonate strontian into post-aragonite structure in crystalline $SrCO_3$ (Biedermann et al., 2020), and roughly to the pressure of the conversion of $SrSiO_3$ into perovskite structure (Xiao et al., 2013; Yusa et al., 2005). The comparison showed that at high pressure Sr-O distances in aluminosilicate glasses are much longer than in crystalline phases. Further difference is that unlike in crystalline phases, where the phase change abruptly occurs, in the studied glasses the phase transformation is a continuous process extending over a large pressure range. In comparison to amorphous $MgSiO_3$, where Mg-O bond distances continuously decrease under compression up to about 40 GPa, even during the increase of the coordination number from 6 to 8 (Kim et al., 2019), we found a slight increase of Sr-O bond lengths during the 6- to 9-fold coordination transformation up to 26 GPa and a subsequent bond distance reduction above 26 GPa, Mg-O bond distances continuously decrease under compression even during the pressure range of the coordination number increase from 6 to 8 (Kim et al., 2019) that covers the pressure range up to about 40 GPa. We assume that in aluminosilicate glasses at least to some extent the increase of the Sr-O bond distances is due to presence of Al in the system which allows Sr to play not only the role of network modifier, but also the role of charge compensator for Al, which has been previously reported in a study on Sr in silicate and aluminosilicate glasses (Cormier et al., 1999), whereas in pure silicate melts it acts solely as network modifier (Henderson et al., 1985). Additionally, it is not excluded that Sr coordination number increase is in overall larger than the fitted coordination number of 9. Underestimation of the fitted Sr coordination number in studied glasses could be related to the multi-electronic excitations MEE that distort the EXAFS signal (D'Angelo et al., 1996), and may lead to the underestimation of the fitted

coordination number parameter.

3) The role of temperature in the densification process of complex aluminosilicate glasses:

In Chapter 4 of this thesis the influence of temperature on the structural transformations in aluminosilicate melts was studied. For this, we studied albite-diopside glass under compression to 48 GPa and at different temperatures up to maximum 5000 K. In general, there are three different states of the amorphous compound at high temperature. The glass persists up to the glass transition temperature, that is followed by a super cooled melt, which covers the temperature range just above the glass transition temperature, and the third state is the melt, or liquid at superliquidus temperatures. For the studied composition we do not know the exact temperature range of the super cooled melt, but it can be estimated from viscosity data on the Ge-free counterpart, e.g. Giordano et al. 2008. This range is limited by the onset of crystallization, which again is strongly controlled by the viscosity that controls nucleation and crystal growth rates. XANES and EXAFS spectra are very sensitive to local ordering that may occur at the onset of crystallization and thus the spectra allow distinguishing between glassy and crystalline samples. Compared to glasses, liquid samples will show an enhanced damping of the EXAFS-signal due to enhanced configurational disorder.

In this work three possible scenarios for the role of the temperature on the structural transformations under compression were considered: a) neutral role, when the structural changes under compression at high temperature follow the same structural pattern like at room temperature; b) shift of the structural transformations to lower pressure due to enhanced kinetics by thermal energy (only works for glass) or due to configurational adjustments (works for melts); c) delay of the structural transformations due to thermal expansion of bond distances. According to the results provided in Chapter 4, temperatures below 1000 K do not influence structural transformations in the studied composition which is related to the glassy nature of the material at this temperature range, whereas at much higher temperatures of 1600 K and above under compression structural transformations are shifted to lower pressures. This shift of the structural changes to lower pressures is related to the liquid state of the material. Thus, at temperatures below 1000 K structural transformations in studied glasses occur in the pressure range up to about 26 to maximum ∼30 GPa, whereas at temperatures of 1600 K and above, in the melts structural transformations are completed already at about 20 GPa. This shows that for the same composition, in melts the completion of the octahedral coordination is shifted to about 30 % lower pressure compared to the glasses. At low pressure, this shift appears to be less dramatic, and the onset of the structural changes in the melts is shifted to about 15 % to lower pressure compared to glasses (Chapter 4). This indicates that at low pressures melts are stronger affected by the effect of thermal expansion than at high pressure for the same temperature.

In conclusion, this thesis is the first systematic investigation of the structural properties of chemically complex aluminosilicate glasses and melts at the conditions relevant for the deep Earth‘s interior. It provides a detailed dataset on the effect of two important factors on the compression mechanism of silicate melts: chemical composition and temperature. It also monitors structural behavior not only of usually studied network forming elements, but also of network modifiers. A major contribution of this study is the observed high polyhedral compressibility in studied aluminosilicate glasses compared to simple oxides SiO_2 and GeO_2 at pressures above the completion of the octahedral coordination (Chapter 2, Chapter 3). This high compressibility is best expressed in the strong shrinkage of the interatomic Ge-O distances in complex glasses compared to Ge-O and Si-O distances in simple oxides. This shows that the simple oxides GeO_2 and SiO_2 that commonly serve as an analogue for melts at the deep Earth

interior (Kono et al., 2017; Prescher et al., 2017; Spiekermann et al., 2019) are not reliable models for natural melt properties at the conditions of the lower mantle (Chapter 2, Chapter 3). Strong reduction of the bond distances in aluminosilicate glasses beyond the completion of the sixfold coordination shows unambiguously that, once the octahedral coordination is completed, no further polyhedral transformations in the structure occur (Chapter 2, Chapter 3). Some previous XRD studies proposed the emergence of the 7-fold species in SiO_2 and GeO_2 glasses (Kono et al., 2017; Prescher et al., 2017). However, these studies provide an inconsistent picture, i.e. they show an increasing coordination number with parallel bond distance reduction (Prescher et al., 2017), which is not in agreement with bond valence rules (Brown, 2009; Pauling 1929). Therefore, following the conception proposed by Spiekermann et al. (2019), we conclude that, similar to aluminosilicate glasses, GeO_2 and SiO_2 glasses also keep octahedral coordination even at pressures exceeding megabar conditions, but a weaker shrinkage of the Ge-O/Si-O distances is observed in these glasses (Prescher et al., 2019; Spiekermann et al., 2019) due to octahedral distortion at ultra-high pressures.

The results on the temperature effects on the structural transformations in aluminosilicate melts are an important step towards the real behavior of the silicate melts in the natural environment of the Earth‘s interior. For the study at high-pressure and high-temperature conditions, albite-diopside glass was probed. It represents a simplified basaltic melt, and thus, a good model for melts in the mantle as basalts can exist at various depths of the mantle. So far, only a few experimental high pressure and high temperature studies on structural properties of silicate melts exist (Pohlenz et al., 2018; Sanloup et al., 2013) supported by a few MD studies (Bajgain et al., 2015; Ghosh and Karki, 2018; Spera et al., 2009). For the conditions of the lower mantle, the work on molten basalt up to 60 GPa and at temperatures between 2200 and 3200 K (Sanloup et al., 2013) is of particular importance. However, due to missing data on basaltic glasses compressed at room temperature it is difficult to answer the question whether and how temperature influences the densification of silicate melts. The detailed structural behavior of the albite-diopside glass under compression at room and at high temperature provided results that allow us to identify the role of the temperature on the densification of the melts (Chapter 3, Chapter 4). The results presented in Chapter 4 showed that temperatures relevant for the Earth's mantle shift structural transformations to lower pressure leading to the completion of the octahedral coordination in the melts at about 30 % lower pressure compared to glasses. Based on presented observations, it is reasonable to assume that in natural silicate melts the coordination of Si also experiences similar temperature effects with a shift of the completion of the octahedral coordination of Si to about 30 % lower pressure. In a MD study on liquid anorthite (Ghosh and Karki, 2018), structural changes around Si and other cations occur in the first 20 to 30 GPa. The experimental study on molten basalt (Sanloup et al., 2013) reported the completion of sixfold coordinated Si at about 35 GPa. If we compare the findings on molten basalt and anorthite to results on SiO_2 glass under compression, we can see that recent studies on SiO_2 glass at room temperature suggested the completion of sixfold coordinated Si at about 60 GPa, which is considerably higher pressure compared to observations on molten basalt (Sanloup et al., 2013). If we keep in mind the pressure difference of about 30 % for the completion of the octahedral coordination between albite-diopside melts and their corresponding glasses, we may speculate that if in SiO_2 glass at room temperature the octahedral coordination is completed at about 60 GPa, in molten silica it could be at about 40 GPa. This estimated pressure corresponds very well to the pressure at which the SiO_2 melting curve shows a considerable change in slope as determined by Andrault et al. (2014), which these authors attributed to the coordination change in the melt. The value for the albite-diopside glass is slightly higher compared to 35 GPa reported by Sanloup et al. (2013) and could be attributed to the compositional effects. We thus propose that sixfold coordination in natural silicate melts

is completed at about 40 GPa.

Geological implications

The results of this thesis illustrate a detailed picture of natural silicate melts at the conditions of the lower and lower most mantle. The results show that in the Earth the densification of basaltic melts is accompanied by continuous structural transformations that take place in the pressure range up to about 40 GPa (Chapter 4) and that most likely at higher pressures no further coordination changes in the structure occur up to the CMB (Chapter 3, Chapter 4). Instead, the melts undergo isostructural compaction with high polyhedral compressibility. In the context of the discussion about the existence of the ultra-dense and gravitationally stable silicate melts in so called ultra-low velocity zones (ULVZs) at the bottom of the mantle, our results do not support the hypothesis that the negative buoyancy of melts is related to an extraordinary structural densification mechanism, as proposed by previous studies (Kono et al., 2017; Murakami and Bass, 2010; Prescher et al., 2017). Further, based on previous knowledge about the melting properties of the lower mantle minerals, it has been shown that much higher temperatures at the CMB of above 4150 K and much hotter core are needed to melt lower mantle minerals (Andrault et al., 2014) and that lowering of the melting temperature could be reached by introduction of minor amounts of alkalis or volatiles. However, the introduction of these components would not directly increase the density. In addition, melting of the lower mantle alone would not increase the resulting melt density compared to the corresponding crystalline counterparts. One plausible explanation for the existence of high-density silicate melts at the bottom of the mantle is that this is caused by the enrichment of the melts with iron from the outer core that increases the density of the melts (Liu et al., 2016). At the interface between the core and the mantle, molten iron alloy can penetrate into the lower mantle. At the bottom of the mantle these molten dense alloys can interact with the minerals and cause partial melting, enrichment of iron in the melt and thus an increase in their density. Some recent studies proposed that subducted oceanic lithosphere can reach the lower most mantle and undergo partial melting (Andrault et al., 2014; Pradhan et al., 2015). A new study investigated the hydration of different high-pressure SiO_2 phases that are typical for oceanic lithosphere at high pressures and temperatures and reported that oceanic crust can transport about 0.2 wt% water to the CMB, where upon heating it undergoes partial melting and reacts with the core generating iron hydrides, that might explain the phenomenon behind the ultra-low velocity zones in this region (Lin et al., 2021). Considering the literature and the results of this study, we conclude that proposed ultra-dense melts as a potential explanation for the ULVZs at the bottom of the mantle could be rather due to mixing of mantle material with molten iron alloy from the core that generates partial melting of the mantle and increase of the density by fractionation of Fe into the silicate melt, rather than due to extra-ordinary changes in the structure. At this stage of the knowledge, there is no clear evidence for the subducted oceanic lithosphere as the origin of the ULVZs as suggested by Lin et al. (2021), Nevertheless, both, iron from the core and alkali and volatiles from the subducted lithosphere could facilitate the melting of the material, and at the same time iron could increase the density and provide gravitationally stable melt at the bottom of the mantle.

Further potential implications resulting from the data of this study are related to the solubility of noble gases in melts as discussed in Chapter 4. At pressures below 15 GPa noble gases have high solubilities in silicate melts (Bouhifd and Jephcoat, 2006; Bouhifd et al., 2020), which was explained by the open sixfold tetrahedral ring structures of the melts up to these pressures. At higher pressures the solubility of noble gases strongly reduces, which has been

attributed to the collapse of the sixfold tetrahedral rings (Bouhifd et al., 2006). The highest solubilities are observed for polymerized Si-rich compositions, whereas basaltic melts show low solubilities. Based on the data of this thesis (Chapter 4), strong reduction in the solubility could be also related to the onset of the 4- to 6-fold structural transformations on one hand. On the other hand, the structure of melts at lower mantle conditions implies that only a low solubility can be expected if there is no other incorporation mechanism available. According to Bouhift et al., 2013, high partition coefficients between metallic and silicate melts at high pressure confirm this assumption, but certainly further data at pressures above 20 GPa are needed to better constrain the transport of noble gases in the lower mantle. Our data suggest that the overall structural behavior of silicate melts at the conditions of the lower mantle can considerably influence the abundance of the noble gases in the Earth's mantle (Chapter 4).

Outlook

Even though many aspects of silicate melts at conditions of the lower mantle have been thoroughly addressed in this study, there are still a couple of aspects that could improve our understanding, which are as

1) Further improvements in the fitting of the Sr local coordination environment and

2) Separate study on structural properties of Sr in simple glasses such as $SrSiO_3$ at conditions of the lower mantle

3) Investigation of the melting behavior of basaltic composition under compression to megabar conditions

Even though this is the only data set showing structural properties of Sr in silicate glasses at pressures of the lower mantle, the analysis could be considerably improved to better constrain the fitted maximum coordination number of 9. This would require an appropriate treatment of the multi-electronic excitation (MEE) visible in EXAFS signals of Sr K edge in studied glasses that could potentially lead to the underestimation of the fitted coordination number parameter values at higher pressures (see Chapter 3). Because the algorithm used to treat the EXAFS background could not remove the effects of the excitation edges from the atomic background, the development of a more suitable procedure could provide more reliable results. We assume that the suppression of the MEE effects on the EXAFS signal could provide higher and most likely more reliable values of the fitted Sr coordination number.

Due to missing data on the structural transformations of Sr in pure silicate glasses at high pressure conditions relevant for the lower mantle, we compared the structural properties of Sr in complex aluminosilicate glasses with Sr in crystalline Sr silicate and Sr carbonate compounds, as well as with Mg in amorphous $MgSiO_3$. In order to constrain the compositional effects on the structural transformations of Sr in amorphous systems, additional high pressure study on local structural environment of Sr in simple silicate glasses ($SrSiO_3$) should be conducted, using the experimental approach, like the one applied in this study (Chapter 3). By using the same experimental protocol and the same data treatment, potential differences in the evolution of the Sr-O distances and in the fitted coordination number could be directly and unambiguously related to the compositional effects and different roles of Sr in the specific system (network modifing role in $SrSiO_3$ vs. dual role as a network modifier and charge compensator for Al in aluminosilicate glasses).

One of the objectives of this study was to find out what is at the origin of the ULVZs at the bottom of the mantle. In this sense the major question was whether ultra-dense silicate melts, that are proposed to be in the origin of these low velocity zones, are due to structural changes in melt that occur at the conditions of the lower most mantle, or whether they are due to distinct melt composition with respect to the lower mantle environment. The results of this study suggest that gravitationally stable silicate melts at the bottom of the mantle cannot be due to extra-ordinary changes in the structure, and that therefore the answer has to be in their chemical composition. The results of this thesis suggest that subducted oceanic lithosphere could reach high density that would allow it to travel to the lower most mantle. In order to test this conception and to provide a clear picture about necessary chemical components that would allow partial melting at CMB conditions on one hand and at the same time to be denser than the surrounding material, detailed studies on the melting behavior of basaltic composition under compression to megabar conditions are needed. In this context it should be noted that in order to reach required non-buoyant densities, the enrichment of iron in the basaltic composition is likely required. Melting properties should be tested for multiple compositional variations of the basic iron doped basaltic assemblage. For this, the variations in iron concentration should be considered, but possibly also the usage of the FeO vs. Fe_2O_3. In this context, ferrous iron could partially substitute either Mg^{2+} or Ca^{2+}, whereas ferric iron could partially substitute Al^{3+}. Molten iron alloys that mix with the subducted basaltic lithosphere could potentially lower the melting temperature. Nevertheless, the potential role of volatile and alkali components should be further studied as these are considered to lower the melting temperature. For this purpose, apart from alkalies, the effect of small amounts of water and/or CO_2 or other volatiles should be constrained. The results should demonstrate whether one of several compositional variations could sufficiently lower the melting temperature of an iron-enriched basaltic composition. Detailed study on melting properties of basalt at the pressure conditions of the lower most mantle could show whether the hypothesis about the subducted oceanic lithosphere as the origin of ULVZs at the CMB is justified or not.

Chapter 7

References

Albornoz, J. C., Landínez Téllez, D. A., Roa-Rojas, J., Munévar, J. A., Baggio-Saitovich, E. (2013). Structural and magnetic properties of the new La2SrCo 2FeO9 triple perovskite. Journal of Superconductivity and Novel Magnetism, 26(6), 2313–2317. https://doi.org/10.1007/s10948-012-1425-4

Andrault, D., Pesce, G., Bouhifd, M. A., Bolfan-Casanova, N., Heńot, J. M., Mezouar, M. (2014). Melting of subducted basalt at the core-mantle boundary. Science, 344(6186), 892–895. https://doi.org/10.1126/science.1250466

Bajgain, S., Ghosh, D. B., Karki, B. B. (2015). Structure and density of basaltic melts at mantle conditions from first-principles simulations. Nature Communications, 6. https://doi.org/10.1038/ncomms9578

Baldini, M., Aquilanti, G., Mao, H. K., Yang, W., Shen, G., Pascarelli, S., Mao, W. L. (2010). High-pressure EXAFS study of vitreous GeO_2 up to 44 GPa. Physical Review B - Condensed Matter and Materials Physics, 81(2). https://doi.org/10.1103/PhysRevB.81.024201

Benmore, C. J., Soignard, E., Amin, S. A., Guthrie, M., Shastri, S. D., Lee, P. L., Yarger, J. L. (2010). Structural and topological changes in silica glass at pressure. Physical Review B - Condensed Matter and Materials Physics, 81(5). https://doi.org/10.1103/PhysRevB.81.054105

Bercovici, D., Karato, S. I. (2003). Whole-mantle convection and the transition-zone water filter. Nature, 425(6953), 39–44. https://doi.org/10.1038/nature01918

Biedermann, N., Bykova, E., Morgenroth, W., Efthimiopoulos, I., Mueller, J., Spiekermann, G., Glazyrin, K., Pakhomova, A., Appel, K., Wilke, M., 32, 2020. Equation of state and high-pressure phase behavior of $SrCO_3$. European Journal of Mineralogy, 32(6), 575–586. https://doi.org/10.5194/ejm-32-575-2020

Bouhifd, M. A., Jephcoat, A. P. (2006). Aluminium control of argon solubility in silicate melts under pressure. Nature, 439(7079), 961–964.

https://doi.org/10.1038/nature04583

Bouhifd, M. A., Jephcoat, A. P., Heber, V. S., Kelley, S. P. (2013). Helium in earth's early core. Nature Geoscience, 6(11), 982–986.
https://doi.org/10.1038/ngeo1959

Bouhifd, A. M., Jephcoat, A. P., Porcelli, D., Kelley, S. P., Marty, B. (2020). Potential of Earth's core as a reservoir for noble gases: Case for helium and neon. Geochemical Perspectives Letters, 15–18.
https://doi.org/10.7185/geochemlet.2028

Brown, I. D., 2009.Recent developments in the methods and applications of the bond valence model, Chem. Rev. 109, 6858.

Cormier, L., Calas, G., Creux, S., Gaskell, P.H., Bouchet-Fabre, B., Hannon, A.C., 1999. Environment around strontium in silicate and aluminosilicate glasses. Phys. Rev. B 59, 13517–13520.
https://doi.org/10.1103/PhysRevB.59.13517.

D'Angelo, P., Nolting, H.F., Pavel, N.V., 1996. Evidence for multielectron resonances at the Sr K edge. Phys. Rev. A - Atomic, Mol. Optical Phys. 53 (2), 798–805.
https://doi.org/10.1103/PhysRevA.53.798.

Elliott, S. R. (2001). Amorphous Materials: Medium-range Order. In Encyclopedia of Materials: Science and Technology (pp. 215–219). Elsevier. https://doi.org/10.1016/b0-08-043152-6/00046-2

Fei, H. (2021, January 16). Water Content of the Dehydration Melting Layer in the Topmost Lower Mantle. Geophysical Research Letters. Blackwell Publishing Ltd.
https://doi.org/10.1029/2020GL090973

Fiquet, G. (2018). Melting in the earth's deep interior. In Magmas Under Pressure: Advances in High-Pressure Experiments on Structure and Properties of Melts (pp. 115–134). Elsevier. https://doi.org/10.1016/B978-0-12-811301-1.00004-6

Garnero, E. J., Grand, S. P., Helmberger, D. V. (1993). Low Pwave velocity at the base of the mantle. Geophysical Research Letters, 20(17), 1843–1846.
https://doi.org/10.1029/93GL02009

Garnero, E. J., Helmberger, D. V. (1998). Further structural constraints and uncertainties of a thin laterally varying ultralow-velocity layer at the base of the mantle. Journal of Geophysical Research: Solid Earth, 103(6), 12495–12509. https://doi.org/10.1029/98jb00700

Garnero, E. J., McNamara, A. K. (2008, May 2). Structure and dynamics of earth's

lower mantle. Science. https://doi.org/10.1126/science.1148028

Ghosh, D. B., Karki, B. B. (2018). First-principles molecular dynamics simulations of anorthite ($CaAl_2Si_2O_8$) glass at high pressure. Physics and Chemistry of Minerals, 45(6), 575–587. https://doi.org/10.1007/s00269-018-0943-4

Giordano D., Russel J.K., Dingwell D. (2008) Viscosity of magmatic liquids: A model. Earth and Planetary Science Letters 271, 123–134

Greaves, G. N. (1985). EXAFS and the structure of glass. Journal of Non-Crystalline Solids, 71(1–3), 203–217. https://doi.org/10.1016/0022-3093(85)90289-3

Guthrie, M., Tulk, C. A., Benmore, C. J., Xu, J., Yarger, J. L., Klug, D. D., Tse, J. S., Mao, H-k. R. J. Hemley (2004). Formation and structure of a dense octahedral glass. Physical Review Letters, 93(11). https://doi.org/10.1103/PhysRevLett.93.115502

Henderson, G. S. (1995). A Si K-edge EXAFS/XANES study of sodium silicate glasses. Journal of Non-Crystalline Solids, 183(1–2), 43–50. https://doi.org/10.1016/0022-3093(94)00651-2

Henderson, G.S., 2005. The Structure of Silicate Melts: A Glass Perspective. Can Mineral 43, 1921–1958. doi:10.2113/gscanmin.43.6.1921

Henderson, P., Nolan, J., Cunningham, G.C., Lowry, R.K., 1985. Structural controls and mechanisms of diffusion in natural silicate melts. Contrib. Mineral. Petrol. 89, 263–272. https://doi.org/10.1007/BF00379459.

Hong, X., Newville, M., Duffy, T. S., Sutton, S. R., Rivers, M. L. (2014). X-ray absorption spectroscopy of GeO_2 glass to 64 GPa. Journal of Physics Condensed Matter, 26(3). https://doi.org/10.1088/0953-8984/26/3/035104

Huang, C., Cormack, A. N. (1990). The structure of sodium silicate glass. The Journal of Chemical Physics, 93(11), 8180–8186. https://doi.org/10.1063/1.459296

Itié, J. P., Polian, A., Calas, G., Petiau, J., Fontaine, A., Tolentino, H. (1989). Pressure-induced coordination changes in crystalline and vitreous GeO_2. Physical Review Letters, 63(4), 398–401. https://doi.org/10.1103/PhysRevLett.63.398

Kim, Y.H., Yi, Y.S., Kim, H.I., Chow, P., Xiao, Y., Shen, G., Lee, S.K., 2019. Structural transitions in $MgSiO_3$ glasses and melts at the core-mantle boundary observed via inelastic X-ray scattering. Geophys. Res. Lett. 46 (23), 13756–13764. https://doi.org/10.1029/2019GL085889.

Kirkpatrick, R. J. (1975). Crystal growth from the melt: A review. Am. Mineral.,

60, 798–814.

Kirkpatrick, R. J. (1983). Theory of nucleation in silicate melts. American Mineralogist, 68(1–2), 66–77.

Kono, Y., Kenney-Benson, C., Ikuta, D., Shibazaki, Y., Wang, Y., Shen, G., Navrotsky, A. (2016). Ultrahigh-pressure polyamorphism in GeO_2 glass with coordination number >6. Proceedings of the National Academy of Sciences of the United States of America, 113(13), 3436–3441. https://doi.org/10.1073/pnas.1524304113

Lay, T., Williams, Q., Garnero, E. J. (1998, April 2). The core-mantle boundary layer and deep Earth dynamics. Nature. https://doi.org/10.1038/33083

Lelong, G., Cormier, L., Ferlat, G., Giordano, V., Henderson, G. S., Shukla, A., Calas, G. (2012). Evidence of fivefold-coordinated Ge atoms in amorphous GeO_2 under pressure using inelastic x-ray scattering. Physical Review B - Condensed Matter and Materials Physics, 85(13). https://doi.org/10.1103/PhysRevB.85.134202

Li, M., McNamara, A. K., Garnero, E. J., Yu, S. (2017). Compositionally-distinct ultra-low velocity zones on Earth's core-mantle boundary. Nature Communications, 8(1). https://doi.org/10.1038/s41467-017-00219-x

Lin, Y., Hu, Q., Yang, J., Meng, Y., Zhuang, Y., Walter, M J., Mao, H-K. (in print). Hydrous SiO_2 in subducted oceanic crust and water transport to the core-mantle boundary

Liu, J., Li, J., Hrubiak, R., Smith, J. S. (2016). Origins of ultralow velocity zones through slab-derived metallic melt. Proceedings of the National Academy of Sciences of the United States of America, 113(20), 5547–5551.
https://doi.org/10.1073/pnas.1519540113

Meade, C., Hemley, R. J., Mao, H. K. (1992). High-pressure x-ray diffraction of SiO_2 glass. Physical Review Letters, 69(9), 1387–1390. https://doi.org/10.1103/PhysRevLett.69.1387

Marrocchelli, D., Salanne, M., Madden, P. A. (2010). High-pressure behaviour of GeO_2: A simulation study. Journal of Physics Condensed Matter, 22(15).
https://doi.org/10.1088/0953-8984/22/15/152102

Micoulaut, M. (2004, March 17). Structure of densified amorphous germanium dioxide. Journal of Physics Condensed Matter. https://doi.org/10.1088/0953-8984/16/10/L03

Murakami, M., Bass, J. D. (2010). Spectroscopic evidence for ultrahigh-pressure polymorphism in SiO_2 glass. Physical Review Letters, 104(2).

https://doi.org/10.1103/PhysRevLett.104.025504

Mysen, B. O., Richet, P. (2005). Silicate Glasses and Melts: Properties and Structure. Elsevier Science.

Mysen, B. O., Toplis, M. J. (2007). Structural behavior of Al^{3+} in peralkaline, metaluminous, and peraluminous silicate melts and glasses at ambient pressure. American Mineralogist, 92(5–6), 933–946. https://doi.org/10.2138/am.2007.2334

Mysen, B. O., Virgo, D., Kushiro, I. (1981). The structural role of aluminum in silicate melts-a Raman spectroscopic study at 1 atmosphere. American Mineralogist, 66(7–8), 678–701.

Mysen, B. O., Virgo, D., Seifert, F. A. (1985). Relationships between properties and structure of aluminosilicate melts. American Mineralogist, 70(1–2), 88–105.

Neuville, D. R., Cormier, L., Massiot, D. (2004). Al environment in tectosilicate and peraluminous glasses: A 27Al MQ-MAS NMR, Raman, and XANES investigation. Geochimica et Cosmochimica Acta, 68(24), 5071–5079. https://doi.org/10.1016/j.gca.2004.05.048

Niu, Y. (1997). Mantle melting and melt extraction processes beneath ocean ridges: Evidence from abyssal peridotites. Journal of Petrology, 38(8), 1047–1074. https://doi.org/10.1093/petroj/38.8.1047

M. O'Keeffe and B. G. Hyde, The role of nonbonded forces in crystals, in Structure and Bonding in Crystals, edited by M. O'Keeffe and A. Navrotsky (Academic Press Inc., New York, 1981), Chap. 10, Vol. 1, p. 227.

Panero, W. R., Thomas, C., Myhill, R., Pigott, J. S. (2020). Dehydration Melting Below the Undersaturated Transition Zone. Geochemistry, Geophysics, Geosystems, 21(2). https://doi.org/10.1029/2019GC008712

Pauling, L., The principles determining the structure of complex ionic crystals, J. Am. Chem. Soc. 51, 1010 (1929).

Petitgirard, S., Malfait, W. J., Journaux, B., Collings, I. E., Jennings, E. S., Blanchard, I., Kantor, I., Kurnosov, A., Cotte, M., Dane, T., Burghammer, M., Rubie, D. C. (2017). SiO_2 Glass Density to Lower-Mantle Pressures. Physical Review Letters, 119(21). https://doi.org/10.1103/PhysRevLett.119.215701

Petitgirard, S., Sahle, C.J., Weis, C., Gilmore, K., Spiekermann, G., Tse, J.S., Wilke, M., Cavallari, C., Cerantolla, V., Sternemann, C., 2019. Magma properties at deep Earth's conditions from electronic structure of silica. Geochem. Perspect. Lett. 9, 32–37.

https://doi.org/10.7185/geochemlet.1902

Pohlenz, J., Rosa, A. D., Mathon, O., Pascarelli, S., Belin, S., Landrot, G., Murzin, V., Veligzhanin, A., Shiryaev, A., Irifune, T., Wilke, M. (2018). Structural controls of CO_2 on Y, La and Sr incorporation in sodium-rich silicate - carbonate melts by *in-situ* high P-T EXAFS. Chemical Geology, 486, 1–15. https://doi.org/10.1016/j.chemgeo.2017.12.023

Pradhan, G. K., Fiquet, G., Siebert, J., Auzende, A. L., Morard, G., Antonangeli, D., Garbarino, G. (2015). Melting of MORB at core-mantle boundary. Earth and Planetary Science Letters, 431, 247–255. https://doi.org/10.1016/j.epsl.2015.09.034

Prescher, C., Prakapenka, V. B., Stefanski, J., Jahn, S., Skinner, L. B., Wang, Y. (2017). Beyond sixfold coordinated Si in SiO_2 glass at ultrahigh pressures. Proceedings of the National Academy of Sciences of the United States of America, 114(38), 10041–10046. https://doi.org/10.1073/pnas.1708882114

Prowatke, S., Klemme, S. (2005). Effect of melt composition on the partitioning of trace elements between titanite and silicate melt. Geochimica et Cosmochimica Acta, 69(3), 695–709. https://doi.org/10.1016/j.gca.2004.06.037

Putnis, A. (1992). Introduction to mineral sciences. Introduction to Mineral Sciences. https://doi.org/10.1016/0016-7037(93)90207-d

Revenaugh, J., Meyer, R. (1997). Seismic evidence of partial melt within a possibly ubiquitous low- velocity layer at the base of the mantle. Science, 277(5326), 670–673. https://doi.org/10.1126/science.277.5326.670

Revenaugh, J., Sipkin, S. A. (1994). Seismic evidence for silicate melt atop the 410-km mantle discontinuity. Nature, 369(6480), 474–476. https://doi.org/10.1038/369474a0

Sanloup, C., Drewitt, J. W. E., Konôpková, Z., Dalladay-Simpson, P., Morton, D. M., Rai, N., van Westrenen, N., Morgenroth, W. (2013). Structural change in molten basalt at deep mantle conditions. Nature, 503(7474), 104–107. https://doi.org/10.1038/nature12668

Sato, T., Funamori, N. (2010). High-pressure structural transformation of SiO_2 glass up to 100 GPa. Physical Review B - Condensed Matter and Materials Physics, 82(18). https://doi.org/10.1103/PhysRevB.82.184102

Scarfe, C. M., Mysen, B. O., Virgo, D. (1987). Pressure dependence of the viscosity of silicate melts. Magmatic Processes: Physicochemical Principles, 59–67.

Schmandt, B., Jacobsen, S. D., Becker, T. W., Liu, Z., Dueker, K. G. (2014). Dehydration melting at the top of the lower mantle. Science, 344(6189), 1265–1268.

https://doi.org/10.1126/science.1253358

Smith, W., Greaves, G. N., Gillan, M. J. (1995). The structure and dynamics of sodium disilicate glass by molecular dynamics simulation. Journal of Non-Crystalline Solids, 192–193, 267–271. https://doi.org/10.1016/0022-3093(95)00441-6

Spera, F.J., Nevins, D., Ghiorso, M., Cutler, I., 2009. Structure, thermodynamic and transport properties of $CaAl_2Si_2O_8$ liquid. Part I: Molecular dynamics simulations. Geochim. Cosmochim. Acta 73 (22), 6918–6936.
https://doi.org/10.1016/j.gca.2009.08.011.

Spiekermann, G., Harder, M., Gilmore, K., Zalden, P., Sahle, C.J., Petitgirard, S., Wilke, M., Biedermann, N., Weis, C., Morgenroth, W., Tse, J.S., Kulik, E., Nishiyama, N., Yavas, H., Sternemann, C., (2019). Persistent Octahedral Coordination in Amorphous GeO_2 up to 100 GPa by Kβ" X-Ray Emission Spectroscopy. Phys. Rev. X 9 (1).
https://doi.org/10.1103/PhysRevX.9.011025.

Stebbins, J.F., 1995. Dynamics and structure of silicate and oxide melts: Nuclear magnetic resonance studies. In: Stebbins, J.F., McMillan, P.F., Dingwell, D.B. (Eds.), Structure, Dynamics and Properties of Silicate Melts, Vol. 32. Mineralogical Society of America, Washington, D.C., p. 191. Chap. 7.

Stebbinss, J. F. (2016, April 1). Glass structure, melt structure, and dynamics: Some concepts for petrology. American Mineralogist. Walter de Gruyter GmbH.
https://doi.org/10.2138/am-2016-5386

Trail, D., Tailby, N., Wang, Y., Mark Harrison, T., Boehnke, P. (2017). Aluminum in zircon as evidence for peraluminous and metaluminous melts from the Hadean to present. Geochemistry, Geophysics, Geosystems, 18(4), 1580–1593. https://doi.org/10.1002/2016GC006794

Vaccari, M., Aquilanti, G., Pascarelli, S., Mathon, O. (2009). A new EXAFS investigation of local structural changes in amorphous and crystalline GeO_2 at high pressure. Journal of Physics Condensed Matter, 21(14). https://doi.org/10.1088/0953-8984/21/14/145403

Vessal, B., Greaves, G. N., Marten, P. T., Chadwick, A. V., Mole, R., Houde-Walter, S. (1992). Cation microsegregation and ionic mobility in mixed alkali glasses. Nature, 356(6369), 504–506. https://doi.org/10.1038/356504a0

Vinnik, L., Farra, V. (2007). Low S velocity atop the 410-km discontinuity and mantle plumes. Earth and Planetary Science Letters, 262(3–4), 398–412.
https://doi.org/10.1016/j.epsl.2007.07.051

Wen, L., Helmberger, D. V. (1998). A two-dimensional P-SV hybrid method and its application to modeling localized structures near the core-mantle boundary. Journal of

Geophysical Research: Solid Earth, 103(8), 17901–17918. https://doi.org/10.1029/98jb01276

Williams, Q., Garnero, E. J. (1996). Seismic evidence for partial melt at the base of earth's mantle. Science, 273(5281), 1528–1530. https://doi.org/10.1126/science.273.5281.1528

Wolf, G.H., McMillan, P.F., (1995). Pressure effects on silicate melt structure and properties. In: Stebbins, J.F., McMillan, P.F., Dingwell, D.B. (Eds.), Structure, Dynamics and Properties of Silicate Melts, Vol. 32. Mineralogical Society of America, Washington, DC, p. 50. Chap. 11.

Xiao, W., Tan, D., Zhou, W., Liu, J., Xu, J., 2013. Cubic perovskite polymorph of strontium metasilicate at high pressures. Am. Mineral. 98 (11–12), 2096–2104.
https://doi.org/10.2138/am.2013.4470.

Yuan, K., Romanowicz, B. (2017). Seismic evidence for partial melting at the root of major hot spot plumes. Science, 357(6349). https://doi.org/10.1126/science.aan0760

Yusa, H., Akaogi, M., Sata, N., Kojitani, H., Kato, Y., Ohishi, Y., 2005. Unquenchable hexagonal perovskite in high-pressure polymorphs of strontium silicates. Am. Mineral. 90 (5–6), 1017–1020.
https://doi.org/10.2138/am.2005.1835.

Zen, E. A. (1986). Aluminum enrichment in silicate melts by fractional crystallization: Some mineralogic and petrographic constraints. Journal of Petrology, 27(5), 1095–1117. https://doi.org/10.1093/petrology/27.5.1095

Zen, E. (1988). Phase relations of peraluminous granitic rocks and their petrogenetic implications. Annual Review of Earth and Planetary Sciences. Vol. 16, 21–51.
https://doi.org/10.1146/annurev.ea.16.050188.000321